The Dissertation Committee for Bum Jin Choi
certifies that this is the approved version of the following dissertation:

High $p_\perp$ Inclusive Charged Hadron Distributions in Au+Au Collisions at $\sqrt{s_{NN}} = 130$ GeV at RHIC

Committee:

_____
Fred Moore, Supervisor

_____
Peter Jacobs, Supervisor

_____
Gerry Hoffmann

_____
Lanny Ray

_____
Takeshi Udagawa

_____
William Guy

High $p_\perp$ Inclusive Charged Hadron Distributions in Au+Au Collisions at $\sqrt{s_{NN}} = 130$ GeV at RHIC

by

Bum Jin Choi, B.A.

DISSERTATION

Presented to the Faculty of the Graduate School of

The University of Texas at Austin

in Partial Fulfillment

of the Requirements

for the Degree of

DOCTOR OF PHILOSOPHY

THE UNIVERSITY OF TEXAS AT AUSTIN

August 2003

Dedicated to my mom, pop, and bro. Fortunately, for their sakes, they'll never read it.

Acknowledgments

To all my friends, enemies, people completely indifferent to my existence, others who lean slightly positively towards me, and still other who acknowlege me with a turned up nose or perhaps a bemused smile or none of the above.

In short, thanks to my advisors Fred Moore and Peter Jacobs, without whom I'd be presently working at McDonalds. Thanks to the bright folks at UT (in random order): Gerry Hoffmann, Lanny Ray, Curtis. Thanks to the bright folks at LBL (in alphabetical order): Dave, Fabrice, Geno, Ian, Jen, Kai, Kiril, and Musashi. Thanks to *et al*, namely (in random order): Chris, Manuel, Jamie, Matt, and Frank.

No thanks to the Eagles, Sixers, Phillies and the Flyers.

Oh yeah, thanks to Roger, Greg, Arlene, Vina, Paul, etc. for providing occasionally meaningful human interaction.

High $p_\perp$ Inclusive Charged Hadron Distributions in Au+Au Collisions at $\sqrt{s_{NN}} = 130$ GeV at RHIC

Publication No. _____

Bum Jin Choi, Ph.D.

The University of Texas at Austin, 2003

Supervisors: Fred Moore
Peter Jacobs

This thesis reports the measurement of the inclusive charged particle ($h^+ +$ h^-) p$_\perp$ spectra for $1.7 < p_\perp < 6$ GeV/c at midrapidity ($|\eta| < 0.5$) as a function of various centrality classes in Au+Au collisions at $\sqrt{s_{NN}}$=130 GeV. Hadron suppression is observed relative to both scaled NN and peripheral Au+Au reference data, possibly indicating non-Abelian radiative energy loss in a hot, dense medium.

Table of Contents

List of Tables

x

List of Figures

Chapter 1

Motiviation

1.1 Introduction

1.1.1 QCD

According to the Standard Model strong interactions [1] are described by Quantum Chromodynamics (QCD), a non-Abelian SU(3) gauge theory based on fermionic quarks mediated by the exchange of massless bosonic gluons [76, 93]. In analogy to QED's electric charge, quarks and gluons (collectively called partons) carry one of three color charges. However unlike QED, where photons do not self couple, the color charged gluons directly interact with one another resulting in two novel features.
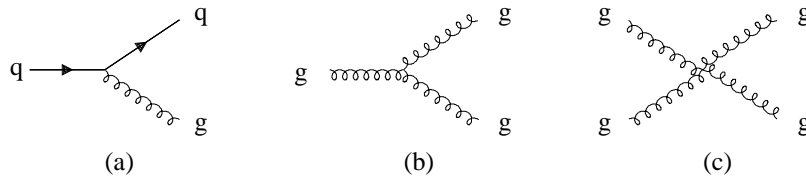
Figure 1.1: Elementary QCD vertices.

First, although QCD describes strong interactions, at large momentum transfer (short distance or short time) quarks are weakly interacting (*asymptotic freedom*) [16]. The coupling strength, g, decreases logrithmically as a function of Q^2 (Figure 1.2). For example, to first order in perturbative expansion, where $\Lambda_{\rm QCD}$ is a

---

[1]e.g. the binding force between nucleons in a nucleus

1
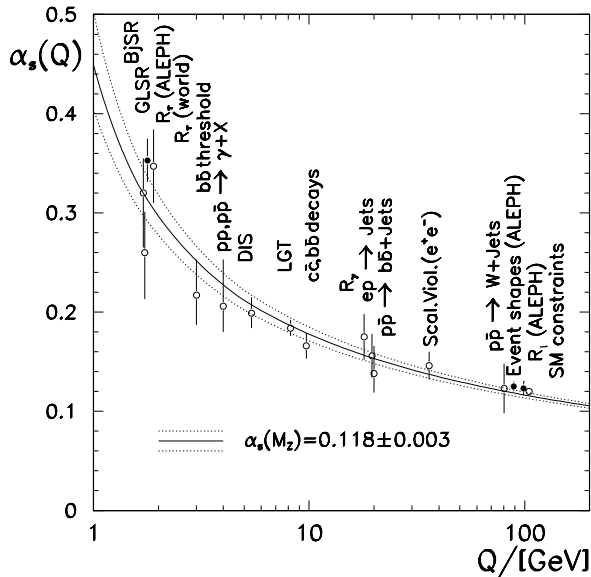
Figure 1.2: Measurements of $\alpha_s(Q)$ at various energy scales. The curves are the pQCD calculations based on the reference point $\alpha_s(M_Z) = 0.118 \pm .003$, the 1996 world average according to the Particle Data Group[50]. Note that α_s is a free parameter in QCD; but the Q (or Q^2) dependence can be computed given a reference value. (Figure taken from [36])

renormalization scale and β_1 a constant,

$$\alpha_s(Q^2) = \frac{g^2}{4\pi} \approx \frac{4\pi}{\beta_1 \ln Q^2/\Lambda_{\mathrm{QCD}}^2} \to 0, \ Q^2 \to \infty \,. \qquad (1.1)$$

Asymptotic freedom implies that for interactions at sufficiently high Q^2 (*hard processes*), the coupling strength is weak enough for perturbative QCD (pQCD) to be computationally valid. Typically, the lower limit of momentum transfer amenable to pQCD is $Q^2 \approx 2(\mathrm{GeV/c})^2$, which corresponds to $\alpha_s \approx 0.3$; although this value is debatable.

Second, quarks and gluons are believed to be *confined* in color singlet states, called hadrons [2]. Hadrons may consist of three bound valence quarks (baryons) or an antiquark-quark pair (mesons). Thus far, no free quarks have been observed. Although a full understanding of confinement currently does not exist, it is believed to be driven by strongly coupled, small momentum transfer interactions in the QCD vacuum ("sea quarks and gluons") and thus outside the purview of pQCD. To study

---

[2]Under 'ordinary' conditions or a vacuum. See below.
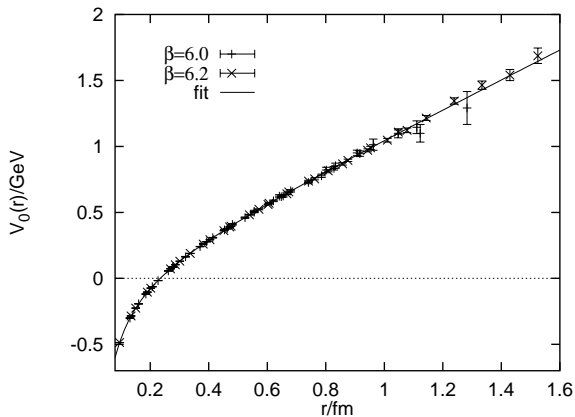
Figure 1.3: Lattice calculation of a static potential for $q - \bar{q}$. The fit function is $V = aR - \epsilon/R + f/R^2$. (Figure taken from [51])

the nonperturbative region, QCD has been formulated on a discrete space-time lattice and analyzed numerically [62, 63, 65]. For example, lattice computations indicate that at zero temperature the potential between a 'heavy' quark(q) and anti-quark($\bar{q}$) grows linearly with distance, r, for 'large' r (Figure 1.3):

$$V(r) \approx ar, \ r \sim 1\,\mathrm{fm} \tag{1.2}$$

where $a \approx 425\,\mathrm{MeV}$ is the string tension. For a simple intuitive picture of confinement, a quark and anti-quark can be viewed as being connected by a 'string' whose potential increases linearly as they are pulled apart. At some point, the string 'breaks' but instead of isolating the quark and anti-quark, there are now two strings (mesons) each with a q-$\bar{q}$ pair; confinement persists. This analogy illustrates the idea that at some point during the q-$\bar{q}$ separation, it becomes energetically favorable to spontaneously produce a q-$\bar{q}$ pair out of the vacuum, forming hadrons with the original quarks.

1.1.2 Deconfinement

Under extreme temperature, T, and/or baryon density [3], μ_B, partonic interactions may become weak and short ranged, resulting in a phase transition from confined hadrons to a QCD plasma of deconfined quarks and gluons [13, 61, 94] [4]. For instance, the early universe may have been a QCD plasma at high temperature and low baryon density until $\sim 10\mu$s after the Big Bang [7]. Presently, the core of a neutron star may be a color superconducting QCD plasma at high baryon density and low temperature [49, 74].

The basic physical reasons for a deconfined color-charged QCD plasma are twofold [52]. First, the QCD coupling strength becomes weak at high temperature and/or baryon density; i.e. a temperature dependent asymptotic freedom [17]:

$$\alpha_s \propto \frac{1}{\ln T \,\text{or}\, \mu_B} \to 0. \tag{1.3}$$

For $T > 300$ MeV, the coupling "constant" may be $\alpha_s < 0.3$ [60]. Second, the Coloumb potential as seen by a test quark is screened by interactions of the surrounding partons (i.e. color screened *Yukawa* potential).

$$V(r) \approx \frac{g^2}{4\pi} \frac{\exp^{-\mu_D r}}{r}, \tag{1.4}$$

where μ_D is the Debye mass. This phenomenon is called Debye screening, in analogy to dielectric screening in a QED plasma. Short of extreme temperatures on the order of $T \sim 10$ GeV, non perturbative Debye screening, over asymptotic freedom, may be the dominant process for deconfinement [62].

Thermodynamic properties of QCD plasma have been studied using the lattice formulation [62]. Figure 1.4 shows a lattice calculation of the energy density, ϵ, divided by T^4 as a function of temperature at $\mu_B = 0$. The abrupt jump in energy

---

[3]Note that low baryon density implies low baryon chemical potential.
[4]Current jargon is the Quark Gluon Plasma (QGP).
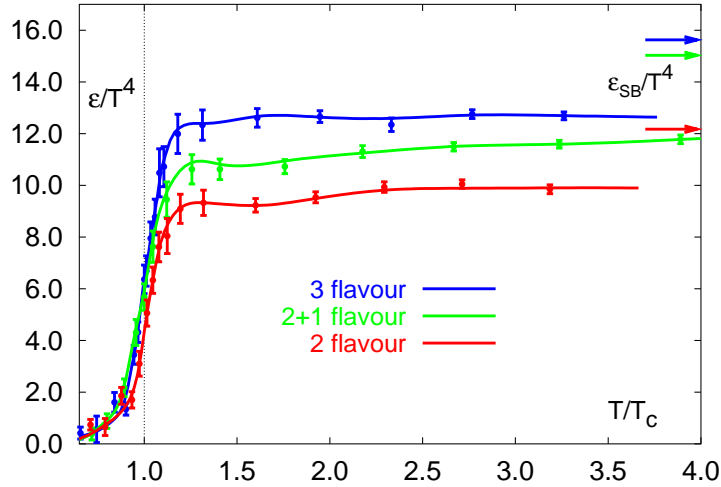
Figure 1.4: Lattice calculation of energy density as a function of temperature for 2 light, 2+1 (2 light and 1 heavy), and 3 light dynamic quarks. The critical temperatures (T_c) are 171 ± 4, 173 ± 8, and 154 ± 8 MeV, respectively. The corresponding critical energy density is $\epsilon_c \approx (6 \pm 2)T_c^4$ [62].

density ($\Delta\epsilon/T_c^4 \approx 8$) at the critical temperature, T_c, reflects the liberation of many degrees of freedom in the transition from hadronic matter to the deconfined phase. As the temperature approaches infinity, the QCD matter behaves as a free partonic gas and the energy density should approach the Stefan-Boltzmann ideal gas limit of

$$K_{SB} = \frac{\epsilon}{T^4} \approx (2_s \times 8_c + \frac{7}{8} \times 2_s \times 2_{q+\bar{q}} \times (N_f = 2))\frac{\pi^2}{30} \approx 12 \qquad (1.5)$$

which takes into account spin, color, anti-quark, and 2 flavor degrees of freedom. However, even at $T = 4T_c$ the energy density falls short of the ideal gas limit by $\sim 20\%$, indicating that non-perturbative effects persist at this temperature. The phase transition may be second order for two flavors and first order for three flavors but further study is needed as the order is sensitive to the quark mass; in fact the transition may be a rapid crossover for a realistic quark mass spectrum. The critical temperature is $T_c \approx 170$ MeV, corresponding to a critical energy density of

Early Universe

LHC: Pb-Pb (2005)
$\sqrt{s}$ = 5.5 ATeV

Quark-Gluon Plasma

deconfinement

T

RHIC: Au-Au (now!)
$\sqrt{s}$ = 200 AGeV

SPS: Pb-Pb (now)
E_b = 158 AGeV
$\sqrt{s}$ = 17 AGeV

T_c

E_b = 40 AGeV

AGS: Au-Au, (past)
E_b = 11 AGeV
$\sqrt{s}$ = 5 AGeV

Hadron Gas

confinement

neutron stars?

μ_B
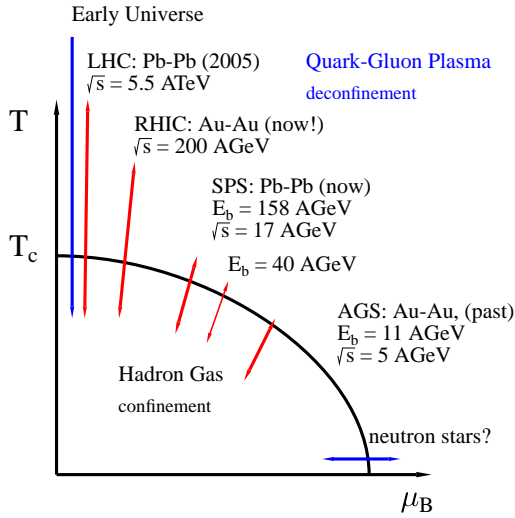
Figure 1.5: Standard QCD phase diagram and possible regions of exploration for various experimental programs, past, present, and future. The particular trajectories of exploration should be taken with a grain of salt. The SPS and AGS are fixed target accelerators while RHIC and LHC are colliders. E_b is the beam energy and $\sqrt{s}$ is the center of mass energy. (Figure taken from [21])

$\epsilon_c \approx 1\,\mathrm{GeV/fm^3}$. For comparison, the energy density for 'cold' nuclear matter is $\epsilon \approx 0.16\,\mathrm{GeV/fm^3}$.

1.2 Relativistic Heavy Ion Collisions

The extreme conditions necessary for a QCD plasma phase may be achieved in the laboratory through the collision of heavy ions ($A \sim 200$) at high center of mass energy. The possible formation and properties of a QCD plasma has been been and will be explored with several relativistic heavy ion accelerators (Figure 1.5). For example, the fixed target experiments at the AGS at BNL and at the SPS at CERN have begun the search at $\sqrt{s_{\mathrm{NN}}}$=5 GeV and $\sqrt{s_{\mathrm{NN}}}$=17 GeV, respectively. They have yielded intriguing results, though arguably not conclusive of a plasma phase. In the year 2000, experiments at the Relativistic Heavy Ion Collider (RHIC) have begun to investigate the region closer to the theoretically best understood limit of $\mu_B/T \to 0$, by colliding Au ions ($A = 197$) at a center of mass energy per nucleon pair ($\sqrt{s_{\mathrm{NN}}}$) of 130 GeV. With $\sqrt{s_{\mathrm{NN}}}$ an order of magnitude greater than at the SPS, new physics channels are accessible to experimental analysis at RHIC, in particular
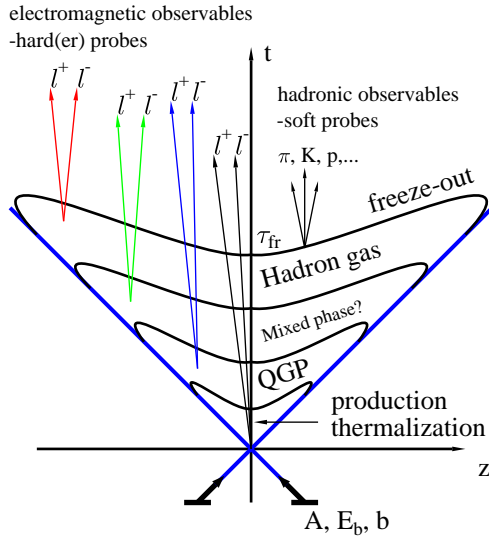
Figure 1.6: Possible spacetime evolution of an A+A collision.

hard processes and jets.

Ideally, the produced strongly interacting system would have a volume as large and a lifetime long enough that thermodynamic principles can be applied when interpretating the data. This implies the goal of generating as many final state particles as possible. Thus while conventional high energy particle physics, colliding elementary ($e^+ + e^-$) or simple composite particles (p+p), generate *tens* of particles, high energy heavy ions collisions produce a complex environment of *hundreds* (SPS) or *thousands* (RHIC) of secondary particles [21]. However, due to the highly dynamic nature of the system produced in heavy ion collisions, it is debatable whether an 'ideal' QCD plasma in global or local (thermal/chemical) equilibrium is formed. Rather, it may be more sensible to consider the formation of a 'general' dense QCD matter in an extended volume ($\gg 1$ fm) with a long lifetime ($\gg 1$ fm/c).

Figure 1.6 shows a standard spacetime evolution diagram of an A+A collision. The two nuclei, Lorentz contracted as thin disks and surrounded by a dense virtual cloud of partons, collide and generate a hot, dense matter which immedi-
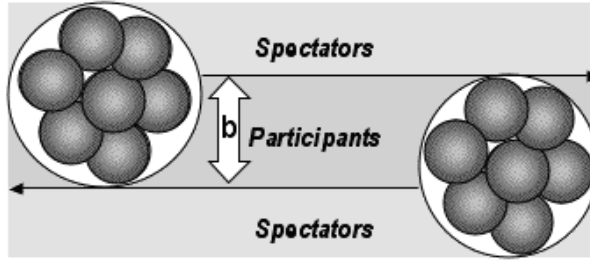
Figure 1.7: Two nuclei collide at impact parameter, *b*. Non interacting nucleons are *spectators*, while interacting nucleons are *participants*.

ately cools while expanding near the speed of light. If the system is sufficiently dense in energy, the QCD plasma may form during some time $\tau_0 \sim 0.2 - 1\,\mathrm{fm/c}$, thereupon evolving hydrodynamically. As the temperature drops, the partonic matter *hadronizes* into a hot gas. After further cooling and expansion of the hadron gas, inelastic interactions become infrequent which fixes the final species distribution (*chemical freezeout*), followed by the virtual cessation of elastic interactions which fixes the final momentum distribution (*kinetic freezeout*).

1.2.1 Geometry of Nuclear Collisions

For a systematic survey of initial conditions in A+A collisions, the controllable experimental parameters are the ion mass/size, energy, and the nuclear collision geometry. Theoretically, the geometry of a nuclear collision is characterized by the *impact parameter*, *b* (Figure 1.7). Collisions at smaller *b* produce a greater number of final state particles, and are expected to correspond to a greater initial energy density. However, the impact parameter is not directly accessible experimentally. Instead the collision geometry may be characterized by dividing the total inelastic cross section into *centrality* classes, based on observables such as hadron multiplicity, transverse energy, or forward neutrons. The fractions of cross sections may then be mapped into impact parameter space using the standard description of nuclear
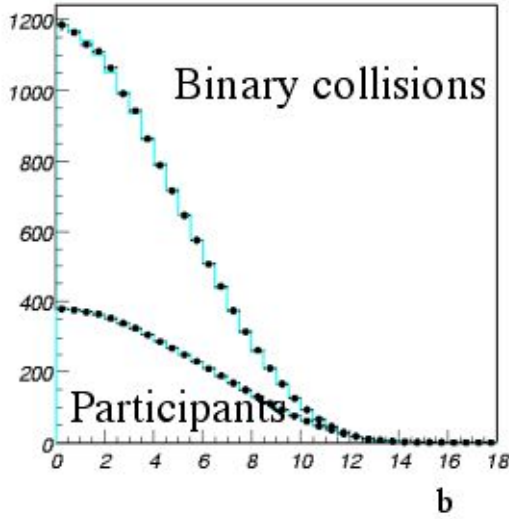
Figure 1.8: $\langle N_{part} \rangle$ and $\langle N_{bin} \rangle$ as a function of impact parameter b (fm) for Au+Au collisions at $\sqrt{s_{NN}}$=130 GeV. (Figure taken from [89])

collision geometry, the *Glauber* formalism [66, 92, 103]. Measurements as a function of centrality class may shed light on the onset of new physics.

Two additional concepts correlated with the impact parameter, based on the composite nature of a nucleus, are the mean number of *participants*, $\langle N_{part} \rangle$, and the mean number of *binary collisions*, $\langle N_{bin} \rangle$. A participant[5] is a nucleon that interacts inelastically. A binary collision simply refers to an inelastic collision between two nucleons. For example, a p+p collision involves two participants and a binary collision. An A+A collision is limited to $\langle N_{part} \rangle \leq 2A$. For a $\sqrt{s_{NN}}$=130 GeV Au+Au collision at $b = 0$, it is expected that $\langle N_{bin} \rangle \sim 1200$ (Figure 1.8).

According to the *two component* model [104], the rate of 'hard' and 'soft' processes[6] is expected to scale with $\langle N_{bin} \rangle$ and $\langle N_{part} \rangle$, respectively as

$$E \frac{dN_{AB}(b)}{d^3p} = \langle N_{part(b)} \rangle \frac{dN_{soft}(b)}{dyd^2p_\perp} + \langle N_{bin}(b) \rangle \frac{1}{\sigma_{inel}^{pp}} \frac{d\sigma_{hard}(b)}{dyd^2p_\perp} \qquad (1.6)$$

Observables deviating from the expected scaling may indicate physical processes unique to relativistic heavy ion collisions and a QCD plasma phase.

---

[5]Also known as a *wounded* nucleon.
[6]'Soft' processes are those not calculable by pQCD; i.e. $p_\perp \sim< 2$ GeV/c.

9

1.3 Jet Quenching

The QCD plasma cannot be studied directly; rather, it's formation and properties must be inferred from observables based on final state particles. Several QCD plasma signatures have been proposed, including J/Ψ suppression and strangeness enhancement [77]. Of particular interest are signatures from *hard probes*, i.e. interactions with a large momentum transfer that generate high $p_\perp$ particles [7]. Since the time scale of a hard process is smaller than the plasma's formation time $\Delta t \sim 1/m_T < \tau_0 \sim 0.5 \, \text{fm/c}$, high $p_\perp$ particles probe the QCD plasma in its earliest and hottest stage [8].

Theoretical studies have indicated that partons propagating through hot, dense matter lose energy (ΔE), primarily by radiating gluons from multiple inelastic scatterings [79, 81, 90] [9]. This is the non-Abelian QCD analogue of the familiar (photon) brehmstrallung in QED. For a thin, static medium of average thickness L, the radiative parton energy loss per length can be written as [105]

$$\frac{\text{d}E_{\text{rad}}}{\text{d}x} \approx C_R \frac{\alpha_s \mu_D^2}{4} \frac{L}{\lambda_g} \ln\left(\frac{2E}{\mu_D L}\right) \, , \qquad (1.7)$$

where C_R is the Casimir of the traversing parton (4/3 for quarks, 9/4 for gluons), λ_g the gluon mean free path, and μ_D the Debye screening mass. The L dependence arises from destructive interference effects from gluon rescattering ([90]). For an expanding medium, the total energy loss may be reduced by a factor $2\tau_0/L$, where τ_0 is the formation time of the medium. Since the above expression is proportional to L/λ_g (*opacity*), measurement of the energy loss may provide insight on the plasma's initial gluon density. Although energy loss does not directly indicate deconfinement,

---

[7] What is 'high' $p_\perp$? For the remainder of the thesis, high $p_\perp$ will be understood to be > 2 GeV/c, roughly corresponding to the lower limit of pQCD's applicablity. However, sometimes the term 'intermediate high' $p_\perp$ will be used for the region $2 < p_\perp < 6$ GeV/c.

[8] Perhaps ironically high $p_\perp$ particles are pQCD probes of a strictly non pQCD medium.

[9] *Elastic* scatterings also contribute to the energy loss, but it is expected to be relatively small [5].
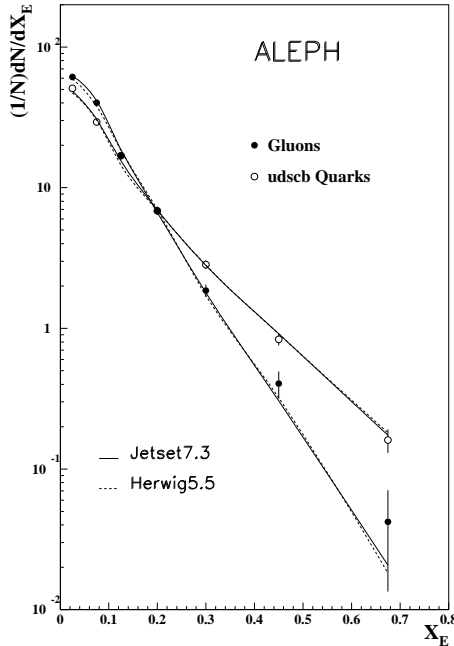
Figure 1.9: Quark and gluon fragmentation functions, at the same jet energy, 24 GeV, measured by the ALEPH Collaboration. Note that the gluon fragmentation is softer; i.e. gluon jets are more likely to contain lower energy particles than quark jets at the same total jet energy. Gluons jets also contain more particles than quark jets [35]. The abscissa is $x_E = E_{\mathrm{particle}}/E_{\mathrm{jet}}$. The solid and dashed lines are two model predictions. The median value of x_E is ~ 0.3. (Figure taken from [36])

an initial gluon density significantly larger than that of ordinary hadronic mattter may indirectly signal a deconfined QCD state.

Upon leaving the medium a parton hadronizes (fragments) into *jets*, clusters of hadrons in phase space. Experimentally, the definition of a jet is not unambiguous. For example, a quark jet make contain fragments from a soft radiated gluon. Several jet algorithms exist on the market, which may be grouped into two categories: (a) the JADE k_T 'clustering' algorithm and its variants, better at discriminating soft gluon jets, [37, 86]; and (b) the traditional 'cone' algorithm. In terms of the cone algorithm, a hadron with azimuthal angle ϕ_i and pseudorapidity η_i lies in a jet cone if

$$(\eta_i - \eta_C)^2 + (\phi_i - \phi_C)^2 < R \tag{1.8}$$

where (η_C, ϕ_C) describes the cone axis. The standard cone radius is $R = 0.7$ or 1. The momentum (energy) distribution of the particles in a jet is described by the *fragmentation* function, $D_{h/c}(z_c, Q^2)$. Formally, it is defined as the probability

11

density for parton c to fragment into hadron h with momentum fraction $z_c \equiv p_L/p_{\text{jet}}$ at scale Q^2, where p_L and p_{jet} are the hadron and total jet momentum along the jet axis, respectively [10]. Jet fragmentation involves soft, long distance physics and is theoretically not well understood. Figure 1.9 shows fragmentation functions for gluon and quark jets for unidentified charged particles measured in an $e^+ + e^-$ experiment. Fragmentation functions for pions and kaons have been parametrized as a function Q^2 for quark flavored (udsb) and gluon jets [58].

In concept, a parton's energy loss is measured via the jet's energy loss (*jet quenching*). In practice, its measurement is not so straightforward. Along with the propagating parton, the radiated gluons also hadronize into jets. Two scenerios are possible: (1) The hadrons due to the radiated gluons and the propagating parton may fall with the same reconstructed jet cone. Then the relevant observable is not the total jet energy, which remains unchanged, but rather the fragmentation function; energy loss will decrease the probability of finding higher momentum hadrons within a jet. (2) The majority of the radiated gluons fall outside the propagating partons's jet cone [90].

In either case, jet reconstruction with energy resolution significantly smaller than the expected energy loss is necessary ($\Delta E \approx 10, \text{GeV}$ for a 40 GeV jet) [105]. Due to the large background of low $p_\perp$ particles in Au+Au collisions [11], jet reconstruction with sufficent energy resolution on an event by event basis may not be possible. Therefore, it has been proposed that since jet energy loss implies a decrease of high $p_\perp$ hadrons (*hadron suppression*), non-Abelian partonic energy loss may be inferred from measurements of inclusive hadron high $p_\perp$ distributions (*spectra*). The lowest order factorized pQCD invariant yield in nuclear A+B collisions at

---

[10]The fragmentation function may also be written in terms of the fractional energy, i.e. $z_c \equiv E_h/E_{\text{jet}}$)

[11]A signicant number of low $p_\perp$ particle may be from low energy *mini jets*.

impact parameter, b, may be written as (ignoring nuclear medium effects):

$$E_h \frac{\mathrm{dN^h}}{\mathrm{d^3p}}(b) = T_{AB}(b) \sum_{abcd} \int \mathrm{d}x_a \mathrm{d}x_b \, f_{a/A}(x_a, Q^2) f_{b/B}(x_b, Q^2) \frac{\mathrm{d}\sigma^{\mathrm{ab \to cd}}}{\mathrm{d}\hat{t}} \frac{D_{h/c}(z_c, Q^2)}{\pi z_c},$$
(1.9)

where $T_{AB} = \langle \mathrm{N_{bin}} \rangle / \sigma_{\mathrm{NN}}$ is the nuclear overlap function [19, 87] and $f_{a/A}(x, Q^2)$ is the *p*arton distribution function (PDF); formally, $f_{a/A}(x, Q^2)$ is defined as the probability density for parton a inside nucleus A to carry a fraction x of the nuclei's longitudinal momentum at scale Q^2. Parton distribution functions have been parametrized using data from deeply inelastic scattering (DIS) experiments with the aid of model assumptions; e.g. EKR-EKS [67] and HKM [96]. However, little data exist for $Q^2 > 1(\mathrm{GeV/c})^2$ at small x and the various PDFs disagree in the regions not constrained by measurements. Energy loss is typically taken into account via a modification of the fragmentation function.

Hadron suppression can be quantified by the *nuclear modification factor*:

$$R_{\mathrm{AA}}(p_\perp) = \frac{\mathrm{dN_{AA}/dydp_\perp}}{(\langle \mathrm{N_{bin}} \rangle / \sigma_{\mathrm{NN}}^{\mathrm{inel}}) \mathrm{d}\sigma_{\mathrm{NN}}^{\mathrm{inel}}/\mathrm{dydp_\perp}}$$
(1.10)

Absent nuclear medium effects, R_{AA} tends to unity at high $p_\perp$; i.e. the hard cross section for A+A collisions is equal to the superposition of independent (incoherent) binary p+p collisions. Final state jet quenching would bring R_{AA} below unity at high $p_\perp$. Two initial state[12] nuclear medium effects are *Cronin* and nuclear *shadowing*.

The Cronin effect [14] refers to hadron production enhancement at high $p_\perp$ for nuclear targets compared to the binary-scaled p+p yield, first observed in p+A collisions; i.e. R_{AA} above unity. (Left panel of Figure 1.10). Cronin is believed to be due to initial state parton multiple scattering within the colliding nuclei, prior to hard scattering. This necessarily enhances the scattered partons' $p_\perp$, thus increasing the yield at high $p_\perp$. Cronin is usually cited as the cause for the observed

---

[12]Prior to hard scattering.
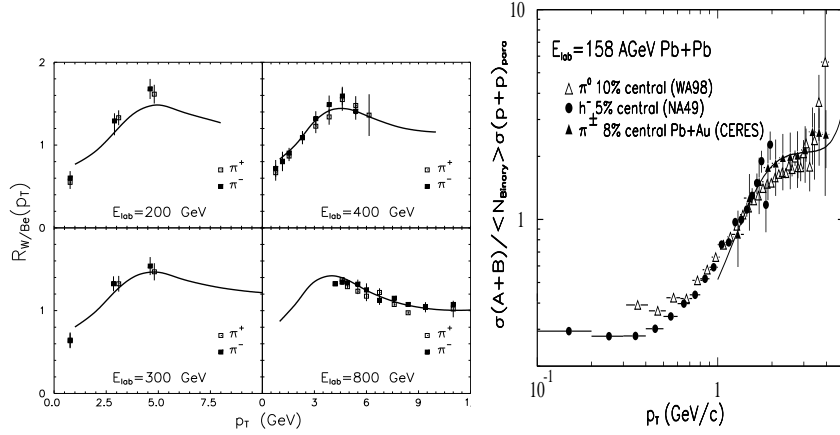
Figure 1.10: Left: In p+A collisions, the ratio of charged pion yield for tungsten over beryllium targets as a function of $p_\perp$, scaled by the atomic number. Curves are theoretical calculations [8]. Data are from [25, 34]. (Figure taken from [8]). Right: R_{AA} measured at the SPS for Pb+Pb collisions at $\sqrt{s_{NN}}$=17 GeV. (Figure taken from [52]). Cronin is cited as the reason why the above ratios are not unity.

R_{AA} above unity at the SPS (Right panel Figure 1.10) [13]. Since Cronin shifts R_{AA} in the opposite direction as jet quenching, there would be no ambiguity between the two nuclear effects in a qualititative interpretation of the data. The Cronin effect at RHIC ($\sqrt{s_{NN}}$=130 GeV) is expected to be significantly smaller than at the SPS ($\sqrt{s_{NN}}$=17 GeV), due to the greater cross section at high $p_\perp$.

Nuclear shadowing refers to the depletion of low $x < 0.1$ partons within a nucleus compared to a free nucleon; i.e. $f_{a/A}(x, Q^2) < f_{a/n}(x, Q^2)$ at small x (Figure 1.11). Consequentally, shadowing leads to a reduction in the high $p_\perp$ hadron yield . Anti-shadowing ($0.1 < x < 0.3$) conversely may increase the high $p_\perp$ yield. Although (extreme) shadowing may potentially mimic the jet quenching signal, models predict that at RHIC energy shadowing's effect on high $p_\perp$ yield is marginal. The Right

---

[13]According to some models, energy loss is allowed at the SPS but any signal is obscured by Cronin.
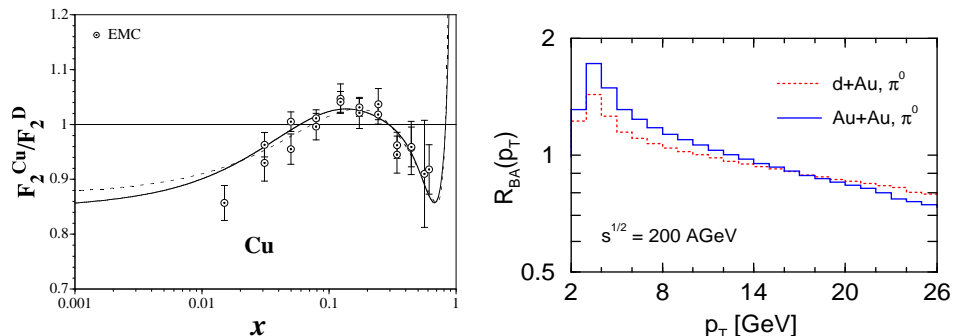
Figure 1.11: Left: Ratio of $F_2^A(x, Q^2) \equiv \sum_q e_q^2(f_{q/A}(x,Q^2) + f_{\bar{q}/A}(x,Q^2))$ for copper over deuteron (sum over quarks, q, only). The depletion in the region $x < 0.1$ is referred as shadowing. (Figure taken from [53]). Right: Predicted R_{AA} in d+Au and Au+Au collisions at $\sqrt{s_{NN}}$=200 GeV/c with Cronin and nuclear shadowing, but no energy loss. (Figure taken from [101])

panel of Figure 1.11 shows a prediction of R_{AA} for Au+Au collisions at $\sqrt{s_{NN}}$=130 GeV when shadowing and Cronin are included (without energy loss). For $2 < p_\perp < 8$ GeV/c, Cronin dominates over shadowing (for the $x > 0.01$ range accessible at RHIC) and R_{AA} remains slightly above unity [14].

Medium induced energy loss is not unique to hot matter. A quark propagating through a cold nucleus in a deep inelastic scattering experiment may scatter off nucleons and radiate away gluons. Typically, the effect of energy loss on the $p_\perp$ distribution is modeled via a modification of the (vacuum) fragmentation function [106]. Therefore, one can compare the fragmentation functions of various target sizes in DIS experiements to assess potential energy loss in cold matter. For example HERMES has measured the ratio of the fragmentation functions for nuclear targets (N^{14}, Kr^{84}) and a deuteron target [102]; model calculations are in relatively good agreement (Figure 1.12). Applying the modified fragmentation function to a cold Au target yields $dE/dx \approx 0.5$ GeV/fm [105].

---

[14]Gluons dominate over quarks for $x < 0.1$. The extent of gluon shadowing is unknown.
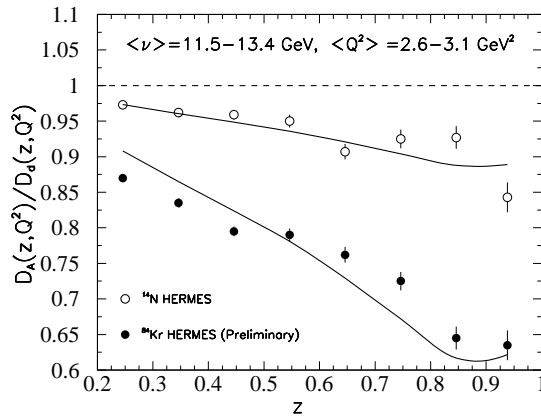
Figure 1.12: In a DIS experiment, the number of charged hadrons per event for a nuclear target (N^{14}, Kr^{84}) over a a deuterium target as a function of fraction of the virtual photon energy (ν) transferred to the hadron (for $\nu > 7$ GeV/c). With a few assumptions, this is equivalent to the ratio of the fragmentation functions. The solid lines are model calculations based on a modified fragmentation function in a (cold) nucleus. (Figure taken from [105])

1.4 Purpose

This thesis reports the measurement of the inclusive charged particle ($h^+ + h^-$) $p_\perp$ spectra for $1.7 < p_\perp < 6$ GeV/c and $|\eta| < 0.5$ as a function of various centrality classes in Au+Au collisions at $\sqrt{s_{NN}}$=130 GeV. Hadron suppression is assessed by comparing the measured yields with both nucleon+nucleon and peripheral Au+Au collisions.

Chapter 2

Experiment

2.1 Relativistic Heavy Ion Collider

The Relativistic Heavy Ion Collider (RHIC) at Brookhaven National Laboratory is an accelerator complex primarily designed for research in relativistic heavy ion collisions [1], capable of reaching a top beam energy of $\sqrt{s_{NN}}$= 200 GeV for Au ions [88],[98]. The flexibility of its design allows a variety of ion species and a wide range of beam energies (low as $\sqrt{s_{NN}}$= 20 GeV for Au ions), affording a systematic survey of initial conditions. In addition, the accelerator complex can generate unpolarized p+p collisons up to $\sqrt{s_{NN}}$= 450 GeV to serve as a baseline for heavy ion physics, deutoron+A collisions to shed light on nuclear shadowing and Cronin, and polarized p+p collisions to study the contribution of quarks and gluons to the proton spin.

Figure 2.1 shows a schematic of the accelerator facility. After passing through the preliminary stages of acceleration, the ions are injected into two concentric rings of circumference 3.8 km, where the final beam energy is reached. Each ring contains ~60 bunches[2], and each bunch contains $\sim 10^9$ ions for Au. The design store time is approximately 10 hours [3] and the design luminosity is $L \approx 2 \times 10^{26} \text{cm}^{-2}\text{s}^{-1}$. The beams cross at 6 interaction points around the ring, at which 4 are occupied by experimental groups: BRAHMS, PHOBOS, PHENIX, and STAR (Solenoidal Tracker at RHIC) [97].

---

[1] Hence the name RHIC

[2] 57 bunches during year 2000 run

[3] typically ~ 5 hours for year 2000 run

100 GeV/u   100 GeV/u

OF BUNCHES: 57
OF IONS/BUNCH: 1x10^9
RF$_{ACC}$: 26.7 MHz, 0.4 MV
RF$_{STORAGE}$: 196 MHz, 6 MV
T$_{FILLING}$: ~1min
T$_{ACC}$: ~1min
$\tau_{\mathscr{S}}$: ~10 hrs

RHIC

PROTON
LINAC

72 MeV/u, Q = +77
STRIPPER

10.8 GeV/u, Q = +79
OF BUNCHES: (3 x 1) x 19
STRIPPER

BOOSTER

AGS

TRANSFER LINE

GOLD BEAM
1 MeV/u, Q = +14

PULSED SPUTTER ION SOURCE
200 μA, >120 μ sec, Q = -1
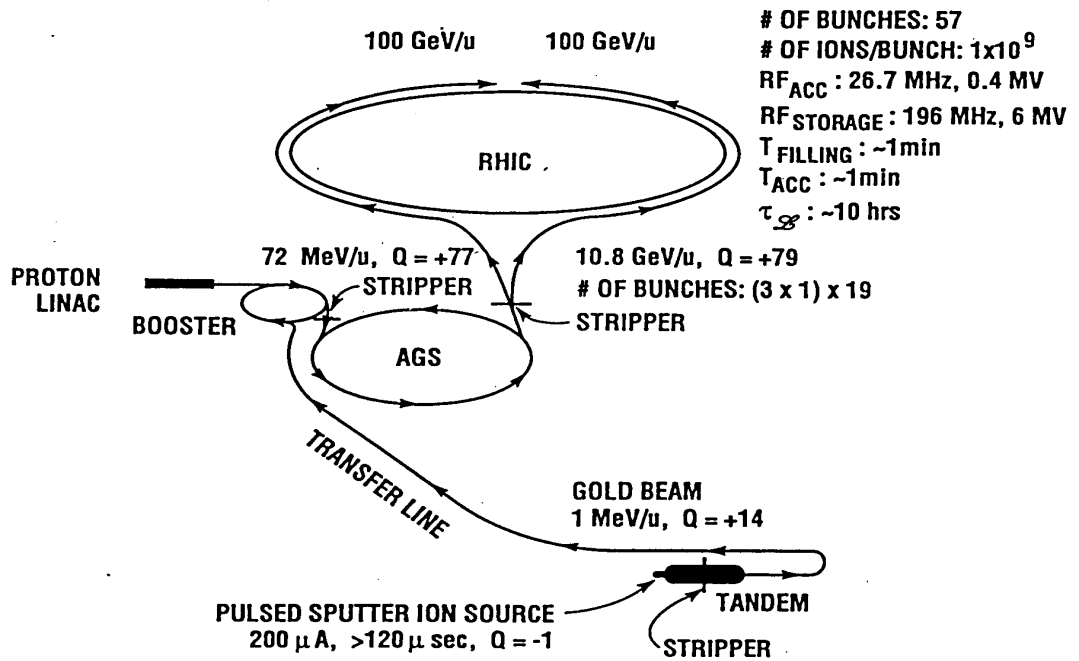
TANDEM
STRIPPER

Figure 2.1: The Relativistic Heavy Ion Collider (RHIC) accelerator facility at Brookhaven National Laboratory (BNL). One of a pair of Tandem Van de Graaff Tandem accelators begins the initial boost of Au ions to ~ 1 MeV/nucleon. After passing through a 700 m Heavy Ion Transfer Line (HITL), the ions are further accelerated to 100 MeV/nucleon in the Booster, stripped to Au^{+77} and sent to the Alternating Gradient Synchotron (AGS). The AGS merges bunches from the Booster to achieve the intensity of $\sim 1 \times 10^9$ Au ions per bunch. Upon exiting the AGS, the ions undergo the final stripping to Au^{+79} and are injected into the RHIC collider at a kinetic energy of 8.6 GeV/nucleon. (Figure taken from [98])
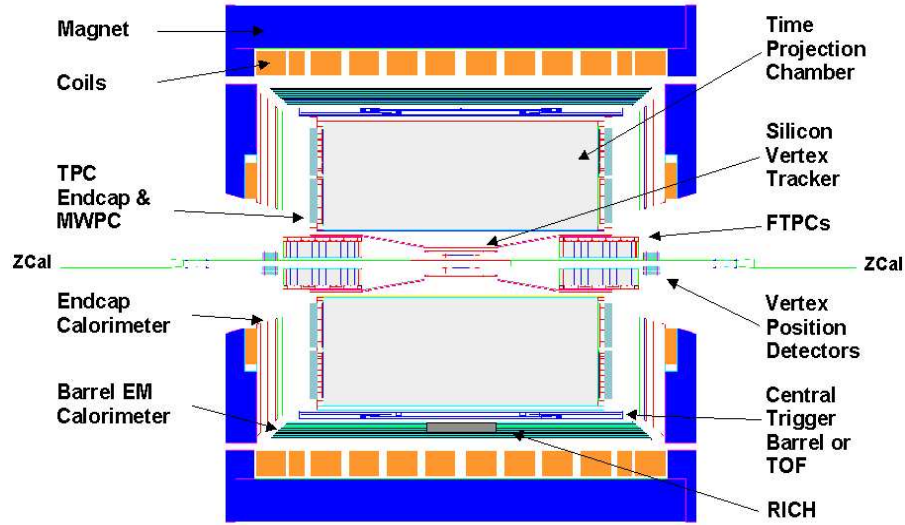
Figure 2.2: STAR Detector System. For the year 2000 data run, the TPC, magnet, RICH, ZDCs, and CTB were operational.

RHIC's first year of operation occurred in year 2000 with the collisions of Au ions at $\sqrt{s_{\mathrm{NN}}} = 130$ GeV at 10% of the design luminosity; this thesis analyzes the data from this run.

2.2 STAR Detector System

The STAR detector system was designed to survey a broad range of physics observables in the complex environment of thousands of particles produced at RHIC (Figure 2.2) [12]. The workhorse is the large acceptance (near full 2π azimuthal converage) Time Projection Chamber (TPC), which tracks charged particles in a uniform magnetic field and identifies particles with momentum $\sim < 1$ GeV/c by sampling ionization energy loss (dE/dx). Particle identification is extended to higher momentum by a Ring Imaging CHerenkov detector (RICH) placed at midrapidity, and in the future by a Time-of-Flight Detector. Decay topologies and secondary
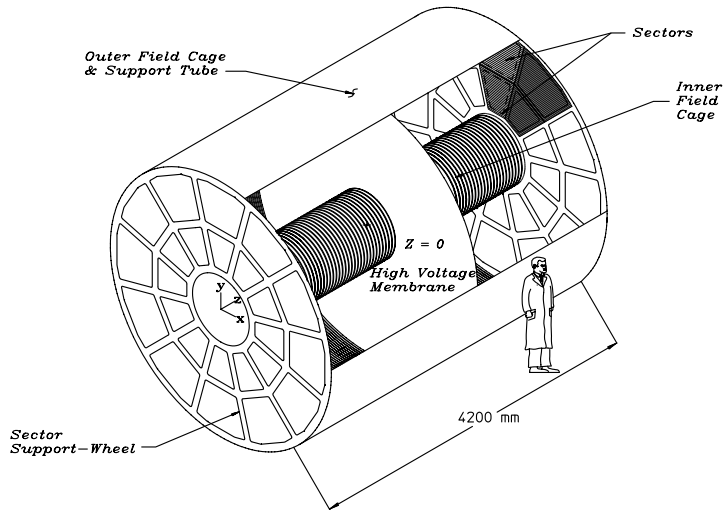
Figure 2.3: STAR Time Projection Chamber

vertices in the TPC are used to identify short lived strange hadrons, abetted in year 2001 by a Silicon Vertex Tracker (SVT) around the interaction point. Also operational in year 2001 was an electromagnetic calorimeter (EMC) measuring π^0, electrons, and photons, along with a Foward Time Projection Chamber (FTPC) tracking charged particles within $2.5 < |\eta| < 4$. Gross event characterizations for triggering was provided in 2000 by a pair of Zero Degree Calorimeters (ZDCs) detecting spectator neutrons and a Central Trigger Barrel (CTB) measuring scintillation photons. In 2001 two Beam-Beam Counters enabled triggering on event vertex position and in defining centrality classes.

For the year 2000 data run, the TPC, magnet, RICH, ZDCs and CTB were installed and operating.

2.2.1 Time Projection Chamber

The main tracking device in the STAR detector system is the Time Projection Chamber (TPC), a cylindrical gas filled drift chamber, 4.2 m long with an inner and outer radius of 0.5 m and 2 m, respectively (Figure 2.3) [6, 11, 12, 32]. The TPC maps the trajectory of a charged particle by recording the 3 dimensional positions of ionized electrons along the particle's path. The electron clouds drift to the readout system at the two ends of the TPC under a uniform electric field of ~ 145 V/cm, whereupon the electrons are multiplied around anode wires and their charge induced on small cathode pads. Pad signals are used to locate the spatial position of the ionized electrons in the plane transverse to the electric field (xy), while the time difference between the collision and the charge collection (combined with the drift velocity) determines the position along the field (z). The momentum of the particle in the plane transverse to the beam line $(p_\perp)$ is calculated from the bending radius in a uniform 0.25 T magnetic field, parallel to the electric field[4]. As the TPC has 136608 pads and as the signal is digitized into a maximum of 512 time bins (*buckets*) [5], the TPC is segmented into as many as $69,943,300$ *pixels*.

The TPC is separated into two symmetric drift regions by a thin cathode Central Membrane (CM) held at -28 kV. In the STAR global coordinate system, the CM is located $z = 0$ cm, and the East and West TPC correspond to the $z < 0$ and $z > 0$ regions, respectively. Along with the CM, the electric field is defined by two end caps at ground[6] and two concentric cylinders, the Inner (radius 50 cm) and Outer (radius 200 cm) Field Cages, which help maintain a uniform electric field with a series of 182 equipotential rings. In addition the IFC, OFC, and the end caps determine the gas volume. The material and construction design were

---

[4]Design strength is 0.5 T
[5]380 time buckets filled in 2000 run
[6]Note that the drift field points in the opposite direction for each TPC half.
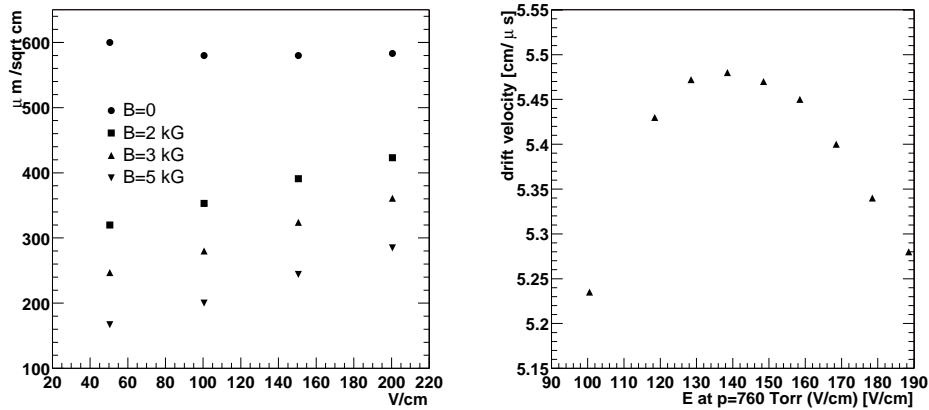
Figure 2.4: Left: P10 transverse diffusion as a function of electric field at TPC working conditions for $B = 0, 2, 3, 5$ kG. Right: P10 drift velocity as a function of electric field. (Figure from [11])

chosen, apart from cost effectiveness, to minimize multiple Coulomb scattering, photon conversions, and hadronic secondary particle production. For example, the Inner Field Cage has a radiation length of 0.5%, while the Outer Field cage has a radiation length of 1.3%; thicker material was used in its construction to supply structural support for the TPC and the Central Trigger Barrel.

Filling the TPC chamber is P10 gas (10% methane, 90% argon). The criteria for the choice of gas (primarily the organic contribution), included minimization of diffusion and multiple scattering, and operation near atmospheric pressure [7]. For example, low diffusion during drift is desired as the size of the electron cloud is roughly proportional to the position resolution. For 0.5 T magnetic field the transverse and longitudinal diffusion coefficients are 230 μm/$\sqrt{\mathrm{cm}}$ and 320 μm/$\sqrt{\mathrm{cm}}$, respectively (Left panel of Figure 2.4). However, the principal reason for the choice of P10 was the high drift velocity at low electric field. A high drift velocity is preferred since it reduces the buildup of positive ion space charge from distorting the electron

---

[7]2 mbar above atmosperic pressure

22
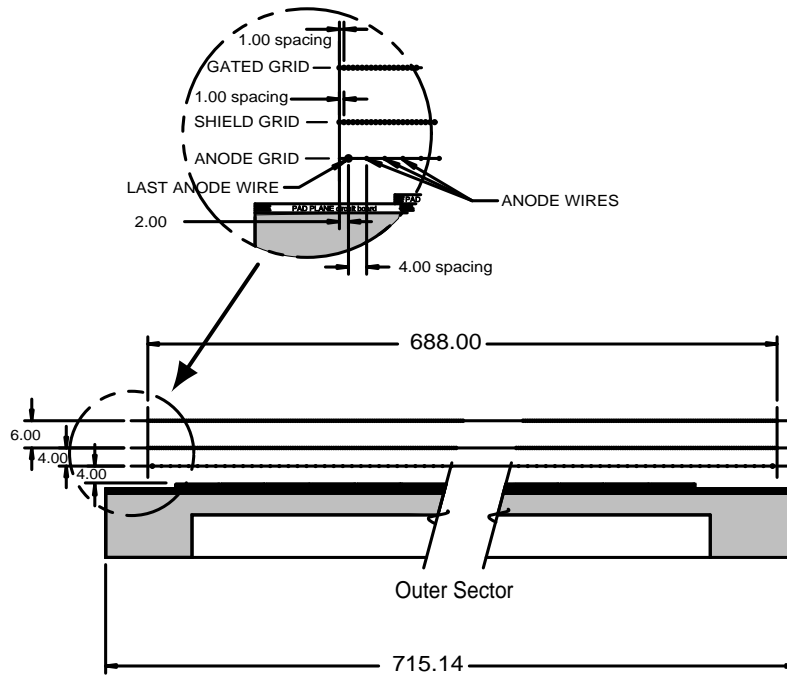
Figure 2.5: Multi-Proportional Wire Chamber for the outer sector.

drift, especially during high luminosity operation; and a low electric field eases the field cage design. The Right panel of Figure 2.4 shows a plot of drift velocity as a function of electric field strength. to lessen variations due to changes in pressure and temperature, the electric field strength was chosen so that drift velocity was slightly below the peak of the function (saturation region). The working drift velocity was ~ 5.44 cm/μs [8], periodically calibrated during data taking to a precision of 0.001 cm/μs.

The (signal) readout planes at the two end caps are based on Multi Wire Proportional Chambers (MWPC), which consist of a plane of segmented cathode pads lying behind 3 wire planes: the outer gating grid, the middle shield grid, and the inner anode wire plane (Figure 2.5). As an electron cluster approaches the

---

[8]Maximum drift time of ~ 36 cm/μs.

readout plane, electric fields around 20 μ m diameter anode wires in the MWPC begin an avalanche process where the energized electrons ionize the gas thereby releasing more electrons in a feedback loop. The multiplicative factor in the increase of electrons (gas gain) is controlled by the anode wire voltage [9]. The chosen voltage results in a 20:1 signal to electronic noise ratio for minimum ionizing particles (e.g. high $p_\perp$ hadrons). The ratio is high enough to achieve sufficient position resolution, while the corresponding gas gain of $\sim 10^4$ is low enough not to degrade the dE/dx resolution [10]. The motion of the positive ions left by the avalanche induce a mirror charge on the pads which is then processed by the electronics system.

The outer gating grid controls the entry and exit of electrons and ions in the MWPC. When an event is 'triggered' for data taking, the gating grid is 'open' (wires held at the same potential) to allow the entry of the drift electrons. Otherwise, the gating grid is 'closed' (wires alternate potential) which both captures positive ions in the MWPC, preventing the distortion of the drift field, and stops ionization amplification when data is not being recorded to reduce the aging of the MPWC. Lastly, the shield grid primarily serves to end the electric field and capture ions in the MPWC. Its secondary role is to shield the pads from em interference.

Each end cap is divided into 12 readout plane modules, or sectors, with a 3mm spacing between sectors (Figure 2.7). A sector is divided into an inner subsector and outer subsector, with the padplanes are arranged in rows across a subsector. The inner subsector consists of 13 pad[plane]rows, while the outer subsector has 32 padrows, for a total of 45 possible measured spatial points on a track (Figure

---

[9]i.e., within a voltage range, the net increase of electrons is *proportional* to the initial number of electrons. Hence the name MWPC.

[10]Gas gains are ~ 3770 for the inner subsectors and ~ 1230 for the outer subsectors. See below for sector definition.

Outer Pads
6.2 mm x 19.5 mm
Total of 3,942 Pads

6.7 x 20 mm Centers

Inner Pads
2.85 mm x 11.5 mm
Total of 1,750 Pads
Row 1 thru 8 on 48 mm Centers
Row 8 thru 13 on 52 mm Centers
Cross Spacing 3.35 mm

600.00 mm from DETECTOR CENTER

87 x 3.35 = 291.45 mm

143 x 6.7 = 958.10 mm

97 x 6.7 = 649.90 mm

183 x 3.35 = 613.05 mm

3.35 mm CROSS SPACING

48.00 mm RADIAL SPACING

52.00 mm

6.70 mm CROSS SPACING
(7 x 48) + (5 x 52) = 596.00 mm

20 mm RADIAL SPACING
31 x 20 = 620.00 mm

1271.95 mm from DETECTOR CENTER

Figure 2.6: Padplane geometry for one sector.

OUTER SECTOR

INNER SECTOR

DETECTOR

CENTER LINE

12 × 30.0°

12 per WHEEL
TOTAL 24

STAR TPC WHEEL
DIAMETER 4m
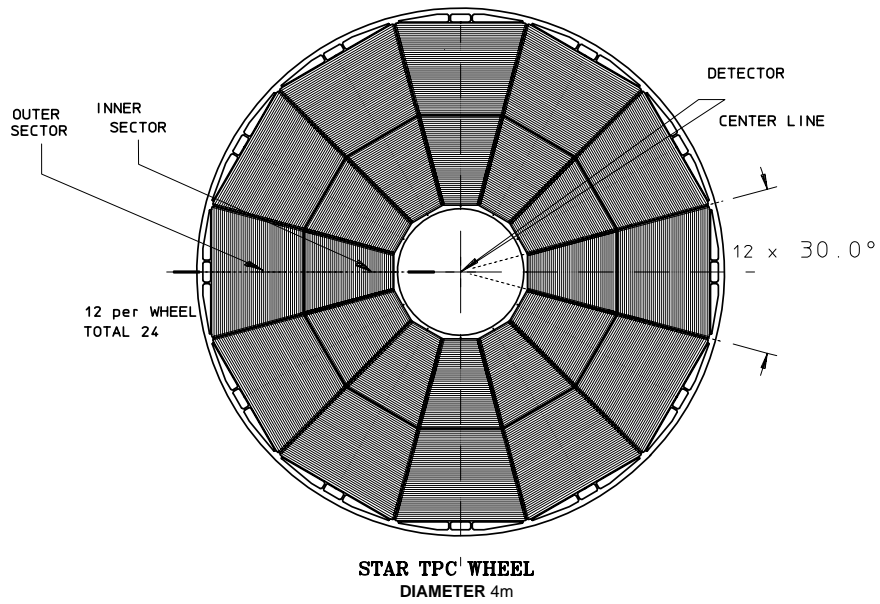
Figure 2.7: Sector layout for one endcap.

25

2.6). The outer subsector has negligible spacing between padrows to improve dE/dx resolution via a greater number of ionization samplings. Both the distance between the anode wires and the pad plane, and the width of a pad along the wire direction were chosen so that the majority of the charge is induced on 3 pads in order to optimize the determination of the hit position in the reconstruction phase, primarily for nearly straight (i.e. high $p_\perp$) hadrons. The pad geometry for the outer subsector is 6.20 mm along the anode wire x 19.5 mm perpendicular to the wire. To improve two-track resolution the inner subsector, where track density is greater, consists of smaller pads (2.85 mm x 11.5 mm).

2.3   Electronics

Pad signals are amplified, shaped, sampled in time, and digitized by Front End Electronics (FEE) cards plugged into the padplane, each processing signals from $\sim$ 5 pads [31]. The FEE cards are based on two custom chips, the SAS (STAR preAmplifier/Shaper) and the SCA/ADC (Switched Capacitor Array/ADC). The total electronic noise is limited to $\sim$ 1000 electrons to maintain a 20:1 signal to noise ratio with a reasonable gas gain (see above). The step functions generated by the preamplifier are shaped to a near gaussian within a $\sim$ 230 ns FWHM window to match a 2m drift signal width, where the chosen shaping time helps smooth fluctuations in the cluster position measurements. In addition, the shaper removes the signal's long tail ($\sim 60\mu$s) resulting from the slow dispersal of the positive ions in the MWPC. The 512 capacitor array samples and stores the signal in time. The sampling frequency is chosen so that the bulk of a long drift signal is spread across 3 time buckets to optimize hit resolution[11]. After the signals for each pad-time bucket (*pixel*) are digitized into 10 bit words (ADC counts), the data are relayed to the readout board, which provides trigger and control monitoring, and then

---

[11]Each time bucket is $\sim$ 70 ns.

subsequently sent over a 1.2 Gbit/s fiber optic link to the data acquisition system (DAQ).

2.4   Trigger

The trigger system has the task of selecting events of interest among the possibly thousands (Au+Au) or hundreds of thousands (p+p) of interactions per second. First, a trigger system is necessary due to finite bandwidth of data transfer to storage. For example the interaction rate for Au+Au collisions at design luminosity is ~ 1 kHz [12], while DAQ transfers data to storage at ~ 50 Hz (transfer rate of ~ 50 MB/s translated for a high multiplicity Au+Au event data). Second, a trigger system is desirable in order to select events or processes with a small cross section, such as high $p_\perp$ jets or collisions at small impact parameter.

The STAR trigger system is based on 4 possible sequential decision making levels [27]. The Level 0, 1, and 2 triggers processes information from 'fast' detectors (e.g. ZDC, EMC) and the Level 3 (L3) trigger analyzes data from 'slow' detectors (e.g. TPC). Each level can accept or veto an event, where the decision time limit is based on the characteristic time of a process along the chain from interaction to TPC signal digitization. For example, the Level 0 trigger accepts/vetos an event within each bunch crossing (~ 107 ns), Level 1 within the TPC maximum drift time ($\sim 36\mu$s), and Level 2 within the TPC signal digitization time (~ 8ms). Along with longer decision times, each succeding level bases the selection decision on more finely grained information, culminating in the Level 3 trigger which reconstructs events in real time (within ~ 10ms).

For year 2000, the two principal fast trigger detectors were a pair of Zero Degree Calorimeters (ZDC East/West) and a Central Trigger Barrel (CTB); they

---

[12]$I = L\sigma_{\mathrm{Au+Au}}$ where $L = 0.2\mathrm{mb}^{-1}\mathrm{s}^{-1}$ and a hadronic cross section of $\sigma = 7200$mb was assumed
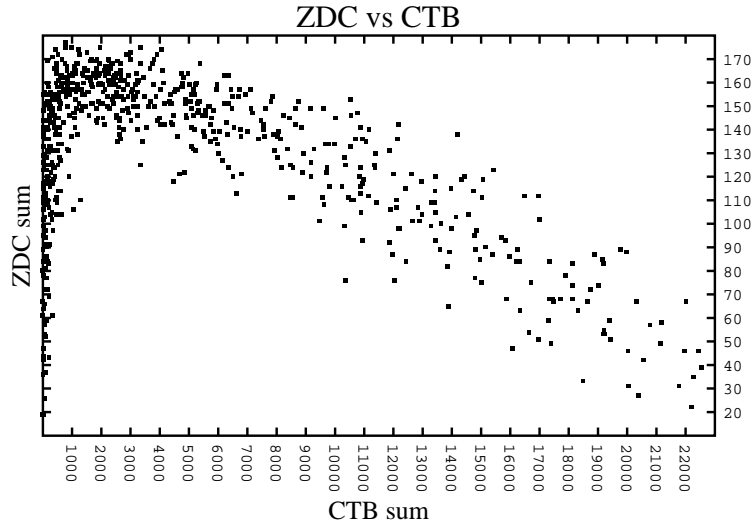
Figure 2.8: ZDC sum vs CTB sum for minimum bias triggered events. Lower ZDC sum/higher CTB sum correlates with smaller impact parameter. (Figure taken from [27])

provided information for the L0 trigger [13]. The hadronic ZDCs are symmetrically situated along the beam line $\sim$ 18 m from the TPC midpoint, where the accelerator dipole magnets bend charged fragments away from the ZDC's angular acceptance of $\sim$ 2 mrad. Hence the ZDCs measure spectator neutrons [14] which were found to be correlated with the event geometry for impact parameters less than $\sim$ 6 fm. Surrounding the TPC is the CTB which detects charged particles within an acceptance of $-1 < \eta < 1$ and 2π in azimuth. Figure 2.8 shows a plot of ZDC sum vs CTB sum. For higher multiplicity events (higher CTB sum/smaller impact parameter), ZDC and CTB sums are anticorrelated. For low multiplicity events (CTB sum < 1500), the relationship becomes ambiguous as nucleons break up into multiple complex fragments resulting in large fluctuations in the number of unbound

---

[13]In addition, the TPC's Mult-Wire Proportional Chambers aided in triggering by measuring charged multiplicity for particles passing through the chambers ($1 < |\eta| < 2$)

[14]neutrons not 'participating' in the collision

28

neutrons.

Two main triggers were used for the analysis.

- minimum bias (minbias)

  The trigger selected any event with a hadronic interaction (with minimum bias). It required an arrival time coincidence of ZDC East and West signals above a threshold, generally 40% of a single neutron peak. Coincidence was demanded to limit Coloumb dissociated and beam+gas events. The trigger was about $94 \pm 2\%$ efficient (see Analysis chapter).

- central

  The trigger logic required ZDC coincidence and CTB ADC sum > 15000. The CTB inequality corresponded to the top $\sim 15\%$ of the $dN_{event}/dCTB$ distribution.

Chapter 3

Reconstruction

The reconstruction software transforms raw data into meaningful physics observables, such as charged particle trajectories (*tracks*) and the spatial position of the interaction point. For the TPC, tracks are reconstructed via *hits*. A hit is the 3 dimensional position where a charged particle nominally crosses a padrow plane. Since the TPC has 45 padrow planes per sector, a track may be composed of a maximum of 45 hits [1]. Lower momentum particles are identified through their ionization energy loss per length (dE/dx) and short lived hadrons (Λ ,K_S^0 ,etc) through their decay topologies. The final event reconstruction integrates data from each detector (e.g. SVT, TPC, FTPC), but only TPC specific information will be discussed below since it was the sole operational tracking detector in 2000. Figure 2.3 shows the STAR global coordinate system [2].

3.1   Hits

The induced charge signals from the ionized electrons along a particle's path are digitized in pad-time bucket space, each unit referred as a *pixel* [70]. Calculating hit positions begins with finding *clusters*, regions of contiguous pixels above an ADC threshold (Figure 3.1) on a padrow. Then the pixel corresponding to a local ADC maximum (*peak*) within each cluster is identified. Clusters containing more than

---

[1]However the majority of tracks has less than the 45 hits due to, among other reasons, finite track curvature and reconstruction inefficiency. In addition, padrow 13 was removed in the track fitting stage. See the Corrections section.

[2]Look closely at the left endcap.
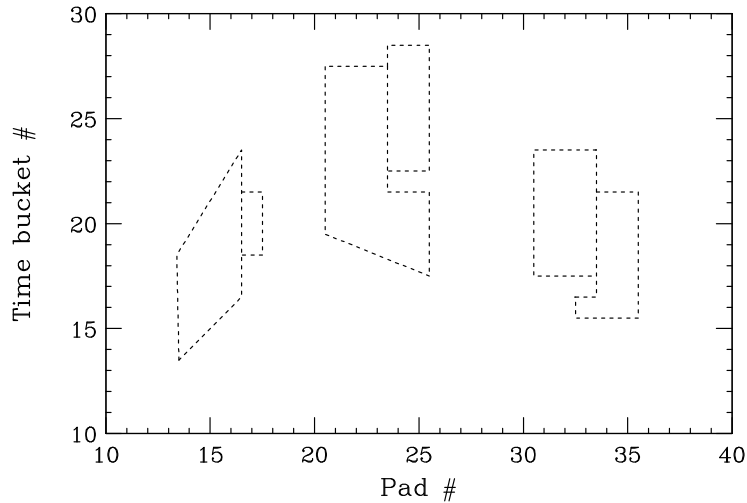
Figure 3.1: Clusters in pad-time bucket-ADC space. Larger 'boxes' in the figure correspond to pixels with higher ADC values. Clusters with multiple peaks have been deconvoluted. (Figure taken from [70])

one peak, which may occur when two or more tracks are spatially close and their ionization deposits overlap, are separated (*deconvoluted*) into multiple hit positions. A helpful analogy is that the pad-time-ADC space is like a mountainous terrain, with the ADC counts representing the altitude. The hit position then corresponds to a local mountain peak position.

Given a cluster and a peak, the hit position is first calculated in local pad coordinates. The position along the padrow is determined by a three point Gaussian parametrization:

$$x = x_0 + \frac{w}{2} \frac{\ln h_a/h_b}{\ln h_{\text{peak}}^2/h_a h_b},$$
(3.1)

where w is the pad width, h_{peak} is the ADC sum in time for the pad containing the peak, x_0 is the position of that pad, and h_a, h_b are the ADC sums of the two adjacent pads. In the direction perpendicular to the padrow, the hit position is simply the midpoint of the pad. The position in the drift direction is calculated by
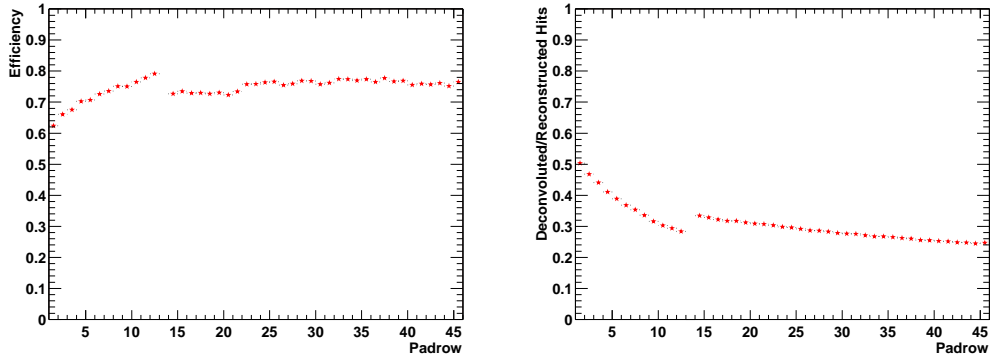
Figure 3.2: Left: Hit finding efficiency per padrow. Right: # Deconvoluted hits/# Reconstructed hits per padrow. Both figures are for central ($b < 3$ fm) HIJING events. Only hits on $p > 100$ MeV/c tracks were considered.

an ADC weighted mean:

$$t = \frac{\sum_i t_i P_i}{\sum_i P_i} - t_{\text{offset}}, \qquad (3.2)$$

where P_i is the ADC sum in time bucket i and t_{offset} is the time delay of the first time bucket relative to the event trigger [3]. The hits' local coordinates are transformed into global coordinates according to the TPC geometry and detector calibration information (e.g. drift velocity and time offset to convert time buckets to global z). Position errors were assigned to hits based on a parametrized function of the measured hit residual distributions (the distance between a hit position and the track model. See below).

To assess the performance of the hit finding software, HIJING Monte Carlo generated events were passed through a TPC response simulator[4]. The Left panel of Figure 3.2 shows the hit finding efficiency per padrow for central ($b < 3$ fm) events. Due to higher track density closer to the interaction point, the fraction of

---

[3]The time offset includes the trigger delay, time for the electron to drift from the gating grid, and the signal shaping by the front end electronics [32].

[4]See Appendix B for a brief description of the simulation chain.
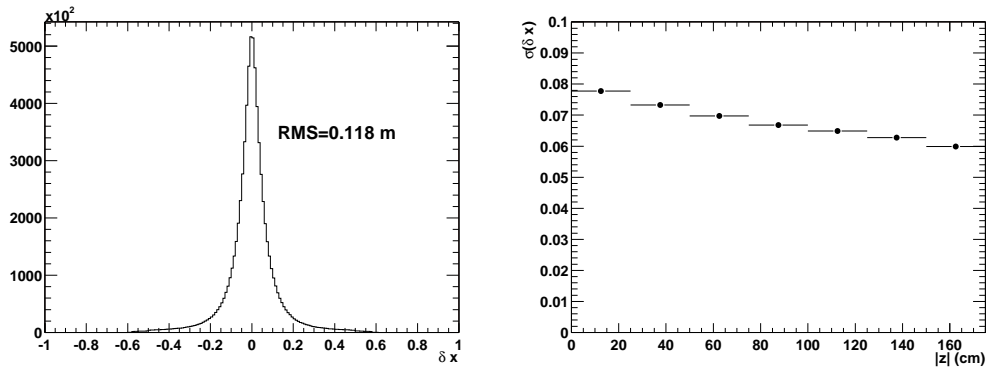
Figure 3.3: Left: Hit position resolution (δx) in the padrow direction. Right: Sigma of a gaussian fit to δx as a function of global $|z|$. Only tracks with $|\eta| < 0.3$ were included.

deconvoluted hits is greater for the inner padrows as illustrated in the Right panel of Figure 3.2. The Left and Right panels of Figure 3.3 show the hit position resolution in the padrow direction (δx) and the sigma of gaussian fit of δx as a function of $|z|$, respectively. Integrated over drift distance, the RMS of δx and δz are $\sim 120\,\mu$m and $\sim 160\,\mu$m, respectively.

3.2   Tracks

3.2.1   Track Finding

Since $\sim 10^5$ hits are found in central collisions, identifying particular charged particle trajectories amid the slew of hits is a nontrivial task. The basis of the STAR algorithm to recognize track patterns was developed by the ALEPH TPC, its approach being to find and reconstruct a track in piecemeal fashion.

Track finding begins in the outermost padrow where track density is lowest and proceeds inwards [83]. The initial step is the formation of simple three-hit links, called roots (Left panel Figure 3.4). A hit in the outermost padrow and is successively linked with hits in the next two inner padrows (allowing for possible
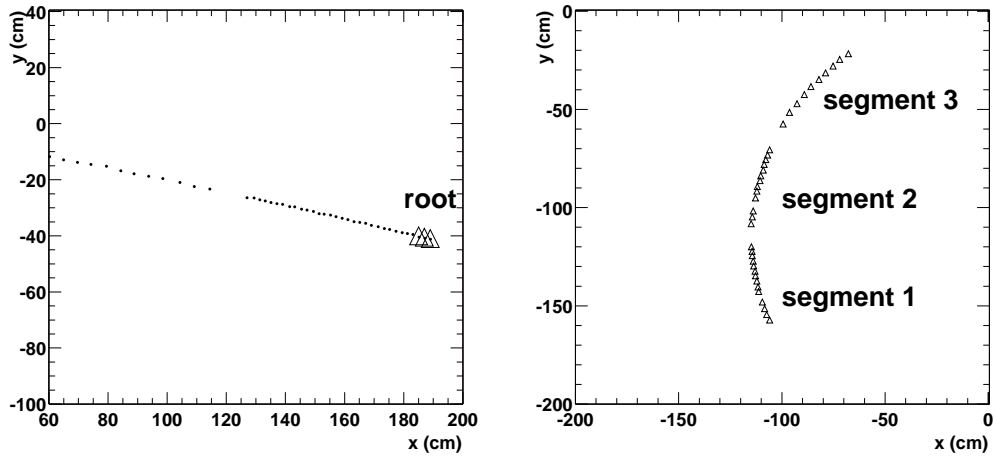
Figure 3.4: Left: Root (triangle markers) for a $p_\perp$ =1 GeV/c track. Right: Three track segments for a $p_\perp$ =100 MeV/c track.

padrow gaps), by applying spatial cuts in the xy (bend) plane and in z.

Each root is then linearly extended into a track *segment* by calculating the root's straight line intercept with the next inner padrow, once again taking into account padrow and sector gaps. If a hit is found within a specified distance from the intercept position, it is added to the segment and removed from the available hit pool. The linear extrapolation continues to the next inner padrow until the procedure fails or the innermost padrow is reached . Once the track segment is formed, the hits are fit with a helical track model (see below). For each track segment originating from a common outer root hit, the best candidate is stored and its points removed from the hit pool. The algorithm is repeated by searching for the next root row by row. After all track segments are identified, segments may be extended radially inwards and/or outwards. In addition shorter track segments may be merged into one helix (Right panel Figure 3.4). This occurs primarily for low $p_\perp$ tracks with small radii of curvature; virtually all high $p_\perp$ tracks are composed of one segment.

34
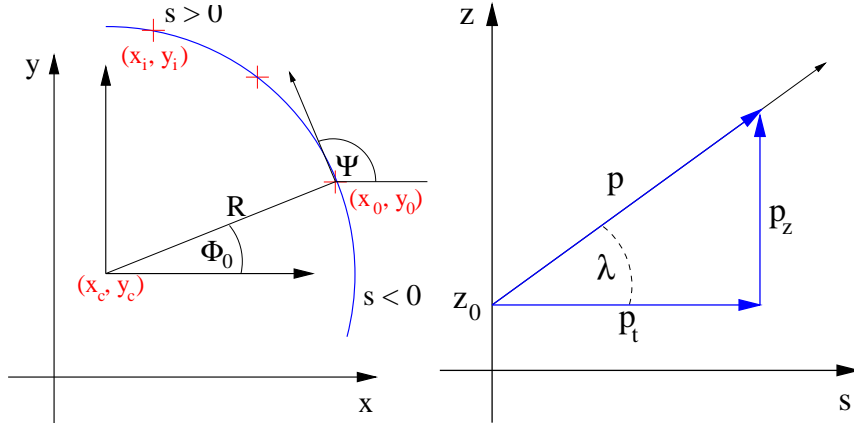
Figure 3.5: Left: Circle fit in the xy plane. Right: Line fit in sz plane, where s is a track's path length.

3.2.2 Track Fitting

To first order in a homogeneous magnetic field, the trajectory of a charged particle is well described by a simple helix. As an initial step, the helix is fit in two components. The component in the xy plane, transverse to the magnetic field, is fit with a circle, while the component in the sz plane, where s is the track length, is fit with a straight line (Figure 3.5). Only tracks with at least 5 points are accepted to ensure that the 5 helix parameters are uniquely defined.

In the xy plane, a circle may be fit by the Least Squared Method with the functional

$$L(a, b, R) = \sum_i \rho_i^2 = \sum_i \left(\frac{\sqrt{(x_i - a)^2 + (y_i - b)^2} - R}{\sqrt{w_i}} \right)^2 \qquad (3.3)$$

where a, b are coordinates of the circle center, R the circle radius, x_i, y_i the hit coordinates, and w_i the weights associated with each hit. However, the non-linearity of ρ_i leads to unwieldy CPU times. To increase speed while maintaining reasonable

35

accuracy and stability, the functional minimized is [10]

$$K(a, b, R) = \sum_i \frac{1}{w_i} \left(\frac{x_i^2 + y_i^2 - 2ax_i - 2by_i + a^2 + b^2 - R^2}{R} \right) \qquad (3.4)$$

The initial helix parameters are then passed through a Kalman Filter [45, 69], which modifies the helix in two stages. The first *filter* stage incorporates second order deviations to the helix model due to multiple Coloumb scattering and energy loss through detector material. For high $p_\perp$ tracks, multiple scattering's effect on the track model, and consequently the momentum resolution, is marginal (see below). The second *smoothing* stage removes outliers and refits the track, the criteria for hit removal based on the χ^2 of the fit using the full 5 parameter error matrix. After two iterations, with the second applying stricter outlier cuts, the best estimate of the helix parameters at the first measured point is recorded.

Figure 3.6 shows padrow hit residuals as a function of crossing angle [5] for $p_\perp > 1.5$ GeV/c tracks. Hits on the inner and outer subsectors for short ($|z_{\text{drift}}| < 50$ cm) and long ($150 < |z_{\text{drift}}| < 200$ cm) drift are plotted separately.

For tracks nominally originating from the interaction point (*primary tracks*), two classes of fits are applied. The first, *global fit*, merely uses the TPC measured points associated with padrow crossings. The second, *primary fit*, uses the TPC hits and in addition constrains the track origin at the interaction point. This leads to an improvement in the momentum resolution by a factor ~ 2 (see below).

3.2.3 Momentum Resolution

For a particle with electric charge $q = ze$, the momentum in the bend plane (equivalent to $p_\perp$ in the STAR geometry) in a uniform magnetic field strength B

---

[5]The crossing angle is defined as the angle between the track and the plane perpendicular to a padrow.
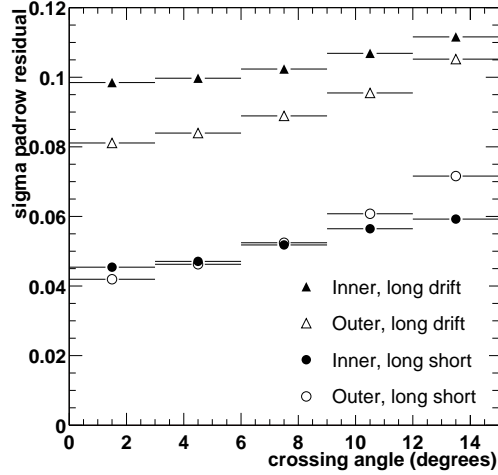
Figure 3.6: Padrow hit residuals as a function of crossing angle for $p_\perp > 1.5$ GeV/c tracks.

(T), is related to the radius, R (m), of the track circle by [50]

$$p_\perp = |zB\kappa|R \quad (\text{GeV/c}), \tag{3.5}$$

where $\kappa \approx 0.2998\,\text{m}^{-1}\text{T}^{-1}(\text{GeV/c})$.

The distribution '(true $p_\perp$ − reconstructed $p_\perp$)/true $p_\perp$' is not gaussian but is rather skewed towards higher $p_\perp$, with the asymmetry more pronounced for distributions with larger RMS. On the other hand, the corresponding distribution in curvature, $k \equiv \frac{1}{R} \propto \frac{1}{p_\perp}$ is a near gaussian (Figure 3.7). For a track with many (≥ 10) uniformly spaced measured points, the fractional curvature resolution (error) may be written as

$$(\delta k/k)^2 = (\delta k_{\text{res}}/k)^2 + (\delta k_{\text{ms}}/k)^2\,, \tag{3.6}$$

where δk_{res} is the curvature error due to measurement resolution and δk_{ms} is the error due to multiple scattering in material. In particular,

$$\frac{\delta k_{\text{res}}}{k} = \frac{\sigma_\phi p_\perp}{z\kappa BL^2}\sqrt{\frac{720}{n+4}}\,, \tag{3.7}$$
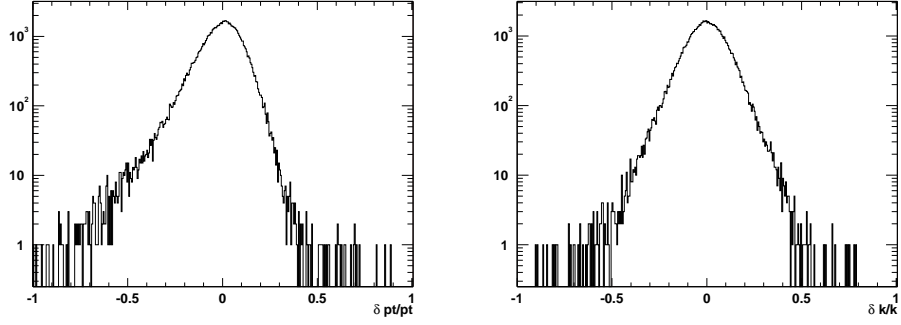
Figure 3.7: Left: $\delta p_\perp / p_\perp$ for $5 < p_\perp < 6$ GeV/c for central embedded events. Right: $\delta k / k$.
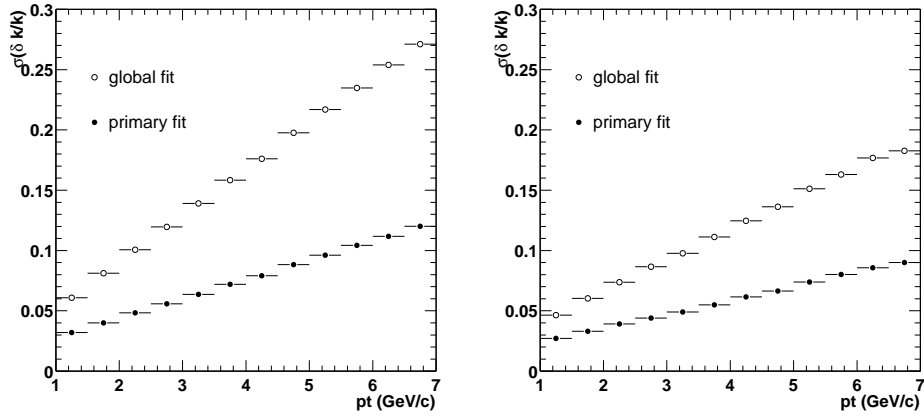
Figure 3.8: Left: $\sigma(\delta k / k)$ as a function of $p_\perp$ for primary and global fit tracks for (0-5%) central events. Right: The corresponding plot for (60%-80%) peripheral events.
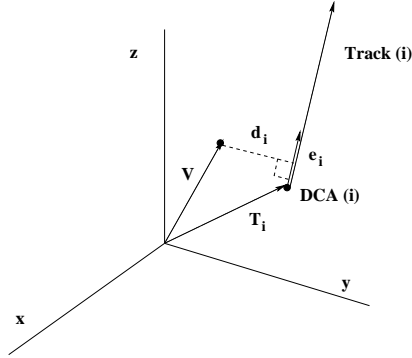
Figure 3.9: (Figure taken from [91])

where σ_ϕ (m) is the error for each measured point (hit) perpendicular to a particle's trajectory, L (m) is the track length in the bend plane, and n is the number of position measurements. Including the interaction point as a constraint on the track's origin (i.e. primary fit) modifies the numerator under the radical to 380. The curvature error due to multiple scattering is approximately

$$\frac{\delta k_{\mathrm{ms}}}{k} \approx \frac{0.016}{0.3LB\beta}\sqrt{\frac{L}{X_0}} \, , \tag{3.8}$$

where X_0 is the radiation length of the scattering medium and β is the velocity in units of c. Since the TPC does not have uniformly spaced points, the above formulas are approximate. Note that for high $p_\perp$ tracks, the curvature error due to multiple scattering is inconsequential. For $B = 0.25$ T, $L = 2$ m, and $X_0 = 110$ m (P10 gas), $\delta k_{\mathrm{ms}}/k$ is ~ 0.01 for $p_\perp > 2$ GeV/c. Figure 3.8 shows $\sigma(\delta k/k)$ as a function of $p_\perp$ for global and primary fit tracks for $B = 0.25$ T. The Left panel is for central events while the Right panel is for peripheral events.

3.3 Event Vertex

The event, or primary, vertex position is the nominal position of the interaction point and serves two main purposes. First, the event vertex allows the identification of tracks originating from the interaction point (primary tracks). Second, a primary track is fit with the event vertex as a constraint, improving the momentum resolution (see above). Tracks with a Distance of Closest of Approach (DCA3d) to the event vertex less than 3 cm are flagged as primary tracks. Two separate software modules, EVR and LMV [6], are used to reconstruct the event vertex depending on the event multiplicity. EVR is applied for events with 10 or more tracks and LMV otherwise. Only EVR will be described below [75, 91].

The event vertex is reconstructed via an iterative procedure with increasingly stringent track cuts. The initial seed of the event vertex position is determined from the weighted mean in x, y, and z of the tracks' DCA3ds to the beam line in the transverse plane. Tracks with ≥ 25 fit hits near the candidate vertex position are linearized in order to achieve an analytical, and thus faster, solution. The event vertex is found by the Least Square Method, minimizing

$$|\xi|^2 = \sum_i \frac{d_i^2}{w_i} \tag{3.9}$$

where

$$d_i = |(\vec{V} - \vec{T_i} \times \hat{e}_i|. \tag{3.10}$$

T_i is the DCA3d to the candidate vertex $\vec{V}$ and $\hat{e}_i$ is the unit momentum vector for each track (Figure 3.9). The weight w_i incorporates effects due to Multiple Coluomb Scattering and possible track helix parameter uncertainties with a minimum value of $w_i = (0.1\text{cm})^2$; however, the version used in the present analysis did not include the track uncertainties. After outliers are removed, the calculated vertex position

---

[6]Event Vertex Reconstructer and Low Multiplicty Vertex [finder], respectively

40
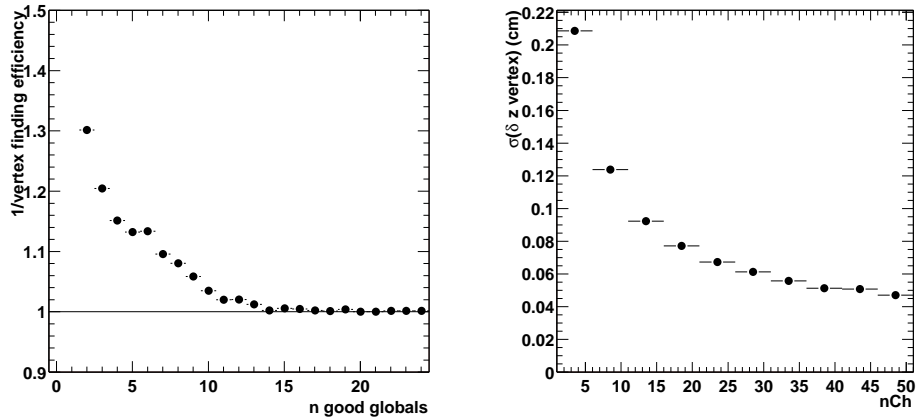
Figure 3.10: Left: Inverse of the vertex finding efficiency as a function of tracks with ≥ 25 fit hits. Right: sigma of the z vertex resolution as a function of n_{ch}. Plots made from peripheral HIJING events.

serves as the seed for the next iteration. The event vertex position is obtained after 3 iterations.

The left panel of Figure 3.10 shows the the inverse vertex reconstruction efficiency from simulated HIJING events as a function of tracks with ≥ 25 fit hits. The Right panel shows the z vertex resolution vs charged multiplicity (n_{ch}) within $|\eta| < 0.5$ for low multiplicity events. At high multiplicy ($n_{ch} \sim 600$), the vertex resolution is $\sim$200 μm.

3.4   Track Geometry

Track geometry is shorthand here for the geometry of a particle's trajectory. For high $p_\perp$ (large radius) tracks where only a small arc is subtended by the measured points, it is instructive to consider the sagitta, s, defined as the deviation from a straight line (chord) connecting the first and last point (Left panel Figure 3.11).

41
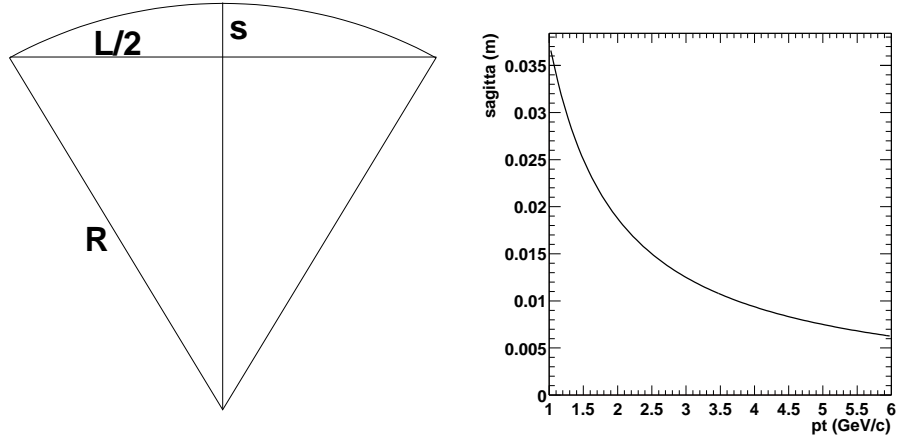
Figure 3.11: Left: Geometric definition of the sagitta, s. Right: Sagitta as a function of $p_\perp$ for $L = 2$ m.

Assuming $L >> s$, one can write

$$s \approx \frac{L^2}{8r} \tag{3.11}$$

The Right panel of Figure 3.11 shows the sagitta as a function of $p_\perp$, for $L = 2$ m at $B = 0.25$ T. Given the relatively small sagitta, high $p_\perp$ (> 2 GeV/c) tracks are essentially contained within a single sector, so the TPC can be regarded from a certain point of view as 24 semi-independent detectors. This is helpful in assessing systematic uncertainties (see Analysis Chapter). The fractional curvature error in the bend plane can be translated into the error on the sagitta (ignoring multiple Coloumb scattering):

$$\frac{\delta k_{\text{res}}}{k} \approx \frac{\delta s}{s} = \frac{8p_\perp}{z\kappa BL^2}\,\delta s \tag{3.12}$$

Also informative for a primary track [7] is its global fit signed DCA to the

---

[7]Recall a primary track is one that ostensibly originates from the interaction point, i.e. primary vertex.
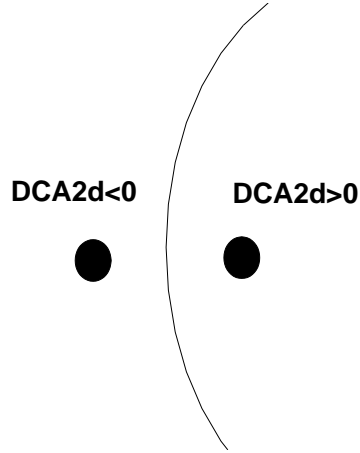
DCA2d<0   **DCA2d>0**

Figure 3.12: Definition of DCA2d.

primary vertex in the bend plane (DCA2d)[8]. The sign is defined such that DCA2d>
0 if the event vertex lies inside the track circle and negative otherwise (Figure 3.12).
Since a track's $p_\perp$ is (to first order) determined by a circle fit in the plane transverse
to the magnetic field, the DCA2d is correlated with the curvature ($p_\perp$) resolution;
i.e. the curvature resolution improves for tracks with smaller DCA2d[9].

3.5   Corrections

Three corrections were applied during reconstruction. (i) A non uniform
magnetic field with components not parallel to the electric field will distort the drift
of the ionized electrons transverse to the electric field. The drift velocity **v** can be
written as: [50]

$$\mathbf{v} = \mu|\mathbf{E}|\frac{1}{1 + \omega^2\tau^2}\left(\hat{\mathbf{E}} + \omega\tau(\hat{\mathbf{E}} \times \hat{\mathbf{B}}) + \mathrm{O}((\omega\tau)^2)\right) \qquad (3.13)$$

---

[8]The DCA2d is 0 for primary fit tracks by construction

[9]The 3 dimensional DCA may also carry a sign based on the track's corresponding DCA2d
(sDCA3d)

43

where ω is the cyclotron frequency and τ is the characteristic time between electron collisions. The distortions were corrected using a mapping of the magnetic field with Hall probes and an NMR probe prior to the TPC's installation[26] . The direction of the electric field was based on the TPC geometry . (*ii*) Hits on padrow 13 were excluded during reconstruction due to possible local $\mathbf{E} \times \mathbf{B}$ distortions in the region between the inner and outer subsectors. Corrections to the field distortions were applied, however, as they affect hit positions on padrows adjacent to padrow 13. (*iii*) The inner and outer subsector were aligned. The outer subsector was translated and rotated relative to the inner sector about a point midway between the subsectors based on hit residuals in $B = 0$ events. Each of the 24 super sectors (inner plus outer subsector) was then aligned to point to the primary vertex via an iterative procedure.

Chapter 4

Analysis

The present analysis measures the invariant yields for unidentified charged hadrons for $1.7 < p_\perp < 6$ GeV/c within an eta window of $|\eta| < 0.5$ for various centrality bins. Criteria for event and track selection, centrality determination, corrections to the yield, and systematic uncertainties will be discussed.

4.1 Event

The *minimum bias* (*minbias*) triggered dataset used in the analysis contained ~ 353k events with a reconstructed primary vertex with $|z| < 200$ cm, while the the *central* dataset consisted of ~ 600k events. Figure 4.1 shows the primary vertex z position for the central and minimum bias datasets. For the minimum bias dataset, the width of the distribution ($\sigma \sim 111$ cm) was determined solely by the beam diamond width, as no additional constraint was applied by the trigger. On the other hand, the plateau region in the central triggered events at $z \sim \pm 75$ cm was due to (Level 3) triggering on the primary vertex position for a subset of events. To ensure that tracks within $|\eta| < 0.5$ were fully contained within the TPC active volume (to guarantee the maximum number of possible hits for each track), the analysis selected minimum bias events with $|z| < 95$ cm and central events with $|z| < 75$ cm (to avoid the dropoff region). After the vertex cut was applied, ~ 230k minbias and ~ 357k central events remained.
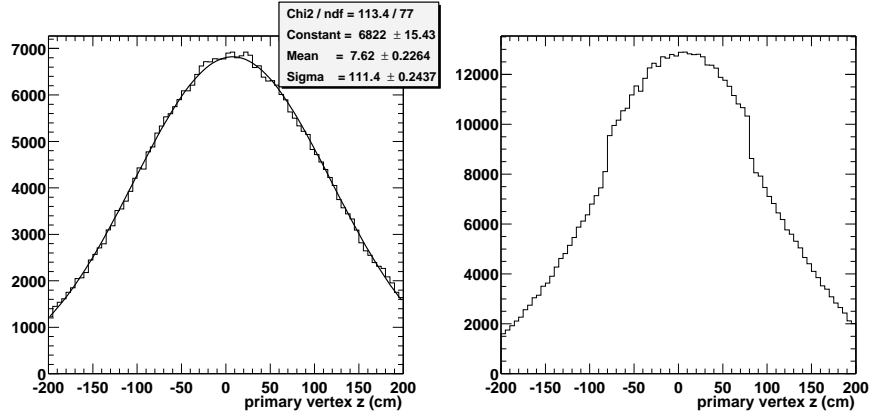
Figure 4.1: Primary vertex z distribution for minimum bias (Left) and central (Right) triggered events.

4.1.1 Centrality Bins

Centrality selection was based on charged multiplicity within $|\eta| < 0.5$ (N_{ch})[1]. To obtain the centrality bins, first the N_{ch} distribution (Figure 4.2) was corrected for vertex finding efficiency as a function of tracks with fit hits$\geq$25 for events within the above z primary vertex position cuts (Left panel of Figure 3.10). Second, the trigger inefficiency was estimated by comparing the low multiplicity (i.e. large impact parameter) end of the efficiency corrected N_{ch} distribution with that from HIJING [104] generated events , normalizing the two distributions between $40 < N_{ch} < 80$. Nuclear collisions at large impact parameter $(12 < b < 20$ fm$)$ were assumed to be well modeled by HIJING, since the cross section for particle production is primarily determined by the collision geometry and p+p cross section, with nuclear medium effects presumably playing a small role. Correcting for vertex finding efficiency, it was estimated that STAR measures $94 \pm 2\%$ of the Au+Au geometric cross section (7.2 barns).

---

[1]Track cuts were DCA3d< 3 cm and fit hits $>= 10$.

46

Figure 4.2: dN$_{\text{event}}$/dN$_{\text{ch}}$ distribution with percentile intervals.
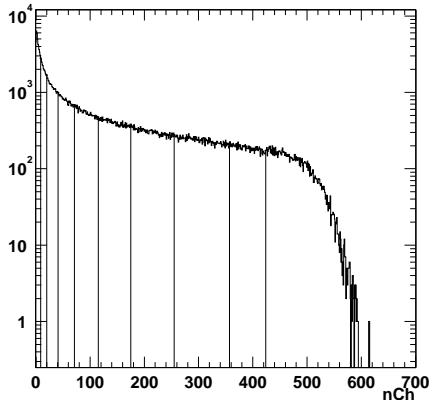
Percent of cross section	N_{ch}
80%	9
70%	20
60%	41
50%	71
40%	115
30%	175
20%	255
10%	357
5%	424

Table 4.1: Centrality bins

The centrality bins and their corresponding N_{ch} boundaries are given in Table 4.1. For each bin, the lower boundary includes the N_{ch} value, while the upper boundary does not. For example, the $70 - 80\%$ centrality bin corresponds to $9 \leq N_{ch} < 20$. The 2% uncertainty on the measured cross section corresponds to an uncertainty of $N_{ch} = 9 \pm 1$ for the 80% boundary. This led to an uncertainty of $\sim {}^{+10}_{-5}$ % for the yield in the 60-80% centrality bin. The yields for the 0-5% and 5-10% centrality bins were analysed using the central triggered dataset, while for the remaining centrality bins the minimum bias dataset was used.

Possible bias in the centrality definition due to multiplicty fluctuations introduced by jets in low multiplicity events was negligible. This was assessed by comparing the percent of the dN$_{\text{event}}$/dN$_{\text{ch}}$ contained above $N_{ch} = 9$ for the quadrant containing a p$_{\perp}$ =2 GeV/c 'trigger' particle against other quadrants; the percentage difference was $< 1\%$. In addition, event selection based on the correlation between ZDC counts and N_{ch} (strictly on ZDC for the 0-5% bin) was investigated, but ultimately not used both to maintain consistency among other STAR analyses and due to the absence of an accurate simulation of the ZDC response. For the

47

0-5% centrality bin, the percentage difference in the spectra between event selection on N_{ch} and on ZDC counts is $\sim 4\%$, roughly independent of $p_\perp$. The percentage difference is smaller for more peripheral centrality bins.

4.2 Tracks

Three multiplicative corrections were applied to the spectra: (*i*) acceptance*efficiency, (*ii*) background, and (*iii*) $p_\perp$ resolution. Acceptance is defined as the percentage of tracks that pass through the TPC active volume, thus affording the opportunity to be reconstructed. Efficiency is the percentage of accepted tracks the detector plus software chain reconstructs. The separation of acceptance and efficiency is provided for conceptual clarity. In practice, the correction to the spectra depends only on the product acceptance*efficiency. Background is due to non-hadrons (e.g. electrons) and secondary hadrons falsely identified as primary tracks. Finite $p_\perp$ resolution when convoluted with a steeply falling hadron distribution leads to an overcount of the yield, especially at higher $p_\perp$. More details are given in the subsections below.

4.2.1 Embedding

The corrections to the yield require an accurate simulation of the TPC response. The simulation framework begins with an event input to GSTAR, a STAR implementation of GEANT [1], which propagates particles according to the STAR geometry, material, and magnetic field, simulating physical processes such as particle decay, multiple scattering, and the ionization energy loss. The electron clusters are then passed through the TPC Response Simulator (TRS), which models TPC processes from electron transport and charge collection, to electronic response and final signal digitization (i.e. pixel data).

Most corrections used data from the *embedding* procedure, where a few
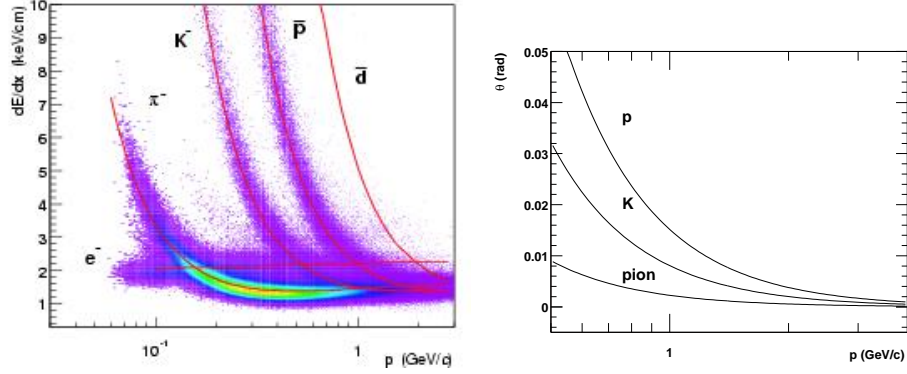
Figure 4.3: Left: dE/dx vs p. (Figure taken from [15]). Right: Multiple scattering angle ($\theta_{\text{plane}}^{\text{RMS}}$) vs p for P10 gas ($X_0 = 110$ m) over a distance of 150 cm. By $p \sim 2$ GeV/c, both dE/dx and $\theta_{\text{plane}}^{\text{RMS}}$ are largely independent of hadron mass.

simulated tracks per event (5% of the primary charged multiplicity) were combined with real raw data. Aspects of the background were investigated using the HIJING event generator and reconstructing the TRS raw data directly. The embedding technique is preferred over a pure simulation as it incorporates the real underlying physical environment of pad signals and noise. The event input for embedding was a uniform distribution of π^- in $p_\perp$ ($0 < p_\perp < 8$ GeV/c) and rapidity ($|y| < 1$). To evaluate correction effects due to a falling $p_\perp$ spectrum, the uniform distribution was simply weighted appropriately. Although the analysis measured all charged hadrons regardless of species, in the (relativistic) $p_\perp$ range of this analysis ($p_\perp > 1.7$ GeV/c), track observables (e.g. fit hits and DCA3d) and correction factors are largely insensitive to species type. For example dE/dx and multiple scattering is virtually transparent to hadron mass in this momentum range (Figure 4.3) [2]. Kaons have a higher probability of decaying in flight, but their shorter lifetime is expected to have a marginal effect on the final spectra (see below).

---

[2] Higher dE/dx means more charge is deposited on the pads, thus affecting hit finding and therefore track reconstruction. Lower multiple scattering also improves track reconstruction.
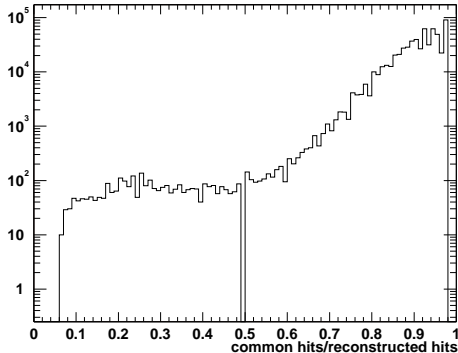
Figure 4.4: Common hits/reconstructed hits for simulated tracks with $2 < p_\perp < 6$ GeV/c.

The embedded data was run through the usual reconstruction chain, (apart from turning off the TPC distortion corrections), and the reconstructed primary vertex of the embedded event was reset to the original vertex position. As an initial step, a reconstructed track was matched with a GSTAR simulated track if they shared 3 or more matched hits (common hits). A reconstructed hit was defined to match a GSTAR simulated hit if they were within 5 mm in x, y, and z. An additional cut of common hits/reconstructed hits>0.3 was applied to define a matched track (Figure 4.4). Less than 1% of the initially matched tracks were removed with this cut. Unless explicitly stated otherwise, 'simulated data' will stand as shorthand for 'reconstructed simulated embedded data'. Appendix B provides plots comparing track observables from real and embedded data.

4.2.2 Cuts

To improve track quality, certain classes of tracks were rejected based on the geometry of their reconstructed trajectory ("track geometry" for short). Only two track observables were found to be significant: the number of hits used in fitting the track (fit hits) and the three dimensional distance of closest approach to the event vertex (DCA3d). A greater number of fit hits improves $p_\perp$ resolution, while a smaller DCA3d selects tracks with better $p_\perp$ resolution and aids in background

50
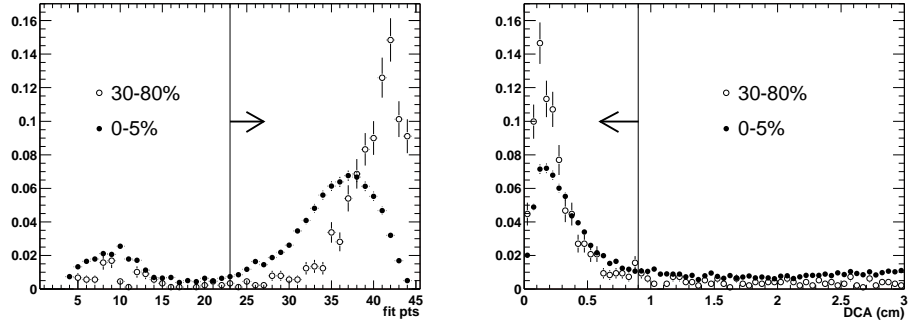
Figure 4.5: Left: Fit points. Right: DCA3d. Tracks are within $4 < p_\perp < 6$ GeV/c and $|\eta| < 0.5$. Vertical lines and arrows indicate the cut and accepted part of the distribution, respectively. The secondary hump at low fit hits is likely from split tracks at padrow 13. Histograms have been normalized by the total number of entries.

rejection. [3] Figure 4.5 shows a typical plot of the fit hits and DCA3d distributions for the 0-5% and 30-80% centrality bin for real data, and their corresponding cuts of fit hits>=23 and DCA3d<0.9. The placement of cuts was a compromise between maximizing the number of fit hits/minimizing the DCA3d, and avoiding the meat of the distributions. Other cuts were investigated such as (i) the angle at which a track crosses a padplane to assess sector boundary effects that may not be properly reproduced in the simulation [4] (i.e. non symmetric pad coverage or local distortions) (ii) dE/dx (i.e. for electron background) and (iii) the distance of closest approach in the plane transverse to the magnetic field (DCA2d). However these and other cuts were found to have marginal effect on the spectra.

---

[3] Actually, DCA2d is correlated with $p_\perp$ resolution, but since DCA2d $<=$ DCA3d cutting on DCA3d or DCA2d has a similar effect on $p_\perp$ resolution. However, in terms of background rejection, cutting on DCA3d is roughly equivalent to cutting on both DCA2d and DCAz.

[4] There was some anamolous behaviour in the yield at large crossing angle (> 10 deg) for tracks with large positive DCA2d, but the DCA3d cut adequately removed these faulty tracks
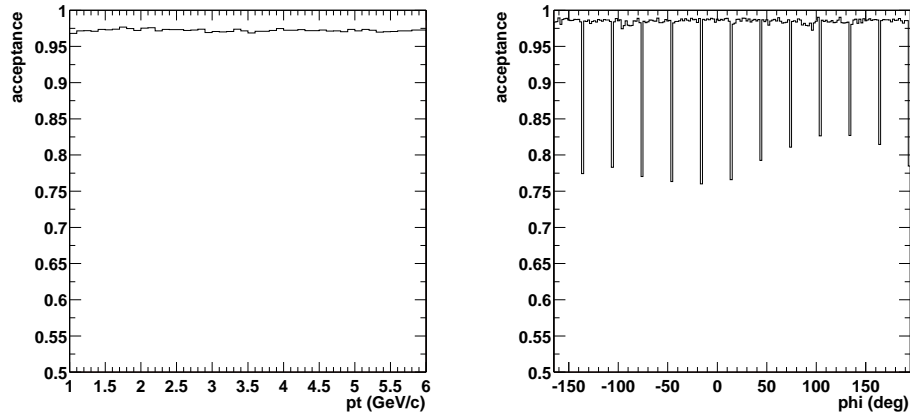
Figure 4.6: Acceptance as a function of $p_\perp$ (Left) and ϕ (Right). The plots are zero suppressed.

4.2.3 Acceptance and Efficiency

Acceptance is the percentage of tracks that traverse the active TPC volume. For example low $p_\perp$ tracks may not be accepted if they spiral before reaching the active TPC region, or high $p_\perp$ tracks may not be accepted if they traverse gaps between sectors. These are examples of geometric acceptance; i.e. acceptance that depends on the physical layout of the detector. Included in the current definition will be tracks that fail to reach the active volume due to decay.

In addition, acceptance depends on track geometry ($p_\perp$, ϕ, η, nhits). However since the z position of the event vertex and η cuts were chosen so that tracks are geometrically accepted in η, and since the final spectra integrate over ϕ, it suffices to consider the acceptance as a function of $p_\perp$ only. Following the working definition that a simulated track has a chance to be reconstructed provided it has at least ten hits, acceptance is defined as the ratio of the number of simulated tracks with $>=10$ hits over the number of input simulated tracks. Because the definition is defined purely in terms of simulated tracks prior to reconstruction, acceptance is

52

independent of the underlying pixel/track density and therefore event centrality.

For high $p_\perp$ tracks, acceptance is uniform vs $p_\perp$ at $\sim 97\%$ as shown in the Left panel of Figure 4.6. The weak $p_\perp$ dependence reflects the similarity in sagitta between a $p_\perp$ =2 GeV/c and a $p_\perp$ =6 GeV/c track. Hits lost to sector gaps account for roughly half the non-accepted tracks, as illustrated in the dips in the Right panel of Figure 4.6, a plot of acceptance as a function of ϕ. Note that due to a kaon's relatively short lifetime ($c\tau = 3.713$ m), the acceptance of kaons was found to be $\sim 92\%$ for tracks above $p_\perp$ =2 GeV/c ([15]). Across centrality bins, the STAR measured kaon dN/dy is $\sim 13 - 15\%$ of the charged hadron yield ([9]). Assuming the fraction of kaons is uniform in $p_\perp$, differing kaon lifetime alters the charged hadron acceptance by 1% and was ignored.

Efficiency is the percentage of accepted tracks found by the detector and reconstruction chain. In practice, a unique definition of efficiency is not possible since it's coupled to the definition of acceptance. However, only the product acceptance*efficiency (acc*eff) contributes to the final correction as, (ignoring other tracking corrections)

$$\text{True} = \frac{\text{Reconstructed}}{\text{acceptance} * \text{efficiency}} \tag{4.1}$$

Formally, the definition of acc*eff is

$$\text{acceptance} * \text{efficiency} = \frac{\#\text{Reconstructed tracks}}{\#\text{Input simulated tracks}} \tag{4.2}$$

Figure 4.7 shows acc*eff vs (simulated) $p_\perp$ and η for the 0-5% and 60-80% centrality bins, integrated over primary vertex $|z| < 75$ cm. The acceptance is independent of both $p_\perp$ and η so any variation in the acc*eff plots is due to inefficiency. The relatively weak $p_\perp$ dependence again points to the similarity of all high $p_\perp$ tracks. Integrated over $|\eta| < 0.5$, at $p_\perp$ =5 GeV/c, the acc*eff is $\sim 67\%$ and $\sim 88\%$ for the 0-5% and 60-80% centrality bins, respectively. For the 0-5%
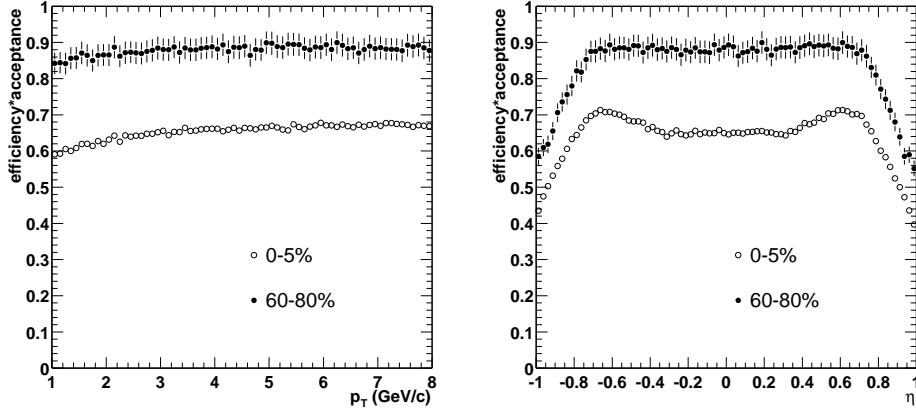
Figure 4.7: Acceptance*efficiency as a function of $p_\perp$ (Left) and η (Right) for two centrality bins. The left plot is integrated over $|\eta| < 0.5$ and the right plot over $2 < p_\perp < 6$ GeV/c. Both plots are for primary vertex $|z| < 75$ cm.

centrality bin the efficiency begins to drop for tracks below $p_\perp \sim 2$ GeV/c, as both the fit hits and DCA3d distribution grow increasingly wider at lower $p_\perp$, which results in the track cuts rejecting a higher percentage of tracks. The increasing efficiency for higher absolute values of η (prior to the dropoff at $\eta \sim \pm 0.7$, which is due to nonacceptance at the edges of the TPC) is probably due to in part to the tracks having more hits due to smaller clusters (shorter drift and less diffusion) and thus less hits lost to hits merging; and the tracks having a longer apparent length across a padrow (more charge deposited). These effects in concert lead to better hit resolution/hit finding efficiency and consequently to tracks with more fit hits and narrower DCA3d (see Systematic Uncertainty for more detail).

To clarify the effect of electron drift distance on efficiency, the Left panel of Figure 4.8, shows acc*eff for tracks with $|\eta| < 0.05$ as a function of the z position of the event vertex for the 0-5% centrality bin. For tracks near the central membrane, the acc*eff is $\sim 63\%$, while for tracks at $|z| = 150$ cm, the acc*eff rises to nearly 80%. Due to the large dependence of efficiency on the vertex z for more central

54
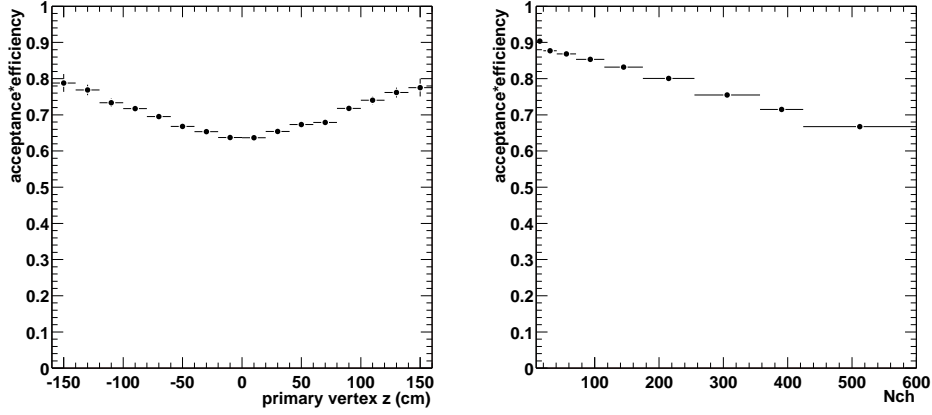
Figure 4.8: Left: Acceptance*efficiency for 'straight-up' tracks as a function of primary vertex z. Tracks are within $3 < p_\perp < 6$ GeV/c and $|\eta| < 0.05$ for the 0-5% centrality bin. Right: Acceptance*efficiency as a function of N_{ch} (primary vertex $|z| < 95$ cm). The N_{ch} bins correspond to the centrality bins listed earlier, starting from 60-80% and ending with 0-5%.

events, applying the efficiency correction per 5 cm z vertex bins was investigated. However, because the embedding data sampled a sufficiently high number of primary vertex z positions, the percentage difference on the final spectra between applying the efficiency correction per primary vertex z bin and integrating over z was found to be less than 1%. For more peripheral events, the efficiency is more uniform as a function of η, $p_\perp$, and primary vertex position z. The centrality dependence of acc*eff on N_{ch} is shown in the right panel of Figure 4.8 for standard cuts.

For the analysis, the acc*eff vs $p_\perp$ and η were separately fit with a exponential and a polynomial, respectively. A two dimensional function of $p_\perp$ and η was constructed assuming independence of the η and $p_\perp$ variables. The correction was then applied on track-wise basis. Plots of acc*eff for all centrality bins can be found in Appendix C.

4.2.4 Momentum Resolution

Due to finite momentum resolution, a track's reconstructed $p_\perp$ may be higher or lower than it's 'true' $p_\perp$. For a given $p_\perp$ bin X, one can consider (i): tracks reconstructed into other $p_\perp$ bins (flow out) and (ii): tracks from other $p_\perp$ bins falsely reconstructed into bin X (flow in). If the yield were independent of momentum and if the distribution in $\Delta p_\perp = p_{\perp\text{meas}} - p_{\perp\text{true}}$ were symmetric, then the number of tracks flowing in and out of bin X would be equal. However, since the yield is rapidly decreasing as a function of $p_\perp$, it's more probable for lower $p_\perp$ tracks to flow into X than vice versa. This leads to an overcount of the yield.

As discussed in the Reconstruction chapter, the fractionional difference in curvature defined as

$$(k_{\text{true}} - k_{\text{measured}})/k_{\text{true}} \tag{4.3}$$

($k \equiv 1/p_\perp$) follows a gaussian distribution, while the distribution in $p_\perp$ is skewed towards larger measured $p_\perp$ (this exacerbates the overcounting in yield for a given $p_\perp$ bin). Therefore, the relevant observable is the fractional curvature resolution as function of $p_\perp$

$$\delta k/k(p_\perp) \equiv \sigma[(k_{\text{measured}} - k_{\text{true}})/k_{\text{true}}] = a + b \cdot p_\perp \tag{4.4}$$

where σ is the standard deviation of a simple gaussian fit. Figure 3.8 shows $\delta k/k$ in central events for global and primary fit tracks as a function of $p_\perp$. The linear fits for $p_\perp > 1.5$ GeV/c give $\delta k/k = 0.012 + 0.016 \cdot p_\perp/\text{GeV/c}$ and $\delta k/k = 0.013 + 0.011 \cdot p_\perp/\text{GeV/c}$ for central and peripheral events, respectively. Primary fit tracks were used for the reported data, but the spectra was also measured for global fit tracks to assess systematic uncertainties.

The multiplicative correction factor due to finite curvature resolution, $\text{Cor}_{\text{res}}(p_\perp)$,
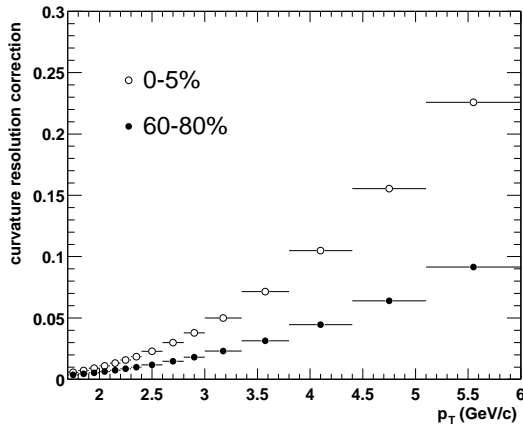
Figure 4.9: (1-$p_\perp$ resolution correction) as a function of $p_\perp$ for 0-5% and 60-80% centrality bins. A cut of |primary vertex z| < 75 and 95 cm was applied, respectively.

for $p_0 < p_\perp < p_1$ can be written as

$$\mathrm{Cor_{res}} = \frac{\int_{p_0}^{p_1} \mathrm{dx}\ f(x)}{\int_0^\infty \mathrm{dx}\ \int_{p_0}^{p_1} \mathrm{dy}\ g(x, y)} \tag{4.5}$$

where the numerator is the yield in the $p_\perp$ bin according to the true distribution $f(x)$, and the denominator is the yield convoluted with the finite curvature resolution. Given the linear fit parameter a and b defined above, then

$$g(x, y) = f(x) \cdot \frac{1}{\sqrt{2\pi} \cdot (ay^2/x + by^2)} \exp\left(-\frac{(x-y)^2}{2(ay + bxy)}\right) . \tag{4.6}$$

Since $f(x)$ is unknown, the correction was found by an iterative procedure, where the corrected data was fit according to $f(x)$ for $2 < p_\perp < 6$ GeV/c using statistical errors, with its parameters used for the next iteration. A power law was assumed for the true distribution $(\mathrm{dN/d}p_\perp = f(x) = \mathrm{Const} \cdot x(1 + x/p_0)^{-n})$. The procedure appeared to 'converge' by the third iteration in the sense that the difference between the second and third iteration was $\ll 1\%$. Other forms of $f(x)$ were investigated and the differences were included in the systematic uncertainties. Figure 4.9 shows $(1 - \mathrm{Cor_{res}})$ for the 0-5% and 60-80% centrality bins.

4.2.5 Background

Background includes non hadrons (e.g. electrons) and secondary hadrons mistakenly reconstructed as primary tracks. The two main sources of background were protons ($\bar{p}$) from Λ ($\overline{\Lambda}$) decays, and $\pi^{\pm}$ from low transverse momentum $\bar{p}$ or $\bar{n}$ annihilation in detector material. The Λs may be primary tracks or daughters from Σ^0 decays. Although Λ decays to π^- and a proton, at high $p_\perp$ over 99% of the background were proton daughters [5]. Also contributing to the background at the 1-2% level were charged $\pi^{\pm}$ from K_S^0 decays. Electrons, mostly from π^0 conversions in detector material, were found to constribute less than $\sim 1\%$ to the yield and were ignored.

Modifications to the charged hadron yield due to $\Sigma^{+/-}$ decays were not applied. The $\Sigma^{+/-}$ daughters are not background but primary hadrons lost in the reconstruction; i.e. anti-background or acceptance loss. From $\Sigma^+ \rightarrow p + \pi^0$ decays (branching ratio of $\sim 50\%$), approximately $\sim 40\%$ of the protons are reconstructed as primary tracks. None of the neutrons from $\Sigma^- \rightarrow n + \pi^-$ decays are reconstructed. Therefore $\sim 90\%$ of $\Sigma^+ + \Sigma^-$ are "lost". If for central collisions at $p_\perp = 2$ GeV/c $(\Lambda + \Sigma^0)/(h^+ + h^-)/2 \sim 0.4$, $\Sigma^0/\Lambda \sim 0.3$, and $\Sigma^0 = \Sigma^{+/-}$, then $\sim 10\%$ of the charged hadron yield may consist of $\Sigma^{+/-}$. Assuming the slope parameters for Λ and $\Sigma^{+/-}$ are identical, the $\Sigma^{+/-}$ constribution to the charged hadron yield is negligible ($\sim 2\%$?) at $p_\perp = 5.5$ GeV/c.

The Left panel of Figure 4.10 shows a plot of the signed DCA3d (sDCA3d)[6] on a log scale from central HIJING generated events; the shaded histogram is the background, and the unshaded histogram the background plus signal. The bias in the background towards sDCA3d< 0 is likely due to the primary fit 'straightening'

---

[5]Due to kinematics, the heavier proton carries the majority of the Λ 's momentum at high momentum.

[6]Not to be confused with DCA2d. This is the 3d DCA with the sign determined by the DCA2d. The relatively wide bins mask the dip at sDCA3d~ 0.
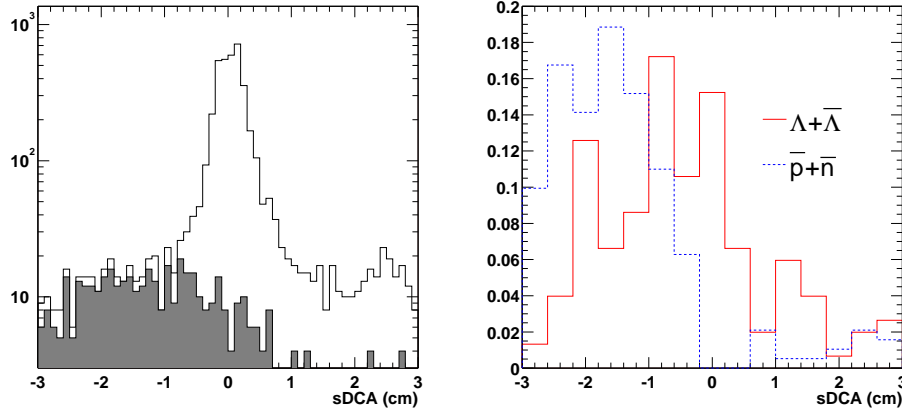
Figure 4.10: Left: sDCA3d for all (unshaded) and background (shaded) for $4 < p_\perp < 6 GeV/c$ tracks in HIJING simulated events. Right: sDCA3d for background arising from $\bar{n}$, $\bar{p}$ annihilation (dashed) and Λ, $\bar{\Lambda}$ decays. As shown, the sDCA3d distribution is skewed towards sDCA3d< 0.

the track and thus increasing the track's apparent $p_\perp$ when the event vertex lies outside the track circle. Tracks with |sDCA3d| >0.9 cm were rejected by a track cut [7]. To estimate the background within the accepted DCA3d region, an attempt was first made to quantitatively compare the shape of the background DCA3d distribution in simulations with the shape in real data. By appropriate scaling of the the sDCA3d in the background dominated region (< -1 cm), the signal in the real data can extracted. The advantage of this method is that it is independent of the $p_\perp$ distribution of the parent hadrons as long as the shape of the sDCA3d distribution of daughters due to Λ decay and $\overline{p}$ /$\overline{n}$ annihilation are identical. Unfortunately this is not the case as shown in the Right panel of Figure 4.10. The reasons are twofold. First, the secondary vertex of a Λ decay, whose decay length is $c\tau = 7.89$ cm, is closer to the nominal event vertex than the secondary vertex of a $\overline{p}$ /$\overline{n}$ annihilation, which occurs mostly in the Berillium beam pipe of radius 4 cm. Second, the

---

[7]The tracks at large positive sDCA3d are poorly reconstructed low $p_\perp$ particles.
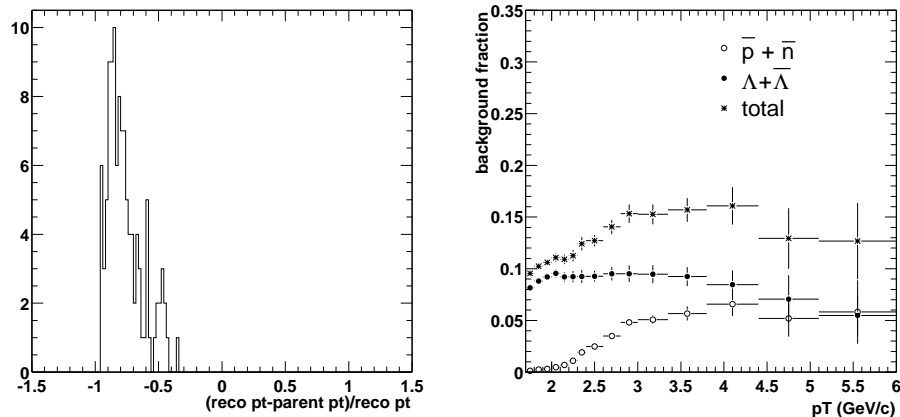
Figure 4.11: Left: (reco p$_\perp$ -$\bar{p}$ pt)/reco p$_\perp$ for $\bar{p}$ annihilations according to central HIJING collisions. Right: Fraction of background as a function of p$_\perp$ for the 0-5% centrality bin. Pions from K_S^0 s are included in the total but not shown. Error bars are statistical.

protons from a Λ decay lie within a narrower cone around the parent's momentum vector than a $\pi^\pm$ in an inelastic $\bar{p} + p$ interaction.

Therefore, the level of background was estimated by weighting the Λ and $\bar{p}$ simulated distributions with the extrapolated STAR measured spectra. The STAR Λ ($\overline{\Lambda}$) yield in m_T was fit with an exponential to cover the range above $m_T \sim 2.5$ GeV/c [40]. The STAR measured $\overline{p}$ yield [39] was extended above $p_\perp \approx 1$ GeV/c using a thermal model, which agrees with the PHENIX measured $\overline{p}$ spectrum at pt=2 GeV/c [30]. The $\overline{n}$ yield was assumed to be identical with the $\overline{p}$ yield. The fraction of background for Λ daughters were required to be no less than 2% at high p$_\perp$, based on HIJING simulations. Furthermore, the $\overline{p}$ yield was required only to $p_\perp \sim 2-3$ GeV/c as the parent $\bar{p}$'s transverse momentum is approximately 30% of its daughter's reconstructed $p_\perp$ (Left panel of Figure 4.11). The weighted background yield was subtracted from the real data's uncorrected yield per $p_\perp$ bin. The ratio of the background over raw yield, as a function $p_\perp$ for the 0-5% centrality bin is shown

in the Right panel of Figure 4.11. The background fraction at $p_\perp$ =2 and 5.5 GeV/c is $\sim 10\%$ and $\sim 12\%$, respectively. Appendix C shows the background fraction as a function of $p_\perp$ for all centrality bins.

4.3 Systematic Uncertainty

Sources of systematic uncertainty are track corrections (acceptance*efficiency, background, momentum resolution), the centrality definition, and TPC spatial inhomegenties causing tracking distortions. Due to the small sagitta, high $p_\perp$ tracks are especially sensitive to spatial distortions and require special care. Systematic uncertainties from the various track corrections are correlated and difficult to disentangle from each other. Uncertainties due to distortions and track corrections are likewise not easily discriminated. A best estimate was derived from various observables.

4.3.1 Due to Efficiency and Distortions

Since track corrections, aside from effects due to dead pad electronics, are symmetric around $z = 0$, variation between the two symmetric drift regions, the east $(z < 0)$ and west $(z > 0)$ TPC, is likely due to spatial nonuniformities. The Right panel of Figure 4.12 is the ratio of the acc*eff corrected yield [8] for tracks in the East TPC over West TPC for the 0-5% centrality bin. The yield for primary and global fit tracks are shown in the upper and lower halves of each plot, respectively. For primary fit tracks, the East/West ratio for positive or negative tracks separately shows a nontrivial $p_\perp$ dependent yield, peaking at $\sim 1.4 - 1.6$ for positive tracks. On the other hand, for the sum of the charged tracks (positive + negative), the ratio is approximately unity as a function of $p_\perp$ (Right panel). In light

---

[8] The effect of ncluding the $p_\perp$ resolution correction is minimal ($\sim 1\%$ at $p_\perp$ =5.5 GeV/c), and the background should roughly cancel.
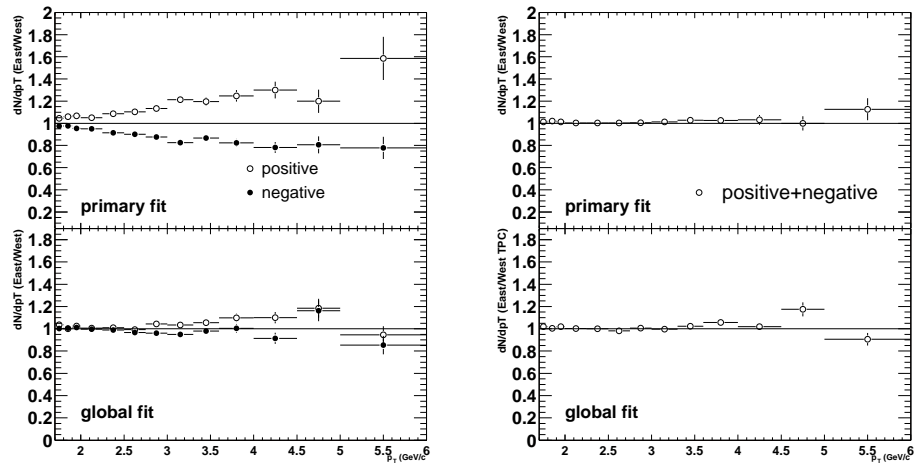
Figure 4.12: The ratio in yield for East/West TPC for postive and negative tracks (Left) and the sum of charged tracks (Right). The primary and global fit tracks are shown in the upper and lower plots, respectively.

of the significantly smaller systamatic variation in the ratio for positive + negative tracks, the final spectra reports $(h^+ + h^-)/2$, and all subsequent plots will show the sum of charged tracks unless specified otherwise. Of course, the ratio at near unity does not necessarily imply that spatial distortions do not alter the $p_\perp$ resolution for each half equally; but this will be investigated when considering the the systematic uncertainties of the $p_\perp$ resolution correction (see below).

4.3.2 Due to Efficiency and Distortions

The fact that the East/West ratio is near unity for global fit track seems to indicate the problem lies especially with spatial inhomogeneties affecting the primary fit (lower Left panel of Figure 4.12). As shown previously, the global fit DCA2d is correlated with the $p_\perp$ resolution and serves as a useful diagnostic tool. Figure 4.13 shows the mean of a gaussian fit of the DCA2d as a function of the z primary vertex for tracks with $2 < p_\perp < 3$ GeV/c and $|\eta| < 0.1$. The left and center panels are
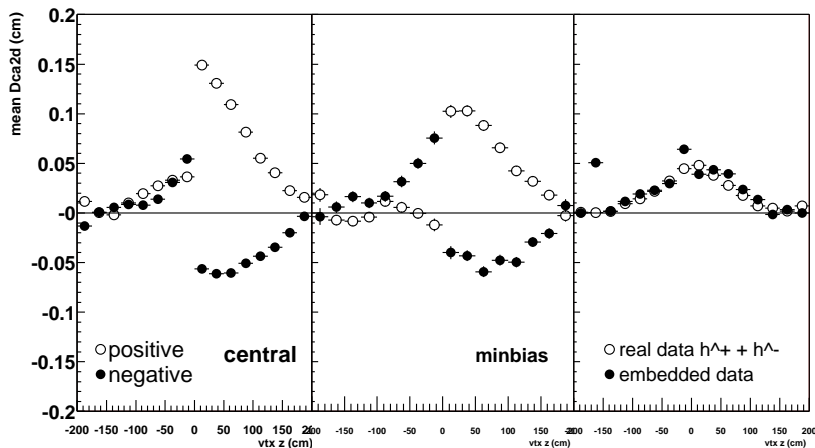
Figure 4.13: Mean DCA2d as a function of primary vertex z for the central triggered dataset (Left) and minimum biased dataset (Center). The Right panel shows the mean DCA2d for $(h^+ + h^-)$ in real central triggered data and π^- in embedded data.

for the central and minimum biased triggered datasets, respectively. Recall that the sign of the DCA2d is defined as positive if the track circle contains the primary vertex in the xy plane and negative otherwise, independent of the track's charge sign. Therefore the 'splitting' of the mean for the two charged signs about 0, especially for the West TPC, is consistent with the picture that the space charges are shifted so that the track is 'rotated' in the same direction regardless of its charge sign. The differing behavior of the mean across $z = 0$ is also compatible with the East versus West asymmetry in the yield. The hypothesis is if the primary vertex position lies outside the track circle, including the primary vertex as a fit point anamolously 'straightens' the track circle, increasing the measured $p_\perp$ (and vice versa). Finally, the Right panel shows the mean DCA2d for all charged tracks in real central collisions and for π^- in $p_\perp$ weighted embedded data; reasonably good agreement is observed. The increasingly positive mean as z approaches 0 is most likely due from the skewing the DCA2d distribution from low $p_\perp$ tracks poorly reconstructed at high
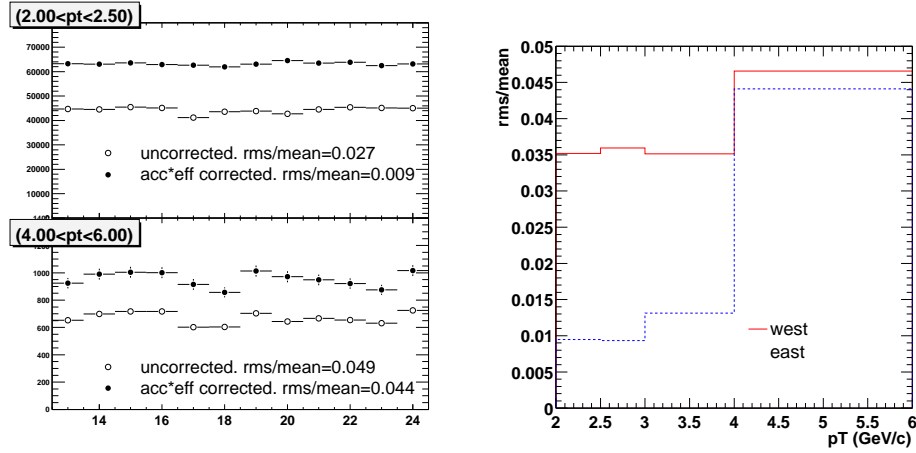
Figure 4.14: Left: Yield per sector for East TPC for 2 $p_\perp$ bins. Right: Relative systematic variation in sector-wise yield as a function of $p_\perp$ for East and West TPC.

$p_\perp$.

Based on the cylindrical geometry of the TPC, it is natural to investigate the systematic uncertainty in the ϕ and z (drift) coordinates. Since each TPC half is divided into 12 sectors and since virtually all high $p_\perp$ tracks are contained within a single sector (sagitta$\sim$ 6 mm for $p_\perp$=6 GeV/c. See Figure 3.11), systematic uncertainty in ϕ may be assessed through the sector-wise variation in the yield. The Left panel of Figure 4.14 shows the summed charged yield per sector for East TPC for two $p_\perp$ bins. The yield was corrected for acc*eff per sector to account for dead pads. Assuming that the observed sector-wise uncertainty is the quadrature sum of the systematic and statistical uncertainties, the relative systematic variation of the sector-wise yield was $3-5\%$ at high $p_\perp$ (Right panel of Figure 4.14). For tracks with $2 < p_\perp < 3$ GeV/c contained in the East TPC, correcting for efficiency reduced the systematic variation from $\sim 2.5\%$ to $\sim 1\%$; little change was observed for tracks in the West TPC.

Tracks with $2 < p_\perp < 4$ GeV/c afford sufficient statistics to investigate

64
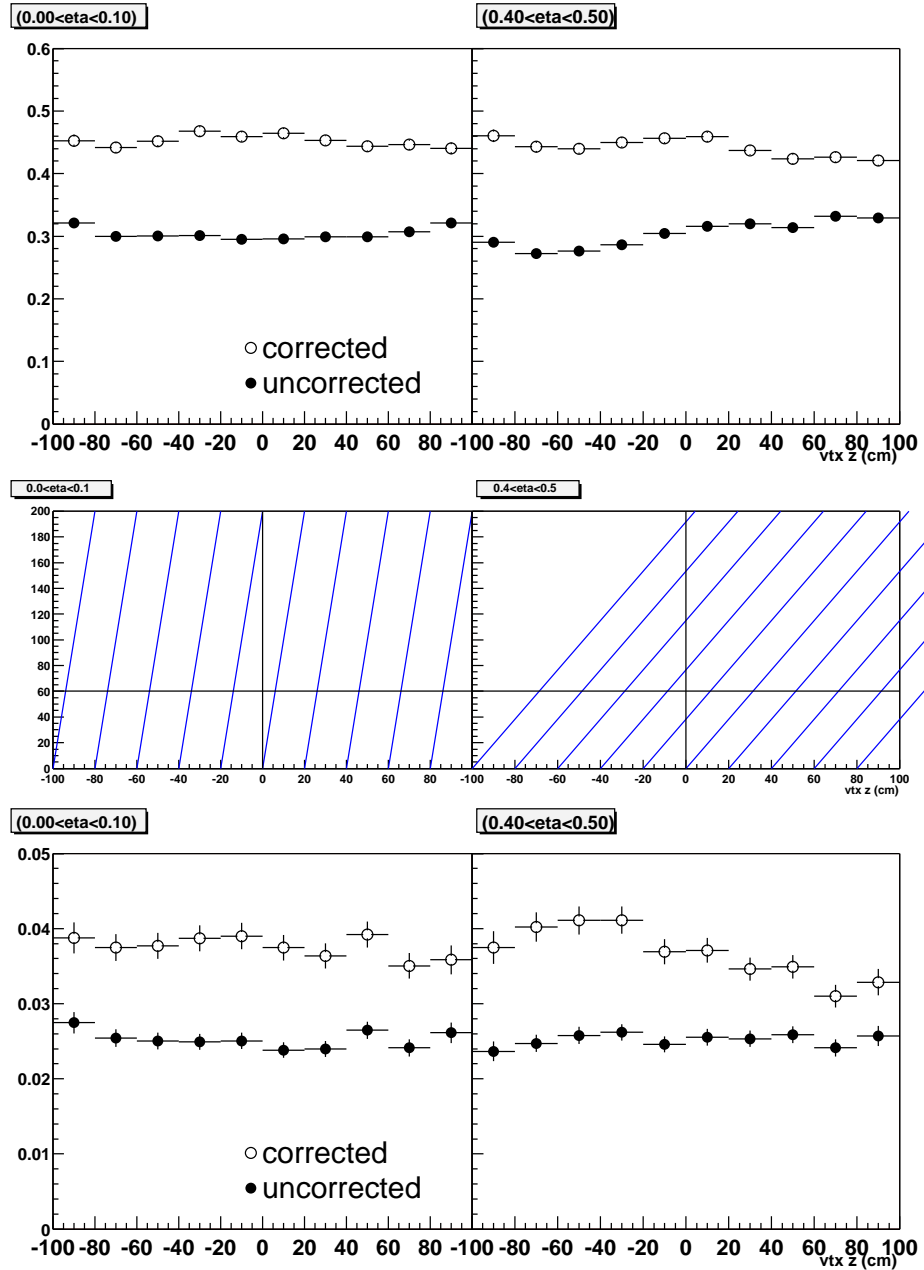
Figure 4.15: Yield as a function of primary vertex z for $2 < p_\perp < 3$ (Upper) and $3 < p_\perp < 4$ (Lower) tracks. The Left panel is for $0 < \eta < 0.1$ and the right $0.4 < \eta < 0.5$. The middle panels show the regions of the TPC contained in each η slice (only the lower limit is show per z vertex bin).

tracking uncertainties as a function of drift length in detail. The top panels of Figure 4.15 show the yield per event for tracks within $2 < p_\perp < 3$ GeV/c as a function of z vertex for two eta slices: $0 < \eta < 0.1$ (left) and $0.4 < \eta < 0.5$ (right). The bottom panels show the corresponding plots for tracks with $3 < p_\perp < 4$ GeV/c. Both uncorrected and acc*eff corrected yields are plotted. The middle panels show the regions of the TPC contained in each η slice. The yield per event should be independent of which z region in the TPC the tracks traverse. For tracks with $2 < p_\perp < 3$ GeV/c, little or no z dependence is observed after applying the efficiency correction. However, for tracks with $3 < p_\perp < 4$ GeV/c at large η (bottom Right panel), the yield seems relatively higher for tracks closer to the central membrane than near the end caps [9]. The peak to peak percentage difference is $\sim 15\%$. The variation is only marginally reduced by the $p_\perp$ resolution correction. A larger percentage of background may account for the difference but this was not verified due to insufficient statistics. For tracks with $3 < p_\perp < 4$ GeV/c, the relative variation for the corrected yield is estimated to be $< 1\%$ for $0 < \eta < 0.1$ and $\sim 8\%$ for $0.4 < \eta < 0.5$. Similar behavior is seen for the converse η slices, i.e. $-0.5 < \eta < -0.4$, although the variation in yield is slightly smaller.

In light of anamolous behavior near the central membrane, the yield was measured excluding tracks crossing the central membrane. The Left panel of Figure 4.16 shows the eff*acc corrected yield for tracks not crossing the central membrane over all tracks as a function of $p_\perp$ for 2 centrality bins. There seems to be a systematic decrease with $p_\perp$ ($\sim 8\%$ at $p_\perp = 5.5$ GeV/c), but due to uncertainty of the normalization when excluding the central membrane crossing tracks, the final spectra included all tracks. Finally, the systematic variation on the final spectra with different track cuts was assessed. The Right panel of Figure 4.16 shows the ratios of the corrected spectra using 'wide cuts' (DCA<1.5, fit hits>=15) and 'tight' cuts

---

[9]This effect may be due in part to tracks crossing the central membrane.
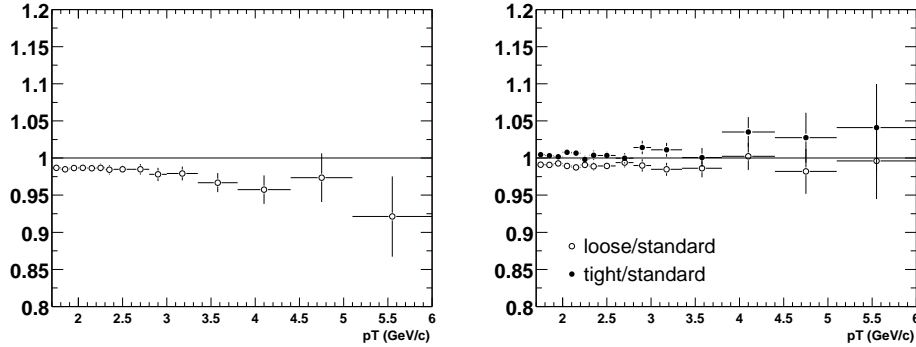
Figure 4.16: Left: Yield for tracks not crossing the central membrane over all tracks. Right: Yield for tighter and looser track cuts over the standard cut. Both plots are for the 0-5% centrality bin.

(DCA3d<0.7, fit hits>= 26) over the 'standard cuts' (DCA3d<0.9,fit hits>=23) for various centrality bins [10]. Good agreement is observed, with the tight/standard cut ratio varying less than $\sim$ 5% at $p_\perp$ =5.5 GeV/c. Varying cuts for less central events typically show smaller percentage differences in the yield [11].

Gathering the information from the above plot, the relative systematic uncertainty due to acceptance*efficiency and distortions (collectively called *tracking* systematic uncertainty) was estimated to be:

$$\Delta_{\text{tracking}} = \sqrt{\Delta^2_{\text{efficiency}} + \Delta^2_{\text{cut}} + \Delta^2_{\text{phi}} + \Delta^2_z + \Delta^2_{\text{distortion}}} \tag{4.7}$$

This is not a rigorous formula; its purpose is motivate a reasonable number. The uncertainty in z and ϕ is based on $p_\perp \sim 2$ GeV/c tracks, where distortion effects are expected to be small. $\Delta_{\text{distortion}}$ can be considered an extra kludge factor,

---

[10]For the $p_\perp$ (or k) resolution corrections, the embedding data was weighted directly instead of using the functional form discussed above. This was done to take into account non gaussian tails in the Δk distributions, especially important for the looser DCA3d cut.

[11]Additional studies on systematic variation were using global fit tracks, integrating over a narror primary vertex z (i.e. $z < 30$ cm), and using the minimum bias dataset for the 0-5% centrality bin. Relative differerences in the yield were less than $\sim$ 10% at $p_\perp$ =5.5 GeV/c and essentially zero for $p_\perp < 3$ GeV/c

estimating the uncertainty due to distortions above and beyond the contribution contained implicitly in the other uncertainty factors. The $p_\perp$ dependent terms are Δ_{cut}, Δ_{phi} and $\Delta_{\text{distortion}}$. $\Delta_{\text{efficiency}}$ is an estimate of the relative uncertainty on the overall normalization due to the efficiency correction.

For example, for the 0-30% centrality bins, the total relative systematic uncertainty on the yield due to the efficiency and distortions at $p_\perp = 2$ GeV/c is estimated to be

$$\Delta_{\text{tracking}} \sim \sqrt{0.04^2 + 0.02^2 + 0.03^2 + 0.03^2 + 0.03^2} \sim 0.07 \rightarrow 0.10 \qquad (4.8)$$

For $p_\perp = 5.5$ GeV/c the estimate is

$$\Delta_{\text{tracking}} \sim \sqrt{0.04^2 + 0.05^2 + 0.05^2 + 0.03^2 + 0.15^2} \sim 0.18 \rightarrow 0.20 \qquad (4.9)$$

The numbers following the arrows indicate the final relative uncertainties, conservatively rounded up. The systematic uncertainty for the more peripheral (30-80%) centrality was estimated to be slightly lower: 7% for $1.7 < p_\perp < 3$ GeV/c increasing to 15% at $p_\perp = 5.5$ GeV/c

4.3.3 Due to Momentum Resolution Correction

The accuracy of the $p_\perp$ resolution correction depends on the accuracy of the $p_\perp$ resolution computed from the embedding data. A rough estimate of the accuracy of the $p_\perp$ resolution may be determined by weighting the simulated data's DCA2d distribution so that its width agrees with that from the real data's, and then assessing its effect on the curvature resolution. The Left panel of Figure 4.17 shows the sigma of a gaussian fit for $2 < p_\perp < 3$ Gev/c tracks within $|\eta| < 0.1$ as a function of primary vertex z. Both real and embedded simulated data are shown for the 0-5% centrality bin, with the percentage difference between the two on the order of $\sim 20\%$ roughly independent of vertex z. The simulated flat $p_\perp$ distribution was weighted
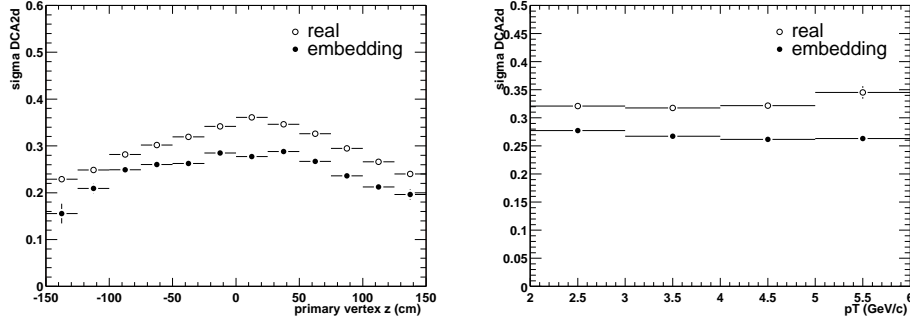
Figure 4.17: Left: sigma DCA2d for real and embedded data as a function of primary vertex z for $2 < p_\perp < 3$ GeV/c tracks within $|\eta| < 0.1$. Right: sigma DCA2d as a function of $p_\perp$, when integrated over $|z| < 75$ cm and $|\eta| < 0.5$.

by a power law; (otherwise, the tails at large DCA2d>0 are not reproduced)[12]. When integrated over $|z| < 75$ cm and $|\eta| < 0.5$, the percentage difference of the DCA2d widths between real and embedded data remains approximately 15-25% for $p_\perp = 2 - 6$ GeV/c (Right panel of Figure 4.17)[13] If the simulated data's DCA2d distribution is weighted to agree with the real data (sigma increased by 20% across $p_\perp$ bins) then $\delta k/k$ increases by a relative $\sim 10\%$ at $p_\perp = 5.5$ GeV/c (Left panel of Figure 4.18). Assuming $\delta k/k$ is uniformly larger by 10%, the corresponding absolute change in the $p_\perp$ resolution correction at $p_\perp = 5.5$ GeV/c is ~ 0.04 (Right panel). As with most track observables, the agreement in the DCA2d widths improves for lower multiplicity events making the above a worst case scenerio.

Other sources of systematic uncertainties for the $p_\perp$ resolution correction are:

- Assumption of a power law

---

[12]Fit range was ± 0.7 cm.

[13]The background may account for some of the difference. Again, there was insufficient statistics to verify.
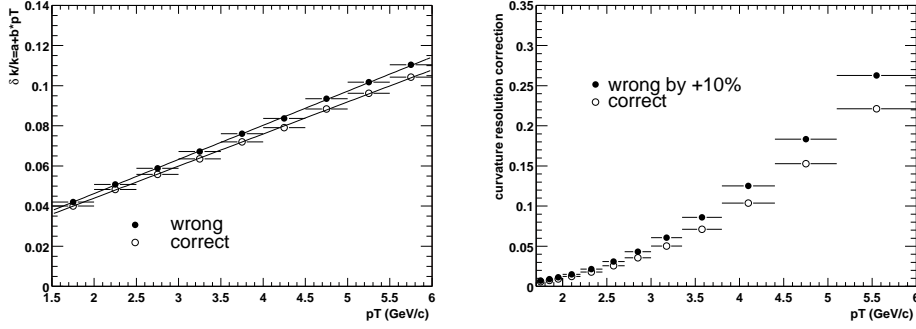
Figure 4.18: Left: The curvature resolution as a fuction of $p_\perp$ for the 0-5% centrality bin if the DCA2d sigma is 20% greater. Right: 1-Cor$_{res}$ when applying the wrong resolution by 10% adjustment.

Both $f(x) = \mathrm{Const} * p_\perp (1 + p_\perp/p_0)^{-n}$ (power law) and $h(x) = \mathrm{Const} * p_\perp (1 + (p_\perp/p_0)^2)^{-n}$ were investigated as the functional form used in the correction scheme. For more central events, $h(x)$ yielded a better fit to data, but the power law was chosen for consistency across centrality bins. For the $p_\perp$=5.5 GeV/c bin in 0-5% central events, using the power law led to $(1 - \mathrm{Cor}_{res}) = \sim$ 0.23 while $h(x)$ gave $(1 - \mathrm{Cor}_{res}) \sim 0.20$. In addition, merely changing the fit range or the errors on the data points modified the correction factor by a several percentage points.

- Functional versus direct embedding correction.

  The $p_\perp$ resolution correction factor was also found by simply weighting the embedding data's $p_\perp$ distribution and taking the ratio (1-(simulated yield/reconstructed yield)) per $p_\perp$ bin [14]. Presumably due to the non-guassian tails in the $k_{MC} - k_{RC}$ distributions, the corrections obtained from the embedding data were ~ 0.02 percentage points higher than that derived from the functional procedure at $p_\perp$ =5.5 GeV/c for the 0-5\$ centrality bin.

---

[14]Note that this method bypasses the calculation of $\delta k/k$ vs $p_\perp$.

- Additional uncertainty due to the primary vertex position resolution

  As mentioned in the Reconstruction Chapter, the primary fit contrains the track to originate from the primary vertex. However, the $p_\perp$ resolution was determined from the embedding data, where the simulated tracks originate precisely from the primary vertex. For the 60-80% centrality bin where the primary vertex resolution is ~ 1 mm, this may not insignificantly affect $\delta k/k$. A preliminary investigation based on HIJING generated events indicated that the $p_\perp$ resolution could be 15% higher for the 60-80% centrality bin. This was the largest source for uncertainty in the correction factor for peripheral events.

  For the 0-5% bin at $p_\perp$=5.5 GeV/c, the above factors conspired to a conservative uncertainty on the $p_\perp$ resolution correction of ± 0.10 (absolute), or $\sim 12\%$ on the yield. For each $p_\perp$ bin the uncertainty on the correction was approximated as 40% of $(1 - \text{Cor}_{\text{res}}$. For example, for the 0-5% centrality bin at $p_\perp$=5.5 GeV/c, $(1 - \text{Cor}_{\text{res}}) \sim 0.23 \pm 0.09$, thus contributing $\sim 11\%$ uncertainty on the yield.

4.3.4 Due to Background

The uncertainty on the background was conservatively estimated to be 100% of the estimated background for $1.7 < p_\perp < 2$ increasing to 100% of the background above $p_\perp$=3 GeV/c. Motivating the conservative estimate at higher p$_\perp$ was that the background for $p_\perp > 2.5$ GeV/c was based on the extrapolated Λ and $\bar{p}$ yields, and not directly on measured data points. At lower p$_\perp$ the conservative estimate factored in the uncertainty of the loss of primary $\Sigma^{+/-}$ through weak decays (anti-background). For example, the multiplicative background correction factor for the $p_\perp$=5.5 GeV/c bin is 0.88 ± 0.12, corresponding to a systematic uncertainty of $0.12/0.88 \rightarrow 13.6\%$ on the yield.

4.3.5 Total Systematic Uncertainty

The total systematic uncertainty is the quadrature sum of the uncertainties due to tracking, background, momentum resolution, and centrality determination. Although some correlation exists among the various uncertainties, it was estimated to be small. The uncertainty in the centrality determination was 5% for all bins except for the 60-80% bin which was estimated to be 10%. See Appendix E for data and their corresponding uncertainties.

Chapter 5

Results

5.1 Overview

The inclusive charged hadron yields $(h^+ + h^-)/2$ have been measured for $1.7 < p_\perp < 6$ GeV/c about midrapidity, $|\eta| < 0.5$, as a function of centrality in Au+Au collisions at $\sqrt{s_{\mathrm{NN}}}$=130 GeV at RHIC. To observe possible hadron suppression due to radiative partonic energy loss, the yields were compared to two reference data where jet quenching is not expected to occur: NN and peripheral Au+Au collisions. The results have been published [41].

5.2 Inclusive Charged Hadrons Distributions

A single particle *inclusive* process is defined as

$$A + B \rightarrow C + X \tag{5.1}$$

where A and B are the interacting particles (e.g. Au nuclei), C the measured hadrons, and X all other final state particles. The hadron C may be identified (e.g protons) or unidentifed as in the present case $((h^+ + h^-)/2)$.

The corresponding differential invariant yield for hadron C is

$$\frac{1}{\sigma_{A+B}} E \frac{\mathrm{d}^3\sigma_{\mathrm{C}}}{d\mathbf{p}^3} = E\frac{\mathrm{d}^3\mathrm{N_C}}{\mathrm{d}\mathbf{p}^3} \tag{5.2}$$

$$= \frac{1}{p_\perp}\frac{\mathrm{d}^2\mathrm{N_C}}{\mathrm{d}\phi\mathrm{dydp}_\perp} \tag{5.3}$$

$$= \frac{1}{2\pi p_\perp}\frac{\mathrm{d}^2\mathrm{N_C}}{\mathrm{dydp}_\perp} \tag{5.4}$$
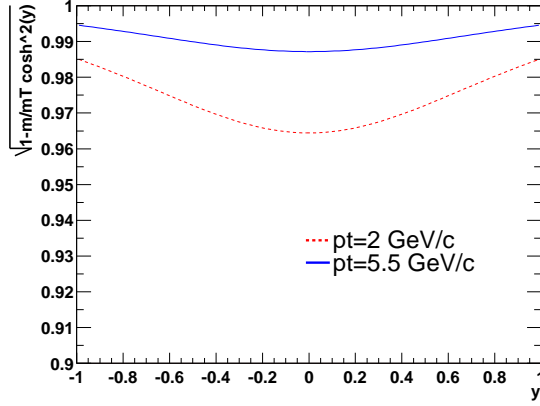
Figure 5.1: Jacobian transforming dN/dy to dN/dη. Pion mass was assumed

where in the second equality the identity dy/dp_z=1/E is used, and in the third equality the invariant yield is integrated over ϕ.

Since the masses of the measured hadrons are unknown, the invariant yield is measured within a pseudorapidity (η), rather than a rapidity (y) window. The two invariant yields are related by

$$\frac{d^2N}{d\eta dp_\perp} = \sqrt{1 - \left(\frac{m}{m_T \cosh^2 y}\right)} \frac{d^2N}{dy dp_\perp} \ . \tag{5.5}$$

Figure 5.1 shows the y dependence of the Jacobian assuming pion mass, at $p_\perp = 2$ GeV/c and $p_\perp = 5.5$ GeV/c. The factor is essentially unity for $p_\perp$ =5.5 GeV/c.

Experimentally, the differential yield is approximated with finite bins. For the present analysis, the $(h^+ + h^-)/2$ yield was measured within the pseudorapidity window $|\eta| < 0.5$ ($\Delta\eta = 1$).

$$\frac{1}{2\pi}\frac{1}{p_\perp}\frac{d^2N_{(h^++h^-)/2}}{d\eta dp_\perp}|_{\eta=0} \approx \frac{1}{2\pi}\left\langle\frac{1}{p_\perp}\right\rangle\frac{\Delta N_{(h^++h^-)/2}}{\Delta\eta\Delta p_\perp}|_{|\eta|<0.5} \tag{5.6}$$

The $p_\perp$ bin widths ($\Delta p_\perp$) were chosen to grow approximately with the momentum resolution. The growing $p_\perp$ bins has the corollary benefit of maintaining

74

reasonable statistical errors for $p_\perp > 3$ GeV/c. There is nothing inherently special with the chosen $p_\perp$ binning. Other bin widths were investigated, but the chosen binning seemed to lessen the statistical fluctuations for $p_\perp > 3$ GeV/c. (See Appendix E for the $p_\perp$ binning.)

The factor $\langle 1/p_\perp \rangle$ was measured using uncorrected data. For each $p_\perp$ bin,

$$\left\langle \frac{1}{p_\perp} \right\rangle = \frac{\sum_i^N 1/p_{\perp i}}{N} \tag{5.7}$$

Although finite $p_\perp$ resolution convoluted with a steeply falling $p_\perp$ distribution may change the charged hadron yield by $\sim 24\%$ at $p_\perp = 5.5$ GeV/c, $\langle 1/p_\perp \rangle$ for a smeared and unsmeared distributions differed only by $\sim 1\%$ at $p_\perp = 5.5$ GeV/c. This was true both for numerical calculations with a power law distribution, and for real data when comparing the measured $\langle 1/p_\perp \rangle$ with the calculated $\langle 1/p_\perp \rangle$ from a power law fit. The yield was not corrected for the difference.

The data points, $p'_\perp$, were chosen within each $p_\perp$ bin according to [48]

$$f(p'_\perp) = \frac{1}{\Delta p_\perp} \int_{p_\perp^{\min}}^{p_\perp^{\max}} dx\, f(x), \tag{5.8}$$

where $\Delta p_\perp = p_\perp^{\max} - p_\perp^{\min}$ and $f(x) = \mathrm{Const}(1 + p_\perp/p_0)^{-n}$ is a power law fit to data. Solving for $p'_\perp$ gives

$$p'_\perp = p_0 \left[\frac{p_0}{\Delta p_\perp (1-n)} \left(\left(1 + \frac{p_\perp^{\max}}{p_0}\right)^{-(n-1)} - \left(1 + \frac{p_\perp^{\min}}{p_0}\right)^{-(n-1)} \right)^{-1/n} - 1 \right] \tag{5.9}$$

One iteration was performed for the final position of $p'_\perp$.

Figure 5.2 shows the invariant charged hadron yield $(h^+ + h^-)/2$ for $|\eta| < 0.5$ for various centrality bins [1]. Data for $p_\perp > 1.7$ GeV/c are listed in Appendix E. Data for $p_\perp < 1.7$ GeV/c are tabulated elsewhere (REF).

---

[1] The yield for $p_\perp < 1.7$ GeV/c is provided by Frank Laue for the STAR collaboration.
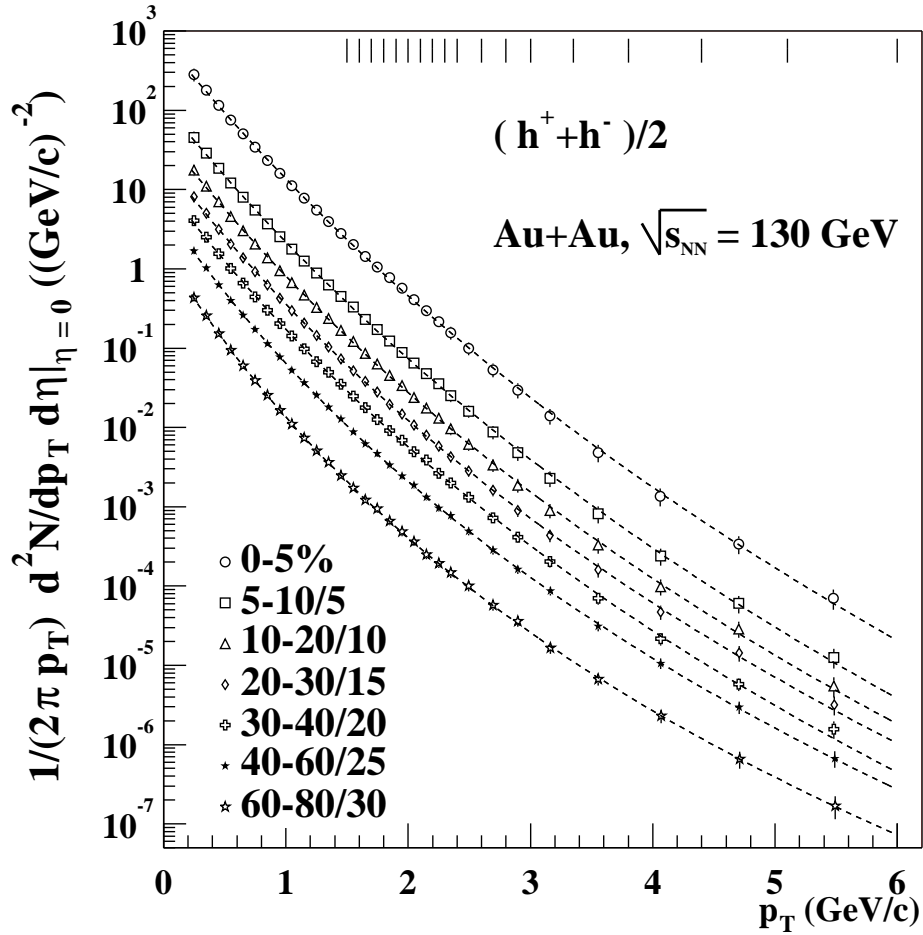
Figure 5.2: Invariant charged hadron yield $(h^+ h^-)/2$ for $|\eta| < 0.5$ as a function of $p_\perp$ for various centrality bins. Yields are scaled for the sake of uncluttered presentation. Dashed lines are power law fits to data.

centrality	$\langle N_{\text{bin}} \rangle$	$\langle N_{\text{part}} \rangle$
0-5%	965^{+67}_{-67}	350^{+4}_{-4}
5-10%	764^{+59}_{-63}	296^{+7}_{-7}
10-20%	551^{+48}_{-56}	232^{+9}_{-9}
20-30%	348^{+44}_{-45}	165^{+10}_{-10}
30-40%	210^{+36}_{-36}	115^{+10}_{-12}
40-60%	90^{+22}_{-22}	62^{+9}_{-11}
60-80%	20^{+7}_{-9}	20^{+5}_{-6}

Table 5.1: $\langle N_{\text{bin}} \rangle$ and $\langle N_{\text{part}} \rangle$ for various centrality bins according to the Monte Carlo Glauber model. Values calculated by [84].

5.3 $\langle N_{\text{bin}} \rangle$ and $\langle N_{\text{part}} \rangle$

The hadronic cross section in heavy ion collisions is expected to scale with the mean number of participants ($\langle N_{\text{part}} \rangle$) for soft processes and the mean number of binary collisions ($\langle N_{\text{bin}} \rangle$) for hard processes. Therefore, hadron suppression at high $p_\perp$ may be observed by comparing the Au+Au yield per independent binary nucleon+nucleon (NN) collision with the yield of a reference system where jet quenching is not expected to occur. Two possible references are NN collisions or Au+Au collisions at large impact parameter. For an NN reference, hadron suppression is quantifiable via the nuclear modification factor:

$$R_{\text{AA}}(p_\perp) = \frac{\text{d}N_{\text{AA}}/\text{dydp}_\perp}{(\langle N_{\text{bin}} \rangle / \sigma_{\text{NN}}^{\text{inel}}) \text{d}\sigma_{\text{NN}}^{\text{inel}}/\text{dydp}_\perp} \quad (5.10)$$

Absent nuclear medium effects, $R_{\text{AA}} = 1$ at high $p_\perp$. Jet quenching brings R_{AA} below unity. Initial multiple scattering (Cronin) and radial flow increases R_{AA}, while nuclear shadowing decreases R_{AA}[2].

To determine $\langle N_{\text{bin}} \rangle$ and $\langle N_{\text{part}} \rangle$, $\text{d}\sigma/\text{dN}_{\text{bin}}$ and $\text{d}\sigma/\text{dN}_{\text{part}}$ were calculated using a Monte Carlo Glauber model with $\sigma_{\text{NN}} = 41 \pm 1$ mb. The number density of

---

[2]See Motivation Chapter.

nucleons follow the Woods-Saxon distribution

$$\rho(r) = \rho_0 \frac{1}{1 + \exp{(r - R)/a}} \, , \tag{5.11}$$

with radius $R = 6.5 \pm 0.1$ fm and surface diffuseness $a = 0.535 \pm 0.027$ fm. The parameters values were based on e+Au scattering data, and the radius was increased from $R = 6.38$ fm to $R = 6.5$ fm to account for the neutron skin [23]. The calculated $d\sigma/dN_{bin}$ ($d\sigma/dN_{part}$) distribution was divided into percentile intervals, and $\langle N_{bin} \rangle$ ($\langle N_{part} \rangle$) was determined for each bin. The uncertainty on $\langle N_{bin} \rangle$ and $\langle N_{part} \rangle$ were estimated by varying the Woods-Saxon parameters and σ_{NN} according to their respective uncertainties, and by altering the the measured Au+Au cross section by $\sim 5\%$. For the most peripheral bin, $\langle N_{bin} \rangle$ and $\langle N_{part} \rangle$ were especially sensitive to the the measured Au+Au cross section, resulting in an uncertainty of $\sim 30\%$ [84]. Table 5.1 lists $\langle N_{bin} \rangle$ and $\langle N_{part} \rangle$ with their uncertainties for each centrality bin.

5.4 R_{AA}

When calculating R_{AA}, the most desirable reference is NN collisions at $\sqrt{s} = 130$ GeV/c. Since this is not available, the NN reference was an interpolation to $\sqrt{s} = 130$ GeV of a power law fit to UA1 $\bar{p}+p$ data at $\sqrt{s} = 200..900$ GeV/c [24, 100] [3]. Writing the power law function as

$$\frac{1}{2\pi p_\perp} \frac{dN}{dp_\perp} = C \left(1 + p_\perp/p_0\right)^{-n} \, , \tag{5.12}$$

the reference parameters are $C\sigma_{inel}^{NN} = 267^{+4}_{-6}$ mb/(GeV/c)^2, $p_0 = 1.90^{+0.17}_{-0.09}$ GeV/c, and $n = 12.98^{+0.92}_{-0.47}$. The NN reference was crosschecked with a pQCD extrapolation to 130 GeV of the UA1 200 GeV spectrum. At $p_\perp = 6$ GeV/c the agreement was within 5% [55, 99].

---

[3] Also see Appendix D
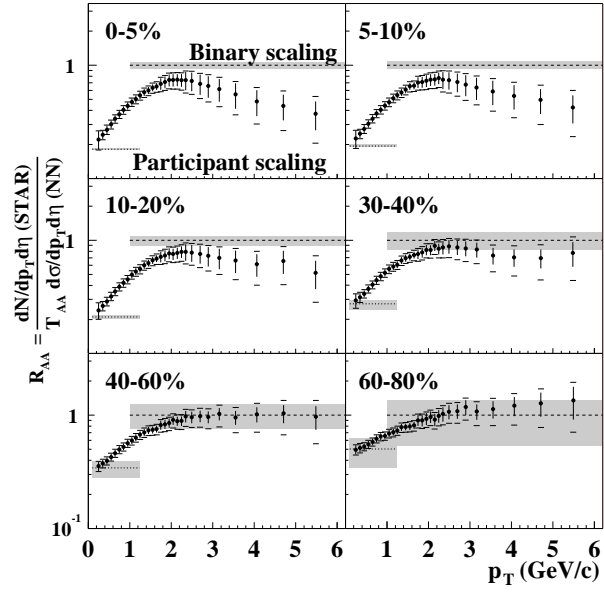
Figure 5.3: R_{AA} for various centrality bins. The dashed lines at unity and below represent $\langle N_{bin} \rangle$ and $\langle N_{part} \rangle$ scaling, respectively. The uncertainty in the scaling is represented by the shaded regions. Uncertainties between bins are highly correlated.

In addition the NN reference was corrected for the UA1 acceptance of $|\eta| <$ 2.5 (as opposed to $|\eta| < 0.5$ for the present analysis) using two independent pQCD calculations [46, 99], which yielded a multiplicative correction factor of 1.17 ± 0.06 at $p_\perp = 2$ GeV/c and 1.35 ± 0.10 at $p_\perp = 5.5$ GeV/c. Isopin corrections (i.e. $p + \bar{p}$ vs. $p + p$ collisions) are negligible for $p_\perp < 6$ GeV/c [55]. The systematic uncertainty of the NN reference is the quadrature sum of the power law parameter and acceptance correction uncertainties.

Figure 5.3 shows R_{AA} for various centrality bins. The dashed lines at unity represent $\langle N_{bin} \rangle$ scaling, while the dashed lines below unity indicate $\langle N_{part} \rangle$ scaling [4]. The shaded regions show the systematic uncertainties of the scaling. The error bars are the total uncertainties of the data, and the caps are the quadrature sum with the systematic uncertainty of the NN reference. R_{AA} increases for $p_\perp < 2$ GeV/c as the yield moves from participant to binary scaling for all centrality bins. For $p_\perp > 2$, R_{AA} saturates near unity for peripheral bins, while R_{AA} decreases with $p_\perp$ for the central bins. For the 0-5% central collisions, R_{AA} is 0.37 ± 0.16 at $p_\perp = 5.5$ GeV/c with an additional uncertainty of ± 0.03 due to $\langle N_{bin} \rangle$. The dependence of R_{AA} with $\langle N_{part} \rangle$ for several $p_\perp$ bins is shown in Figure 5.4, clearly exhibiting a decreasing R_{AA} at high $p_\perp$ for more central collisions. Unambiguous hadron suppression in central collisions is observed. Data for R_{AA} are tabulated in Appendix G and for its $\langle N_{part} \rangle$ dependence in Appendix H.

5.5 Central Over Peripheral

Hadron suppression may also be assessed by comparing the charged hadron yield per binary NN collision for Au+Au collisions at small impact parameter against those at large impact parameter. Figure 5.5 shows the ratio of the yield for the 0-5%

---

[4]Note that $\langle N_{part} \rangle$ scaling is technically $\langle N_{part} \rangle / 2$ scaling.
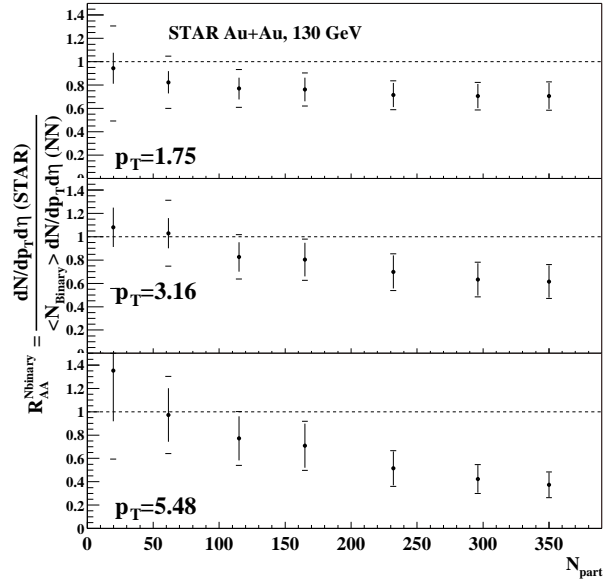
Figure 5.4: R_{AA} vs $\langle N_{part} \rangle$ for three $p_\perp$ bins.
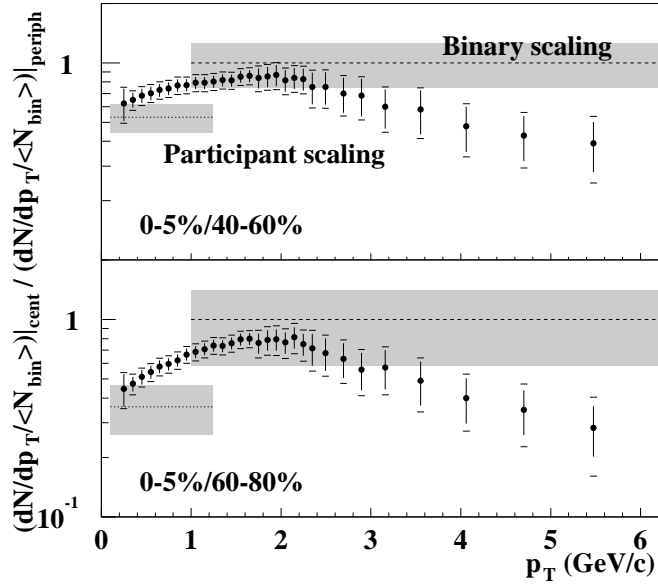
Figure 5.5: Ratio of the $\langle N_{bin} \rangle$ scaled yields for the 0-5% centrality bin over two peripheral bins (40-60% and 60-80%).
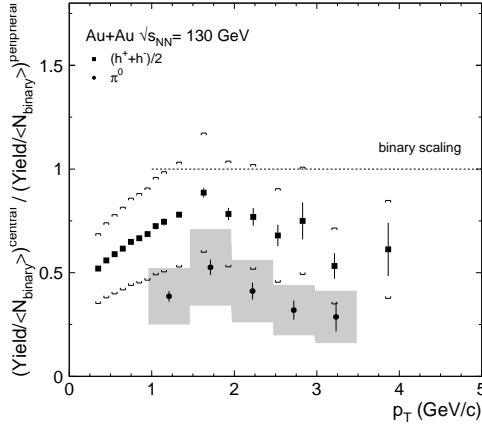
Figure 5.6: Ratio of yield scaled by $\langle N_{bin} \rangle$ in (0-10%) central vs. (60-80%) peripheral collisions for $(h^+ + h^-)/2$ and π^0, measured by the PHENIX Collaboration [29].

centrality bin over the 40-60% and 60-80% peripheral bins, scaled by $\langle N_{bin} \rangle$. The error bars are the uncertainty of the central data, while the caps are the quadrature sum of both datasets. Similarly to R_{AA}, the ratio rises to ~ 2 GeV/c and subsequently begins to fall at higher $p_\perp$. With respect to the 60-80% bin, the ratio at $p_\perp =5.5$ GeV/c is 0.28 ± 0.12 with an additional uncertainty of ± 0.12 due to $\langle N_{bin} \rangle$. Values for both ratios are tabulated in Appendix F.

The PHENIX Collaboration has also reported hadron suppression for Au+Au collisions at $\sqrt{s_{NN}}$=130 GeV [29]. Figure 5.6 shows the ratio of yield scaled by $\langle N_{bin} \rangle$ in (0-10%) central vs (60-80%) peripheral collisions for $(h^+ + h^-)/2$ and π^0. The difference between the $(h^+ + h^-)/2$ and π^0 ratio may be due to a larger than expected contribution from baryons to the total charged hadron yield at high $p_\perp$. Typically, pions are assumed to be the dominant species at high $p_\perp$ since both gluon and quark fragmentation functions favor the production of light mesons. For example, the DELPHI Collaboration has measured pions to account for $\sim 85\%$ of

the charged hadrons in jets in $e^+ + e^-$ collisions [33][5]. However, in central Au+Au collisions pQCD may not entirely determine particle production for the 'intermediate 'high $p_\perp$ range $(2 < p_\perp < 6)$. Rather, baryons from non pQCD processes, (e.g. hydrodynamic transverse flow or baryon junctions [18, 47]), may compete with the pQCD quenched mesons. For instance, the PHENIX Collaboration claims that $\bar{p}/\pi^- \sim 1$ at $p_\perp \sim 2$ GeV/c [30]. The 'anomalously' large baryon content may extend to $p_\perp \sim 6$ GeV/c before reverting back to pQCD rates [56].

5.6 Supplemental Evidence for Jet Quenching

If the produced dense nuclear medium has a sufficiently large volume and long lifetime, local kinetic/chemical equilibrium may be achieved through multiple scatterings. Upon freezeout, the (low $p_\perp$) particles then emerge with a common thermodynamic velocity based on the local temperature and chemical potential. This collective behavior is known as *transverse flow* [59] [6]. For nuclear collisions with a non-zero impact parameter, the produced (low $p_\perp$) particles are found to be correlated with the plane defined by the impact parameter (*reaction plane*). The correlation is typically interpreted as being due to the differential pressure gradient in the spatially anisotropic overlapping region, which leads to an asymmetric transverse flow (i.e. $\langle v_x \rangle \neq \langle v_y \rangle$) and an asymmetric azimuthal distribution of the final state hadrons (Figure 5.7).

The azimuthal asymmetry is quantified via a Fourier decomposition of the particle azimuth distribution with respect to the reaction plane, $\phi - R$:

$$\frac{\mathrm{dN}}{\mathrm{d}(\phi - \mathrm{R})} \propto \left(1 + 2v_1 \cos \phi + 2v_2 \cos 2(\phi - R) + ...\right). \tag{5.13}$$

The first Fourier moment (v_1) describes *directed flow* [7], while the second

---

[5]Although it does not necessarily follow that this extends to the leading hadrons in a jet.

[6]Also referred as *radial flow*.

[7]$v_1 \sim 0$ at midrapidity by symmetry.
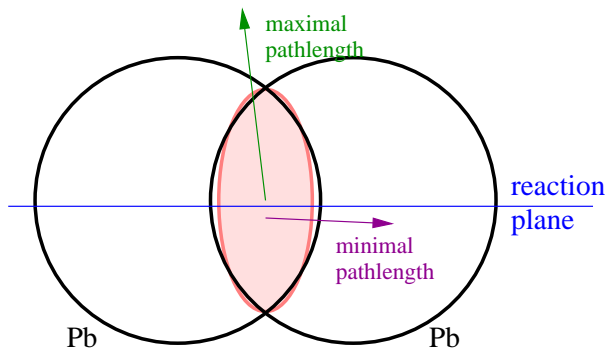
Figure 5.7: The reaction plane in a non central A+A collision.

moment (v_2) refers to *elliptic flow*. Higher order moments have been found to add marginal additional physical insight. Of particular interest for the jet quenching model is the differential elliptic flow, $v_2(p_\perp)$. Assuming thermalization, the hydrodynamic model predicts a near linear rise in v_2 as a function of $p_\perp$. However, at a sufficiently high $p_\perp$, the hydrodynamic model should no longer apply, for the dominant particle production is rather from hard or semi-hard processes. As a parton's energy loss is a function of the azimuthally dependent pathlength in $b \neq 0$ collisions (Figure 5.7), it has been proposed that high $p_\perp$ particles are correlated with the reaction plane and generate a finite v_2 [80]. Note that since the momentum transfer Δp due to (elastic) multiple scattering at high $p_\perp$ is relatively small ($\Delta p/p << 1$), absent energy loss, high $p_\perp$ particles should not be correlated with the reaction plane.

The Left panel of Figure 5.8 shows $v_2(p_\perp)$ for unidentified hadrons in minimum bias events [42]. Displayed are the STAR data, the hydrodynamical model, and the jet quenching model with 3 different assumptions of inital gluon density dN_g/dy. Note that the energy loss prediction of v_2 is reliable only for the highest $p_\perp$ values (> 5 GeV/c) as the intermediate $p_\perp$ region is merely an interpolation between the low $p_\perp$ hydrodynamic and high $p_\perp$ pQCD limits. The monotonic rise in

84
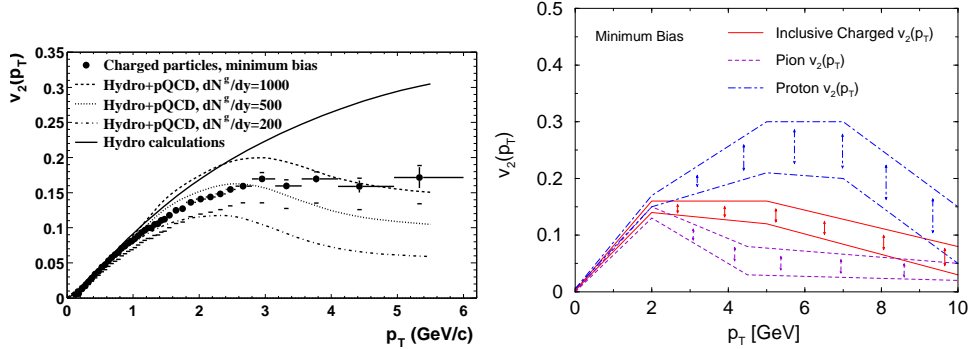
Figure 5.8: Left: v_2 as a function of $p_\perp$ in minimum bias collisions. The hydrodymical and the jet quenching model with 3 different initial gluon density is shown. (Figure taken from [42]). Right: Theoretical picture of $v_2(p_\perp)$ for pions, protons and inclusive charged particles in minimum bias collisions. Error bands are qualitative theoretical uncertainties. (Figure taken from [82])

v_2 up to ~ 1.5 GeV/c is consistent with the hydrodynamical picture which possibly indicates a dense thermalized medium. However, beginning at higher $p_\perp$ ($2-3$ GeV/c), v_2 seems to saturate at a value of ~ 0.17, inconsistent with hydrodynamics. Perhaps of significance is that the onset of saturation in $v_2(p_\perp)$ and the downward turning in R_{AA} lie a similar $p_\perp$ range of $2 < p_\perp < 3$ GeV/c. Criticism of the energy loss model has been levied that the value of observed v_2 at high $p_\perp$ may require a gluon density and jet cross section inconsistent with the observed hadron suppression [95]. Counter arguments have been proposed that $v_2(p_\perp)$ is hadron species dependent with baryons having a greater v_2 than mesons in the intermediate high $p_\perp$ region ($2 < p_\perp < 6$ GeV/c) due to differing particle production mechanisms (e.g. baryon junction vs pQCD) [82]. The apparent uniform $p_\perp$ dependence of v_2 for $p_\perp > 2$ GeV/c is then simply the superposition of baryon and meson constributions to $v_2(p_\perp)$ (Right panel of Figure 5.8)

The discussion of partonic energy loss assumes that at high $p_\perp$ hard scattering dominates with partons fragmenting into jets upon leaving the medium. Has

85
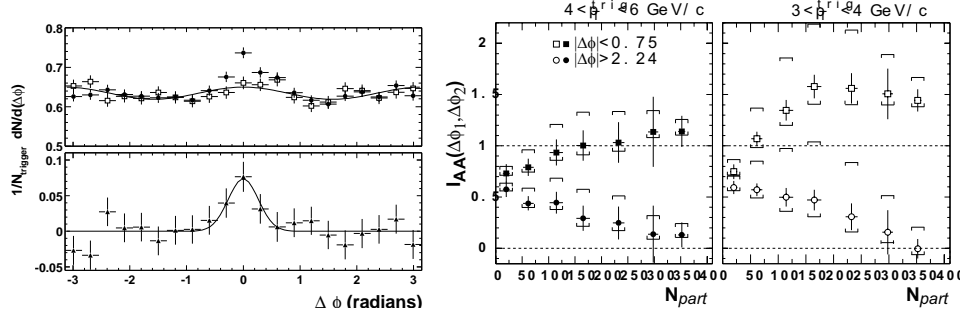
Figure 5.9: Left Upper: Correlation functions for $|\Delta\eta| < 0.5$ (filled circles) and $0.5 < |\Delta\eta| < 1.4$ (open squares) ($\sqrt{s_{NN}}$=130 GeV). Left Lower: Difference of the two correlation functions. A gaussian fit to data yields $\sigma = 0.27 \pm 0.09(\text{stat.}) \pm 0.04(\text{sys.})$ at $\Delta\phi = 0$. (Figure taken from [42]). Center and Right: Ratio of Au+Au and p+p small angle (square) and back-to-back (circle) azimuthal regions vs $\langle N_{part} \rangle$ ($\sqrt{s_{NN}}$=200 GeV). For the Au+Au correlation, the estimated contribution from v_2 according to the reaction plane analysis was subtracted. Caps indicate the dominant systematic uncertainty due to v_2. (Figure taken from [43])

STAR seen any evidence of jets? Since the large background of low $p_\perp$ particles makes jet reconstruction on an event-by-event basis prohibitive, observation of jets was done via a statistical method [42]. Since the hadrons within a jet 'cone' are angularly correlated, two particle azimuth correlations were performed with respect to a trigger particle. The trigger particles were required to fall within $4 < p_\perp < 6$ GeV/c and $|\eta| < 0.7$, while the correlated particles were within $2 < p_\perp < 6$ and $|\eta| < 0.7$. The relative azimuthal distribution was normalized by the number of trigger particles, $N_{trigger}$,

$$\frac{1}{N_{trigger}} \frac{dN}{d(\Delta\phi)} \equiv \frac{1}{N_{trigger}} \frac{1}{\epsilon} \int d\Delta\eta \, N(\Delta\phi, \Delta\eta), \qquad (5.14)$$

where $N(\Delta\phi, \Delta\eta)$ is the number of observed pairs and ϵ is the track finding efficiency.

Figure 5.9 shows the two particle correlation functions for $|\Delta\eta| < 0.5$ and $0.5 < |\Delta\eta| < 1.4$ in central events. The short range correlation function ($|\Delta\eta| < 0.5$) was absolutely normalized, while the long range correlation function ($|\Delta\eta| > 0.5$)

was scaled to match the short range function within the presumably 'off-jet' region $0.75 < |\Delta\phi| < 2.25$ rad. The v_2 derived from fitting the long range correlation function to $\mathrm{dN/d}\Delta\phi \propto 1 + 2\mathrm{v}_2^2\cos(2\Delta\phi)$ is consistent with the v_2 derived from the reaction plane (elliptic flow) analysis [85].

The lower left plot shows the correlation function for $|\Delta\eta| > 0.5$ subtracted from the function for $|\Delta\eta| < 0.5$. For the enhancement about $\Delta\phi = 0$, a gaussian fit yields $\sigma = 0.27 \pm 0.09(\mathrm{stat.}) \pm 0.04(\mathrm{sys.})$, which is consistent with observations from p+p data [22, 28] and with an equivalent analysis performed on HIJING generated data ($\sigma = 0.20 \pm 0.01$), where the dominant production mechanism in this $p_\perp$ range is from hard scattering jet fragmentation; i.e. the finite correlation about $\Delta\phi = 0$ rad is consistent with jet behavior.

Curiously, the enhancement in the correlation function at $\Delta\phi \pm \pi$, which ostensibly identifies back-to-back jets observed in p+p data, appears to be suppressed in central collisions. Finite correlation about $\Delta\phi \pm \pi$ is in fact observed by STAR in Au+Au collision for more peripheral events, agrees well with the measured p+p data, but appears to decrease in magnitude with increasing centrality (Center and Right panel of Figure 5.9). One possible explanation, in harmony with the energy loss model, is that for more central collisions the requirement of the trigger particle biases the observation of high $p_\perp$ particles from hard scattering near the surface of the medium; i.e., the parton fragmenting into the observed trigger particle and its correlated partners 'escape' the medium with minimal inelastic scattering, while the opposite parton loses energy through gluon radiation traversing through the bulk of the medium. In short, STAR does see evidence of jets, but in central collisions the away side jet is suppressed in accordance with the energy loss model [78].

5.7 Saturation Model: An Alternative Explanation

An alternative model to explain the data is the *parton saturation* model [3, 68, 73], possibly forming a new state of matter called the Color Glass Condensate [71]. The saturation model claims that at high energy, the parton phase space density becomes so high it limits the growth of parton occupation at low x [8]. The onset of saturation is characterized by the *saturation scale*, Q_s, which is related to the density of partons in the tranverse plane and grows with energy and the atomic number, A [9]. Even when $\alpha_s(Q_s) \ll 1$, many body coherence effects between low $x$partons produce non linear effects that are outside of the scope of pQCD. The saturation model describes well the Q^2 evoluton of $F_2(x, Q)$ for $x < 0.01$ measured by HERA in a e+p DIS experiment [64]. Although initial state saturation need not be mutually exclusive with the energy loss model, if the totality of the data better agrees with saturation then this necessarily excludes significant energy loss.

Although the saturation scale at RHIC energies is believed to be $Q_s \sim 1 - 2$ GeV, recent studies have indicated that saturation effects on the hadron yield may extend as high as $p_\perp \sim 5 - 10$ GeV/c, and can describe the observed hadron suppression [20]. In particular the invariant yield is predicted to scale as $dN/dyd^dp_\perp \propto N_{\mathrm{part}}/p_\perp^2$ at intermediate high $\mathrm{p}_\perp$. At sufficiently high $\mathrm{p}_\perp$, the yield should revert back to pQCD rates. Figure 5.10 show the hadron yield according to the saturation model for various $\mathrm{p}_\perp$ bins, scaled by the number of participant pairs and normalized to the yield per $\langle \mathrm{N}_{\mathrm{part}} \rangle$ in peripheral collisions. This should be compared with Figure 5.11, which shows analogous plots for the measured STAR yields at $\sqrt{s_{\mathrm{NN}}}$=130 GeV (reference is the 60-80% centrality bin). Although the saturation model may be consistent with data at higher $\mathrm{p}_\perp$ bins, (near) $\langle \mathrm{N}_{\mathrm{part}} \rangle$ scaling appears to be violated at

---

[8]Low $x > 10^{-2}$ gluons are believed to play a significant role at midrapidity at RHIC (and LHC) energies. Gluons dominate over quarks at small $x < 10^{-1}$. Therefore saturation is also refered to as *gluon* saturation.

[9]$Q_s^2 = \alpha_s N_c \frac{1}{\pi R^2} \frac{\mathrm{dN_g}}{\mathrm{dy}}$, where $\mathrm{dN_g}/\mathrm{dy}$ is the gluon distribution and R the hadron radius [71].
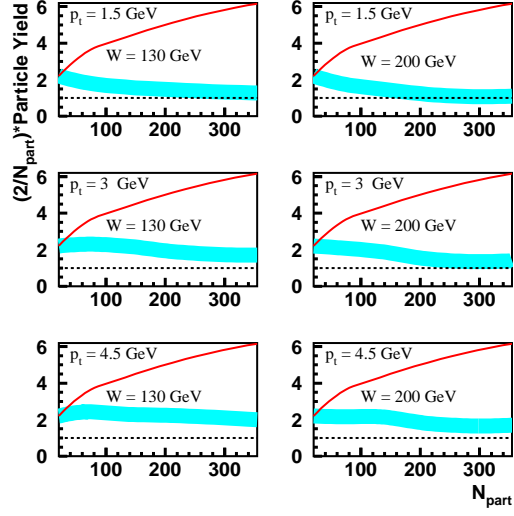
Figure 5.10: The (blue) shaded regions indicate yield scaled by $\langle N_{\text{part}} \rangle / 2$ as a function of $\langle N_{\text{part}} \rangle$, normalized to the $\langle N_{\text{part}} \rangle$ scaled yield in peripheral collisions, for various $p_{\perp}$ bins, according to the saturation model. (Figure taken from [20])
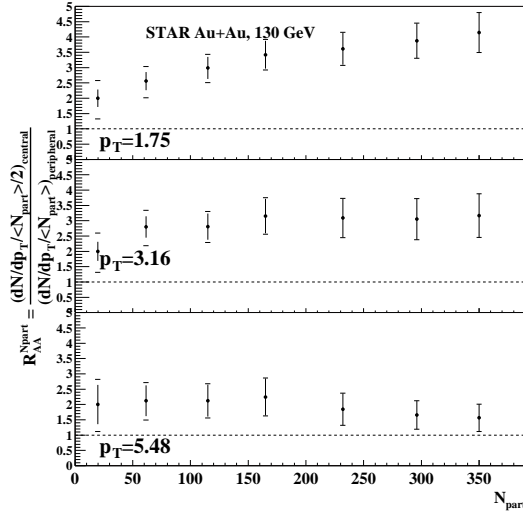
Figure 5.11: Measured yield scaled by $\langle N_{\text{part}} \rangle / 2$ as a function of $\langle N_{\text{part}} \rangle$, normalized to the $\langle N_{\text{part}} \rangle$ scaled yield in 60-80% peripheral collisions. Data is tabulated in Appendix I.

lower $p_\perp$ ($p_\perp$ =1.5 GeV/c) in more central events. In addition, it has been proposed that the observed $v_2(p_\perp)$ at RHIC is not due to spatial/momentum anisotropy but rather to an interplay of saturation and mini jets, possibly explaining the observed saturation at high $p_\perp$ [107].

5.8 Conclusion

Hadron suppression has been observed in central collisions with respect to both $\langle N_{\mathrm{bin}} \rangle$ scaled $p+\bar{p}$ and peripheral Au+Au reference data. The amount of energy loss to be consistent with the observed hadron suppression has been estimated to be 15 times greater than that in cold nucleus for an expanding medium. Since the energy loss is proportional to the initial gluon density, this implies that that the produced system may have a gluon density 15 times greater than inside a cold nucleus[105]. To isolate the contribution from partonic energy loss, Cronin and nuclear shadowing need to be measured in d+Au collisions. Neither the energy loss nor the saturation model is inconsistent with the Au+Au data at high $p_\perp$ at $\sqrt{s_{\mathrm{NN}}}$=130 GeV. Hopefully, d+Au collisions may help disentangle the two competing models. Since the saturation model only depends on the particulars of the gluon wavefunction, saturation should be present in d+Au collisions. For (15%) central d+Au events, R_{AA} at moderately high $p_\perp$ (4-6 GeV/c) is predicted to be ~ 0.7 [20]. On the other hand, the jet quenching model predicts no observable energy loss in d+Au. Factoring in Cronin and shadowing, R_{AA} is predicted to be above unity in the same $p_\perp$ region [101].

Appendices

Appendix A

Kinematics

	Definition
p	Total momentum.
p_z	Momentum along the beam line.
$p_\perp$	Momentum transverse to the beam line.
	$$p_\perp = \sqrt{p_x^2 + p_y^2}$$.
m_T (Transverse Mass)	$m_T^2 = m^2 + p_x^2 + p_y^2$
y (Rapidity)	$y = \frac{1}{2} \ln \left(\frac{E+p_z}{E-p_z} \right) = \ln \left(\frac{E+p_z}{m_T} \right) = \tanh^{-1} \left(\frac{p_z}{E} \right)$. Since $\delta y = \delta p_z / E$, the shape of dN/dy is boost invariant.
η (PseudoRapidity)	$\eta = -\ln \tan(\theta/2)$, where $\theta = p_z/p$. If $p \gg m$, $\eta \approx y$. η is commonly used over y when the particle mass is unknown.
Single particle inclusive process	$A + B \rightarrow C + X$, where A and B are the interacting particles, C the particle(s) of interest, and X all other final state particles.
$E\frac{\mathrm{d}^3 \mathrm{N_C}}{\mathrm{d}\mathbf{p}^3}$ (Differential invariant yield)	$$E\frac{\mathrm{d}^3 \mathrm{N_C}}{\mathrm{d}\mathbf{p}^3} = \frac{1}{\sigma_{A+B}} E\frac{\mathrm{d}^3 \sigma_\mathrm{C}}{\mathrm{d}\mathbf{p}^3} = \frac{1}{2\pi p_\perp} \frac{\mathrm{d}^2 \mathrm{N_C}}{\mathrm{dydp_\perp}}$$ The identity $dy/dp_z = 1/\mathrm{E}$ was used in the second equality.

	Definition
$f_{a/N}(x, Q^2)$ (Parton distribution function)	Probability density for parton a inside nucleon N to have a fraction x of the nucleon's longitudinal momentum at scale Q^2. $f_{a/N}(x, Q^2)$ are typically normalized so that $$\sum_h \int \mathrm{dx}\, \mathrm{x}\, \mathrm{f_{a/N}}(\mathrm{x}, \mathrm{Q}^2) = 1$$
$D_{h/c}(z_c, Q^2)$ (Fragmentation function)	Probability density for parton c to fragment into hadron h with momentum fraction $z_c \equiv p_L/p_{\mathrm{jet}}$ at scale Q^2; p_L and p_{jet} are the hadron and total jet momentum along the jet axis, respectively. $D_{h/c}(z_c, Q^2)$ are normalized so that $$\sum_h \int \mathrm{dz}\, \mathrm{dz}\, \mathrm{D_{h/c}}(\mathrm{z_c}, \mathrm{Q}^2) = 1$$

Appendix B

Simulation

The corrections to the yield [1] require an accurate simulation of the TPC response. The simulation framework begins with an event input to GSTAR, a STAR implemention of GEANT[1], which propagates particles according to the STAR geometry, material, and magnetic field, simulating physical processes such as particle decay, multiple scattering, and the ionization energy loss. The electron clusters are then passed through the TPC Response Simulator (TRS), which models TPC processes from electron transport and charge collection, to electronic response and final signal digitization (i.e. pixel data).

Most track corrections used data from the *embedding* procedure, where a few simulated tracks per event (5% of the primary charged multiplicity) were combined with real raw data. Aspects of the background were investigated using the HIJING event generator [input to GSTAR] and reconstructing the TRS raw data directly. The embedding technique is preferred over a pure simulation as it incorporates the real underlying physical environment of pad signals and noise. The embedded data was run through the usual reconstruction chain, (apart from turning off the TPC distortion corrections), and the reconstructed primary vertex of the embedded event was reset to the original vertex position.

Figures B.1, B.2, B.3 plots DCA3d, DCA2d, and the fit hits distributions, respectively, for real and embedded data.

---

[1]This section is taken almost verbatim from the Analysis Chapter.
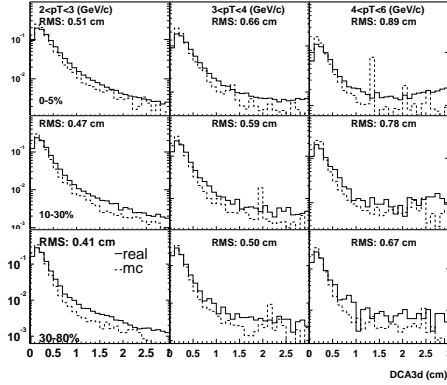
Figure B.1: DCA3d distribution for real (solid lines) and embedded data (dashed lines). The left, middle, and right panels are for $2 < p_\perp < 3$, $3 < p_\perp < 4$, and $4 < p_\perp < 6$ GeV/c respectively. The upper, middle, and lower panels are for 0-5%, 10-30%, and 30-80% central collisions respectively. The discrepancy for large DCA3d> 1 cm between real and embedded data is likely chiefly due to background in real events
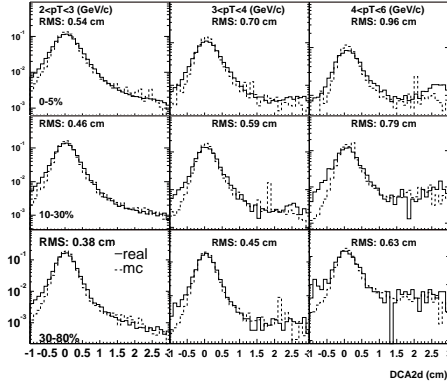
Figure B.2: DCA3d distribution for real (solid lines) and embedded data (dashed lines). The left, middle, and right panels are for $2 < p_\perp < 3$, $3 < p_\perp < 4$, and $4 < p_\perp < 6$ GeV/c respectively. The upper, middle, and lower panels are for 0-5%, 10-30%, and 30-80% central collisions respectively. The discrepancy for DCA2d< -1 cm between real and embedded data is chiefly due to background in real events.

95
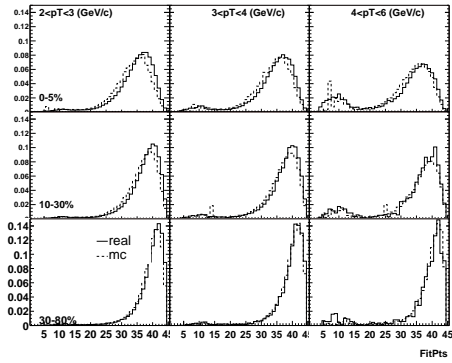
Figure B.3: Fit hits distribution for real (solid lines) and embedded data (dashed lines). The left, middle, and right panels are for $2 < p_\perp < 3$, $3 < p_\perp < 4$, and $4 < p_\perp < 6$ GeV/c respectively. The upper, middle, and lower panels are for 0-5%, 10-30%, and 30-80% central collisions respectively.

Appendix C

Corrections

C.1   Acceptance*Efficiency
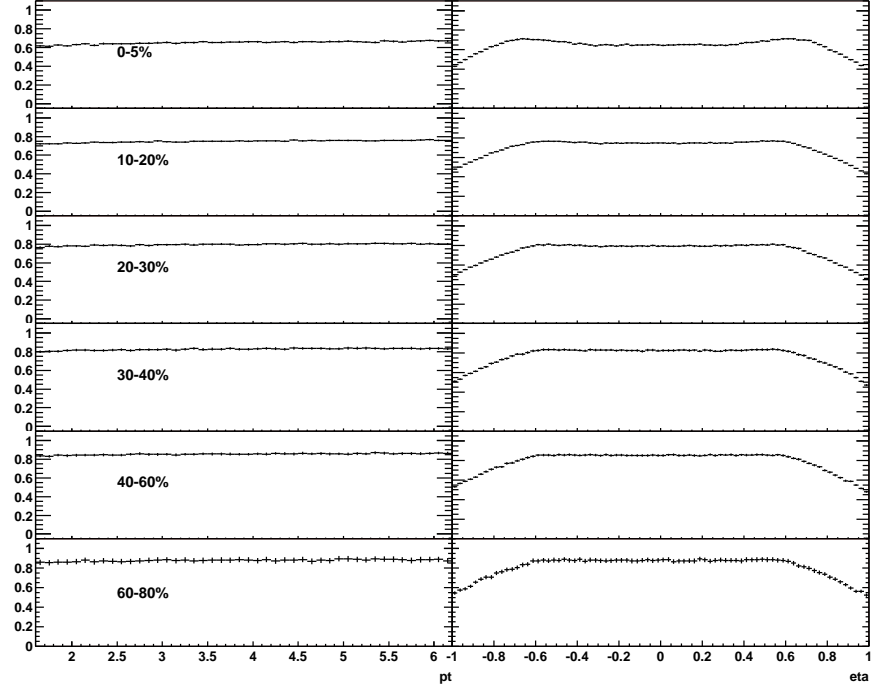
Figure C.1: Left: Acceptance*efficiency as a function of $p_\perp$, $|\eta| < 0.5$, for various centrality bins. Right: Acceptance*efficiency as a function of η, summed over $2 < p_\perp < 6$ GeV/c. The plots for the 0-5% centrality bin were summed over |event vertex z| < 75 cm; the remaining centrality bins summed over |event vertex z| < 95 cm; For the analysis a 2D function of η and $p_\perp$ was constructed. The 2D function was normalized at $\eta = 0$ and the weighted mean $p_\perp$ for $3 < p_\perp < 7$ GeV/c.

C.2 Curvature Resolution Vs p$_\perp$
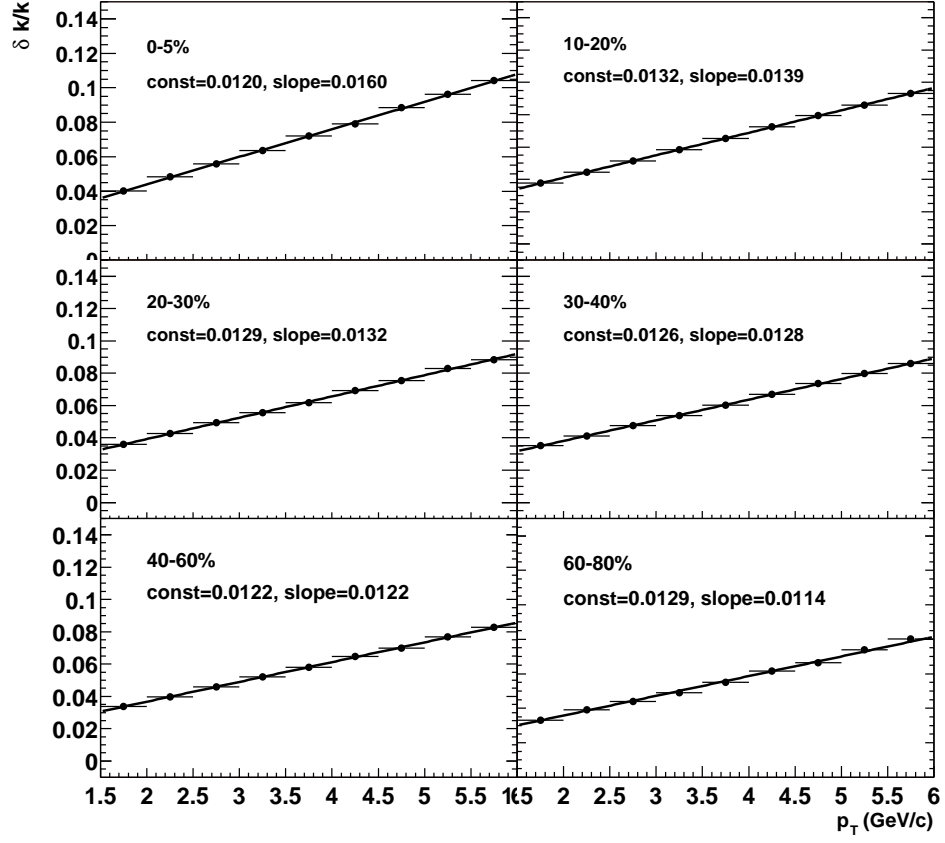
Figure C.2: $\delta k/k$ as a function of p$_\perp$, $(k \equiv 1/p_\perp)$, for various centrality bins.

C.3 Curvature Resolution Correction Vs $p_\perp$
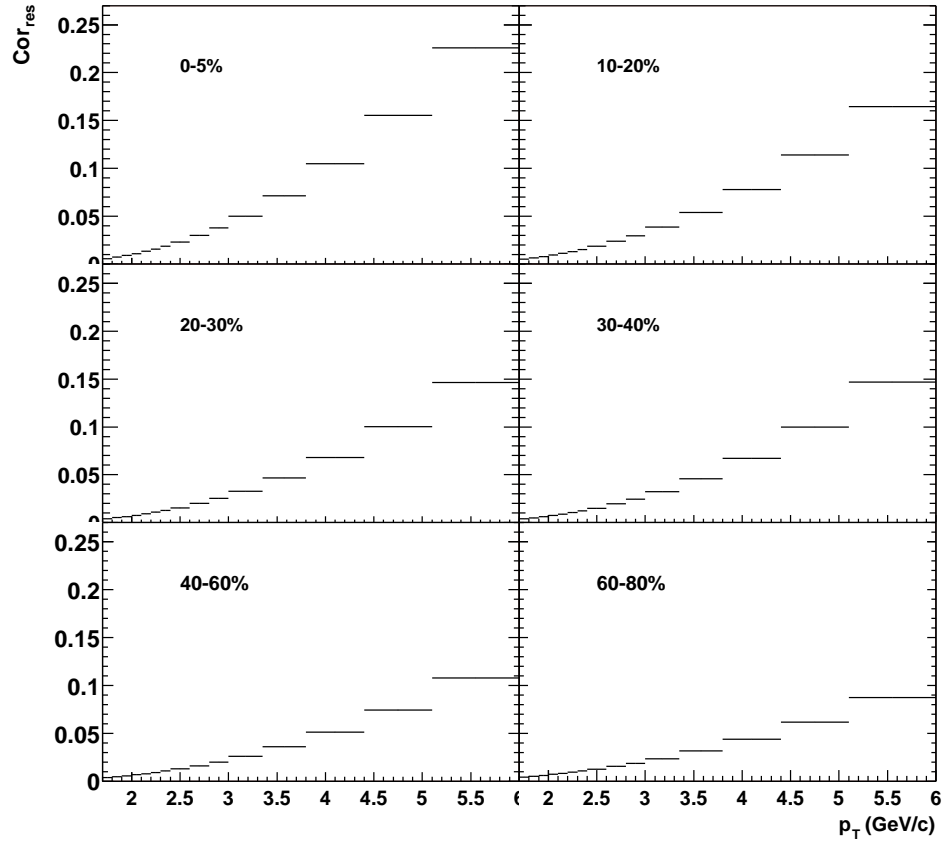
Figure C.3: 1-Cor$_{res}$, where Cor$_{res}$ is the multiplicative correction factor due to finite curvature resolution and a steeply falling distribution.

C.4 Background Fraction Vs $p_\perp$
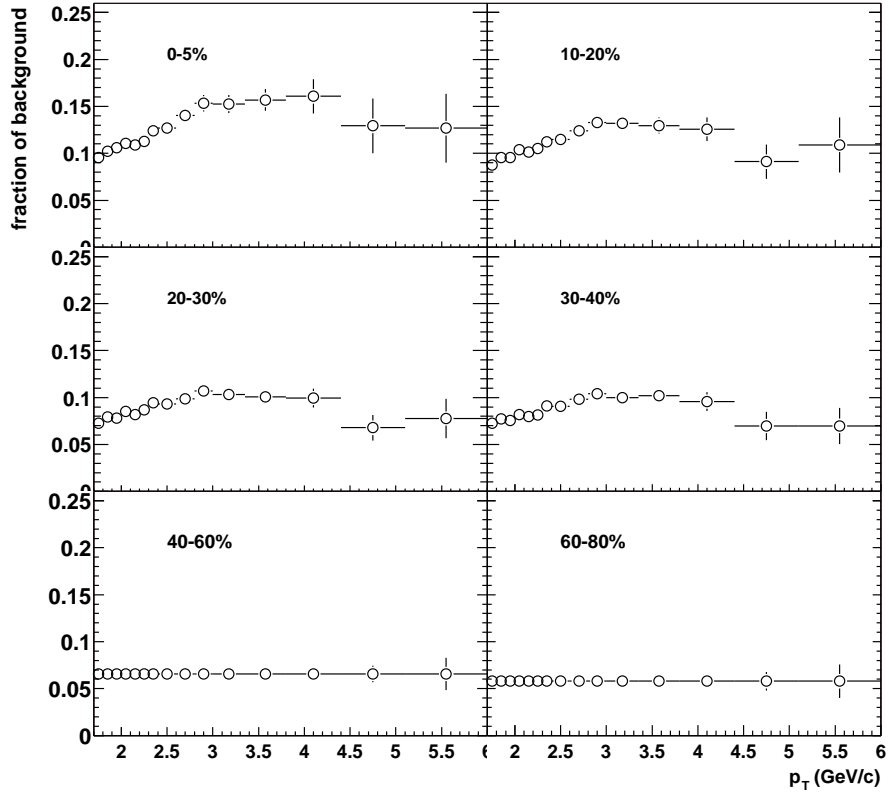
Figure C.4: Fraction of background as a function of $p_\perp$ for various centrality bins. The primary contributors are pions from $\overline{p}$, $\overline{n}$ annihilation in detector material and p and $\bar{p}$ from Λ , $\overline{\Lambda}$ decays. For the 40-60% and 60-80% bin, a uniforn background was used due to the large uncertainty in the measured parent Λ , $\overline{\Lambda}$ and $\bar{p}$ yields. Errors are statistical only.

Appendix D

NN Reference

	$\sqrt{s}$ (GeV)	$A\,\mathrm{mb/GeV^2}$	p_0 (GeV)	n
UA1 data	200	285	1.8	12.14
Best guess	130	266.6	1.895	12.98
Lower limit	130	260.8	2.07	13.91
Upper limit	130	270.5	1.8053	12.54

Table D.1: The NN reference for the R_{AA} plots was an interpolation to $\sqrt{s} = 130$ GeV of a power law fit to UA1 $\bar{p} + p$ data at $\sqrt{s} = 200..900$ GeV/c [24]. Details can be found in [100]. Writing the power law function as $E\frac{\mathrm{d}^3\sigma}{\mathrm{dp}^3} = A\left(1 + \frac{p_\perp}{p_0}\right)^{-n}$, the above table lists the interpolated parameters to $\sqrt{s} = 130$ GeV and for the UA1 data at $\sqrt{s} = 200$ GeV.
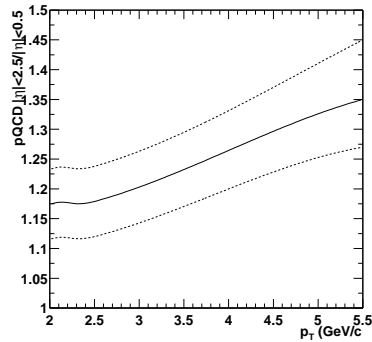
Figure D.1: The NN reference was corrected for the UA1 acceptance of $|\eta| < 2.5$ vs $|\eta| < 0.5$ for the present analysis using two independent pQCD calculations [46, 99], which yielded a multiplicative correction factor of 1.17 ± 0.06 at $\mathrm{p}_\perp = 2$ GeV/c and 1.35 ± 0.10 at $\mathrm{p}_\perp = 5.5$ GeV/c. The lower and upper uncertainty limits to the correction are illustrated by the dashed lines.

Appendix E

Differential Invariant Yield

	0-5%			
	$1/(2\pi p_\perp)\,\mathrm{d}^2\mathrm{N}^{(\mathrm{h}^+ +\mathrm{h}^-)/2}/\mathrm{dp}_\perp\mathrm{d}\eta|_{|\eta|<0.5}\,((\mathrm{GeV/c})^2)$			
$p_\perp$ (GeV/c)	(value)		(uncertainty)	
		(stat)	(sys)	(total)
$1.70 \leq 1.75 < 1.80$	1.09e+00	±2.13e-03	±1.72e-01	±1.72e-01
$1.80 \leq 1.85 < 1.90$	7.89e-01	±1.75e-03	±1.29e-01	±1.29e-01
$1.90 \leq 1.95 < 2.00$	5.71e-01	±1.44e-03	±9.49e-02	±9.49e-02
$2.00 \leq 2.05 < 2.10$	4.08e-01	±1.19e-03	±6.97e-02	±6.97e-02
$2.10 \leq 2.15 < 2.20$	2.96e-01	±9.84e-04	±5.00e-02	±5.00e-02
$2.20 \leq 2.25 < 2.30$	2.16e-01	±8.17e-04	±3.72e-02	±3.72e-02
$2.30 \leq 2.35 < 2.40$	1.57e-01	±6.74e-04	±2.87e-02	±2.88e-02
$2.40 \leq 2.49 < 2.60$	9.99e-02	±3.67e-04	±1.86e-02	±1.86e-02
$2.60 \leq 2.69 < 2.80$	5.34e-02	±2.55e-04	±1.07e-02	±1.07e-02
$2.80 \leq 2.89 < 3.00$	2.96e-02	±1.81e-04	±6.39e-03	±6.39e-03
$3.00 \leq 3.16 < 3.35$	1.39e-02	±8.89e-05	±3.14e-03	±3.14e-03
$3.35 \leq 3.55 < 3.80$	4.84e-03	±4.28e-05	±1.22e-03	±1.22e-03
$3.80 \leq 4.06 < 4.40$	1.35e-03	±1.79e-05	±3.49e-04	±3.49e-04
$4.40 \leq 4.70 < 5.10$	3.39e-04	±7.62e-06	±8.64e-05	±8.67e-05
$5.10 \leq 5.48 < 6.00$	7.03e-05	±2.71e-06	±1.99e-05	±2.01e-05

Table E.1: The total uncertainty is the quadrature sum of the statistical and systematic uncertainties.

	5-10%			
	$1/(2\pi p_\perp)\,\mathrm{d}^2\mathrm{N}^{(\mathrm{h}^++\mathrm{h}^-)/2}/\mathrm{dp}_\perp\mathrm{d}\eta|_{|\eta|<0.5}\,((\mathrm{GeV/c})^2)$			
$p_\perp$ (GeV/c)	(value)		(uncertainty)	
		(stat)	(sys)	(total)
$1.70 \leq 1.75 < 1.80$	8.63e-01	$\pm$2.01e-03	$\pm$1.26e-01	$\pm$1.26e-01
$1.80 \leq 1.85 < 1.90$	6.20e-01	$\pm$1.65e-03	$\pm$9.44e-02	$\pm$9.44e-02
$1.90 \leq 1.95 < 2.00$	4.48e-01	$\pm$1.36e-03	$\pm$6.98e-02	$\pm$6.98e-02
$2.00 \leq 2.05 < 2.10$	3.22e-01	$\pm$1.12e-03	$\pm$5.16e-02	$\pm$5.17e-02
$2.10 \leq 2.15 < 2.20$	2.38e-01	$\pm$9.38e-04	$\pm$3.75e-02	$\pm$3.75e-02
$2.20 \leq 2.25 < 2.30$	1.73e-01	$\pm$7.78e-04	$\pm$2.79e-02	$\pm$2.79e-02
$2.30 \leq 2.35 < 2.40$	1.25e-01	$\pm$6.43e-04	$\pm$2.17e-02	$\pm$2.17e-02
$2.40 \leq 2.49 < 2.60$	8.04e-02	$\pm$3.51e-04	$\pm$1.41e-02	$\pm$1.41e-02
$2.60 \leq 2.69 < 2.80$	4.38e-02	$\pm$2.46e-04	$\pm$8.22e-03	$\pm$8.22e-03
$2.80 \leq 2.90 < 3.00$	2.41e-02	$\pm$1.74e-04	$\pm$5.01e-03	$\pm$5.01e-03
$3.00 \leq 3.16 < 3.35$	1.14e-02	$\pm$8.59e-05	$\pm$2.49e-03	$\pm$2.49e-03
$3.35 \leq 3.55 < 3.80$	4.08e-03	$\pm$4.22e-05	$\pm$9.87e-04	$\pm$9.87e-04
$3.80 \leq 4.06 < 4.40$	1.19e-03	$\pm$1.82e-05	$\pm$2.91e-04	$\pm$2.92e-04
$4.40 \leq 4.70 < 5.10$	3.02e-04	$\pm$7.76e-06	$\pm$7.45e-05	$\pm$7.49e-05
$5.10 \leq 5.48 < 6.00$	6.30e-05	$\pm$2.79e-06	$\pm$1.74e-05	$\pm$1.76e-05

	10-20%			
	$1/(2\pi p_\perp)\,\mathrm{d}^2\mathrm{N}^{(\mathrm{h}^++\mathrm{h}^-)/2}/\mathrm{dp}_\perp\mathrm{d}\eta|_{|\eta|<0.5}\,((\mathrm{GeV/c})^2)$			
$p_\perp$ (GeV/c)	(value)		(uncertainty)	
		(stat)	(sys)	(total)
$1.70 \leq 1.75 < 1.80$	6.30e-01	$\pm$3.86e-03	$\pm$9.08e-02	$\pm$9.09e-02
$1.80 \leq 1.85 < 1.90$	4.58e-01	$\pm$3.18e-03	$\pm$6.91e-02	$\pm$6.92e-02
$1.90 \leq 1.95 < 2.00$	3.32e-01	$\pm$2.63e-03	$\pm$5.01e-02	$\pm$5.02e-02
$2.00 \leq 2.05 < 2.10$	2.38e-01	$\pm$2.17e-03	$\pm$3.76e-02	$\pm$3.77e-02
$2.10 \leq 2.15 < 2.20$	1.78e-01	$\pm$1.83e-03	$\pm$2.78e-02	$\pm$2.79e-02
$2.20 \leq 2.25 < 2.30$	1.28e-01	$\pm$1.51e-03	$\pm$2.04e-02	$\pm$2.05e-02
$2.30 \leq 2.35 < 2.40$	9.60e-02	$\pm$1.27e-03	$\pm$1.59e-02	$\pm$1.60e-02
$2.40 \leq 2.49 < 2.60$	6.10e-02	$\pm$6.92e-04	$\pm$1.03e-02	$\pm$1.03e-02
$2.60 \leq 2.69 < 2.80$	3.35e-02	$\pm$4.88e-04	$\pm$5.97e-03	$\pm$5.99e-03
$2.80 \leq 2.90 < 3.00$	1.87e-02	$\pm$3.49e-04	$\pm$3.61e-03	$\pm$3.62e-03
$3.00 \leq 3.16 < 3.35$	9.02e-03	$\pm$1.74e-04	$\pm$1.83e-03	$\pm$1.84e-03
$3.35 \leq 3.55 < 3.80$	3.30e-03	$\pm$8.70e-05	$\pm$7.40e-04	$\pm$7.45e-04
$3.80 \leq 4.06 < 4.40$	9.84e-04	$\pm$3.79e-05	$\pm$2.19e-04	$\pm$2.22e-04
$4.40 \leq 4.70 < 5.10$	2.88e-04	$\pm$1.77e-05	$\pm$6.46e-05	$\pm$6.70e-05
$5.10 \leq 5.48 < 6.00$	5.50e-05	$\pm$6.03e-06	$\pm$1.42e-05	$\pm$1.55e-05

			20-30%	
	$1/(2\pi p_\perp)\, \mathrm{d^2N^{(h^++h^-)/2}}/\mathrm{dp_\perp d\eta}|_{|\eta|<0.5}\, ((\mathrm{GeV/c})^2)$			
$\mathrm{p_\perp}$ (GeV/c)	(value)		(uncertainty)	
		(stat)	(sys)	(total)
$1.70 \leq 1.75 < 1.80$	4.24e-01	±3.07e-03	±5.64e-02	±5.65e-02
$1.80 \leq 1.85 < 1.90$	3.05e-01	±2.52e-03	±4.20e-02	±4.21e-02
$1.90 \leq 1.95 < 2.00$	2.25e-01	±2.10e-03	±3.07e-02	±3.08e-02
$2.00 \leq 2.05 < 2.10$	1.59e-01	±1.72e-03	±2.27e-02	±2.27e-02
$2.10 \leq 2.15 < 2.20$	1.22e-01	±1.47e-03	±1.70e-02	±1.71e-02
$2.20 \leq 2.25 < 2.30$	8.53e-02	±1.20e-03	±1.22e-02	±1.23e-02
$2.30 \leq 2.35 < 2.40$	6.37e-02	±1.01e-03	±9.53e-03	±9.58e-03
$2.40 \leq 2.49 < 2.60$	4.24e-02	±5.62e-04	±6.30e-03	±6.32e-03
$2.60 \leq 2.70 < 2.80$	2.40e-02	±4.05e-04	±3.69e-03	±3.71e-03
$2.80 \leq 2.90 < 3.00$	1.34e-02	±2.89e-04	±2.23e-03	±2.25e-03
$3.00 \leq 3.16 < 3.35$	6.55e-03	±1.46e-04	±1.16e-03	±1.17e-03
$3.35 \leq 3.55 < 3.80$	2.41e-03	±7.31e-05	±4.85e-04	±4.90e-04
$3.80 \leq 4.06 < 4.40$	7.07e-04	±3.16e-05	±1.42e-04	±1.46e-04
$4.40 \leq 4.71 < 5.10$	2.15e-04	±1.50e-05	±4.54e-05	±4.78e-05
$5.10 \leq 5.48 < 6.00$	4.76e-05	±5.57e-06	±1.14e-05	±1.27e-05

			30-40%	
	$1/(2\pi p_\perp)\, \mathrm{d^2N^{(h^++h^-)/2}}/\mathrm{dp_\perp d\eta}|_{|\eta|<0.5}\, ((\mathrm{GeV/c})^2)$			
$\mathrm{p_\perp}$ (GeV/c)	(value)		(uncertainty)	
		(stat)	(sys)	(total)
$1.70 \leq 1.75 < 1.80$	2.58e-01	±2.36e-03	±3.11e-02	±3.12e-02
$1.80 \leq 1.85 < 1.90$	1.92e-01	±1.97e-03	±2.38e-02	±2.38e-02
$1.90 \leq 1.95 < 2.00$	1.40e-01	±1.63e-03	±1.72e-02	±1.73e-02
$2.00 \leq 2.05 < 2.10$	1.00e-01	±1.35e-03	±1.28e-02	±1.28e-02
$2.10 \leq 2.15 < 2.20$	7.55e-02	±1.14e-03	±9.49e-03	±9.56e-03
$2.20 \leq 2.25 < 2.30$	5.50e-02	±9.48e-04	±7.00e-03	±7.07e-03
$2.30 \leq 2.35 < 2.40$	4.00e-02	±7.86e-04	±5.42e-03	±5.48e-03
$2.40 \leq 2.49 < 2.60$	2.64e-02	±4.37e-04	±3.56e-03	±3.59e-03
$2.60 \leq 2.70 < 2.80$	1.46e-02	±3.10e-04	±2.07e-03	±2.10e-03
$2.80 \leq 2.90 < 3.00$	8.30e-03	±2.24e-04	±1.23e-03	±1.25e-03
$3.00 \leq 3.16 < 3.35$	4.07e-03	±1.13e-04	±6.08e-04	±6.19e-04
$3.35 \leq 3.55 < 3.80$	1.39e-03	±5.46e-05	±2.27e-04	±2.34e-04
$3.80 \leq 4.06 < 4.40$	4.31e-04	±2.44e-05	±7.08e-05	±7.49e-05
$4.40 \leq 4.70 < 5.10$	1.16e-04	±1.08e-05	±1.93e-05	±2.21e-05
$5.10 \leq 5.48 < 6.00$	3.14e-05	±4.48e-06	±6.23e-06	±7.68e-06

40-60%

p$_\perp$ (GeV/c)	$1/(2\pi p_\perp)\,\mathrm{d}^2\mathrm{N}^{(\mathrm{h}^+ + \mathrm{h}^-)/2}/\mathrm{d}p_\perp\mathrm{d}\eta\|_{\|\eta\|<0.5}\,((\mathrm{GeV/c})^2)$ (value)	(uncertainty)		
		(stat)	(sys)	(total)
$1.70 \leq 1.75 < 1.80$	1.18e-01	±1.12e-03	±1.36e-02	±1.37e-02
$1.80 \leq 1.85 < 1.90$	8.77e-02	±9.32e-04	±1.01e-02	±1.01e-02
$1.90 \leq 1.95 < 2.00$	6.21e-02	±7.63e-04	±7.16e-03	±7.20e-03
$2.00 \leq 2.05 < 2.10$	4.69e-02	±6.47e-04	±5.39e-03	±5.43e-03
$2.10 \leq 2.15 < 2.20$	3.40e-02	±5.38e-04	±3.92e-03	±3.95e-03
$2.20 \leq 2.25 < 2.30$	2.54e-02	±4.53e-04	±2.92e-03	±2.95e-03
$2.30 \leq 2.35 < 2.40$	1.93e-02	±3.86e-04	±2.22e-03	±2.26e-03
$2.40 \leq 2.50 < 2.60$	1.23e-02	±2.11e-04	±1.42e-03	±1.43e-03
$2.60 \leq 2.70 < 2.80$	7.09e-03	±1.54e-04	±8.17e-04	±8.31e-04
$2.80 \leq 2.90 < 3.00$	4.04e-03	±1.12e-04	±4.66e-04	±4.79e-04
$3.00 \leq 3.16 < 3.35$	2.17e-03	±5.89e-05	±2.64e-04	±2.70e-04
$3.35 \leq 3.55 < 3.80$	7.76e-04	±2.92e-05	±1.05e-04	±1.09e-04
$3.80 \leq 4.07 < 4.40$	2.64e-04	±1.37e-05	±3.82e-05	±4.05e-05
$4.40 \leq 4.71 < 5.10$	7.38e-05	±6.15e-06	±1.19e-05	±1.34e-05
$5.10 \leq 5.49 < 6.00$	1.68e-05	±2.35e-06	±3.19e-06	±3.96e-06

60-80%

p$_\perp$ (GeV/c)	$1/(2\pi p_\perp)\,\mathrm{d}^2\mathrm{N}^{(\mathrm{h}^+ + \mathrm{h}^-)/2}/\mathrm{d}p_\perp\mathrm{d}\eta\|_{\|\eta\|<0.5}\,((\mathrm{GeV/c})^2)$ (value)	(uncertainty)		
		(stat)	(sys)	(total)
$1.70 \leq 1.75 < 1.80$	2.96e-02	±5.43e-04	±4.15e-03	±4.18e-03
$1.80 \leq 1.85 < 1.90$	2.04e-02	±4.38e-04	±2.86e-03	±2.89e-03
$1.90 \leq 1.95 < 2.00$	1.49e-02	±3.64e-04	±2.09e-03	±2.12e-03
$2.00 \leq 2.05 < 2.10$	1.14e-02	±3.10e-04	±1.59e-03	±1.62e-03
$2.10 \leq 2.15 < 2.20$	8.23e-03	±2.57e-04	±1.15e-03	±1.18e-03
$2.20 \leq 2.25 < 2.30$	6.09e-03	±2.16e-04	±8.53e-04	±8.80e-04
$2.30 \leq 2.35 < 2.40$	4.45e-03	±1.80e-04	±6.24e-04	±6.50e-04
$2.40 \leq 2.49 < 2.60$	3.00e-03	±1.01e-04	±4.20e-04	±4.32e-04
$2.60 \leq 2.70 < 2.80$	1.71e-03	±7.36e-05	±2.40e-04	±2.51e-04
$2.80 \leq 2.90 < 3.00$	1.08e-03	±5.61e-05	±1.51e-04	±1.61e-04
$3.00 \leq 3.16 < 3.35$	4.96e-04	±2.75e-05	±7.22e-05	±7.72e-05
$3.35 \leq 3.55 < 3.80$	2.01e-04	±1.45e-05	±3.14e-05	±3.46e-05
$3.80 \leq 4.07 < 4.40$	6.87e-05	±6.83e-06	±1.12e-05	±1.31e-05
$4.40 \leq 4.71 < 5.10$	1.97e-05	±3.12e-06	±3.57e-06	±4.74e-06
$5.10 \leq 5.49 < 6.00$	5.06e-06	±1.26e-06	±1.02e-06	±1.62e-06

Appendix F

Central Over Peripheral

p$_\perp$ (GeV/c)	0-5%/40-60% (dN/dp$_\perp$$\langle$N$_{bin}$$\rangle$)$_{cent}$/(dN/dp$_\perp$/$\langle$mN$_{bin}$$\rangle$)$_{periph}$			
	(value)		(uncertainty)	
		(central)	(total)	($\langle$N$_{bin}$$\rangle$)
$1.70 \leq 1.75 < 1.80$	0.86	± 0.14	± 0.17	$+0.29/-0.17$
$1.80 \leq 1.85 < 1.90$	0.84	± 0.14	± 0.17	$+0.29/-0.17$
$1.90 \leq 1.95 < 2.00$	0.85	± 0.14	± 0.17	$+0.29/-0.17$
$2.00 \leq 2.05 < 2.10$	0.81	± 0.14	± 0.17	$+0.28/-0.16$
$2.10 \leq 2.15 < 2.20$	0.81	± 0.14	± 0.17	$+0.28/-0.16$
$2.20 \leq 2.25 < 2.30$	0.79	± 0.14	± 0.16	$+0.27/-0.16$
$2.30 \leq 2.35 < 2.40$	0.76	± 0.14	± 0.16	$+0.26/-0.15$
$2.40 \leq 2.49 < 2.60$	0.75	± 0.14	± 0.17	$+0.26/-0.15$
$2.60 \leq 2.69 < 2.80$	0.70	± 0.14	± 0.16	$+0.24/-0.14$
$2.80 \leq 2.89 < 3.00$	0.68	± 0.15	± 0.17	$+0.23/-0.14$
$3.00 \leq 3.16 < 3.35$	0.60	± 0.14	± 0.15	$+0.20/-0.12$
$3.35 \leq 3.55 < 3.80$	0.58	± 0.15	± 0.17	$+0.20/-0.12$
$3.80 \leq 4.06 < 4.40$	0.48	± 0.12	± 0.14	$+0.16/-0.10$
$4.40 \leq 4.70 < 5.10$	0.43	± 0.11	± 0.13	$+0.15/-0.09$
$5.10 \leq 5.48 < 6.00$	0.39	± 0.11	± 0.14	$+0.13/-0.08$
0-5%/60-80%				
$1.70 \leq 1.75 < 1.80$	0.75	± 0.12	± 0.16	$+0.53/-0.22$
$1.80 \leq 1.85 < 1.90$	0.78	± 0.13	± 0.17	$+0.55/-0.23$
$1.90 \leq 1.95 < 2.00$	0.78	± 0.13	± 0.17	$+0.55/-0.23$
$2.00 \leq 2.05 < 2.10$	0.73	± 0.12	± 0.16	$+0.52/-0.21$
$2.10 \leq 2.15 < 2.20$	0.73	± 0.12	± 0.16	$+0.52/-0.21$
$2.20 \leq 2.25 < 2.30$	0.72	± 0.12	± 0.16	$+0.51/-0.21$
$2.30 \leq 2.35 < 2.40$	0.72	± 0.13	± 0.17	$+0.51/-0.21$
$2.40 \leq 2.49 < 2.60$	0.68	± 0.13	± 0.16	$+0.48/-0.20$
$2.60 \leq 2.69 < 2.80$	0.63	± 0.13	± 0.16	$+0.45/-0.19$
$2.80 \leq 2.89 < 3.00$	0.56	± 0.12	± 0.15	$+0.39/-0.16$
$3.00 \leq 3.16 < 3.35$	0.57	± 0.13	± 0.16	$+0.40/-0.17$
$3.35 \leq 3.55 < 3.80$	0.49	± 0.12	± 0.15	$+0.35/-0.14$
$3.80 \leq 4.06 < 4.40$	0.40	± 0.10	± 0.13	$+0.28/-0.12$
$4.40 \leq 4.70 < 5.10$	0.35	± 0.09	± 0.12	$+0.25/-0.10$
$5.10 \leq 5.48 < 6.00$	0.28	± 0.08	± 0.12	$+0.20/-0.08$

Table F.1: The total uncertainty is the quadrature sum of the systematic uncertainties for the central and peripheral yields.

Appendix G

R_{AA}

	0-5%			
	$d^2N/d\eta dp_\perp(STAR)/T_{AA}d^2\sigma/d\eta dp_\perp(NN)$			
$p_\perp$ (GeV/c)	(value)		(uncertainty)	
		(data)	(total)	($\langle N_{bin}\rangle$)
$1.70 \leq 1.75 < 1.80$	0.71	± 0.11	± 0.13	$+0.05/-0.05$
$1.80 \leq 1.85 < 1.90$	0.73	± 0.12	± 0.14	$+0.05/-0.05$
$1.90 \leq 1.95 < 2.00$	0.74	± 0.12	± 0.15	$+0.06/-0.05$
$2.00 \leq 2.05 < 2.10$	0.74	± 0.13	± 0.15	$+0.06/-0.05$
$2.10 \leq 2.15 < 2.20$	0.74	± 0.13	± 0.16	$+0.06/-0.05$
$2.20 \leq 2.25 < 2.30$	0.74	± 0.13	± 0.16	$+0.06/-0.05$
$2.30 \leq 2.35 < 2.40$	0.74	± 0.13	± 0.17	$+0.05/-0.05$
$2.40 \leq 2.49 < 2.60$	0.73	± 0.14	± 0.17	$+0.05/-0.05$
$2.60 \leq 2.69 < 2.80$	0.69	± 0.14	± 0.18	$+0.05/-0.04$
$2.80 \leq 2.89 < 3.00$	0.66	± 0.14	± 0.18	$+0.05/-0.04$
$3.00 \leq 3.16 < 3.35$	0.62	± 0.14	± 0.18	$+0.05/-0.04$
$3.35 \leq 3.55 < 3.80$	0.55	± 0.14	± 0.19	$+0.04/-0.04$
$3.80 \leq 4.06 < 4.40$	0.48	± 0.12	± 0.18	$+0.04/-0.03$
$4.40 \leq 4.70 < 5.10$	0.44	± 0.11	± 0.17	$+0.03/-0.03$
$5.10 \leq 5.48 < 6.00$	0.37	± 0.11	± 0.17	$+0.03/-0.02$

Table G.1: The total uncertainty is the quadrature sum of the data and NN reference uncertainties.

		5-10%		
	$d^2N/d\eta dp_\perp(STAR)/T_{AA}d^2\sigma/d\eta dp_\perp(NN)$		
$p_\perp$ (GeV/c)	(value)		(uncertainty)	
		(data)	(total)	($\langle N_{bin}\rangle$)
$1.70 \leq 1.75 < 1.80$	0.71	± 0.10	± 0.12	$+0.06/-0.05$
$1.80 \leq 1.85 < 1.90$	0.72	± 0.11	± 0.13	$+0.06/-0.05$
$1.90 \leq 1.95 < 2.00$	0.74	± 0.11	± 0.14	$+0.07/-0.05$
$2.00 \leq 2.05 < 2.10$	0.74	± 0.12	± 0.15	$+0.07/-0.05$
$2.10 \leq 2.15 < 2.20$	0.75	± 0.12	± 0.15	$+0.07/-0.05$
$2.20 \leq 2.25 < 2.30$	0.75	± 0.12	± 0.16	$+0.07/-0.05$
$2.30 \leq 2.35 < 2.40$	0.74	± 0.13	± 0.16	$+0.07/-0.05$
$2.40 \leq 2.49 < 2.60$	0.74	± 0.13	± 0.17	$+0.07/-0.05$
$2.60 \leq 2.69 < 2.80$	0.71	± 0.13	± 0.18	$+0.06/-0.05$
$2.80 \leq 2.90 < 3.00$	0.67	± 0.14	± 0.19	$+0.06/-0.05$
$3.00 \leq 3.16 < 3.35$	0.63	± 0.14	± 0.19	$+0.06/-0.05$
$3.35 \leq 3.55 < 3.80$	0.59	± 0.14	± 0.19	$+0.05/-0.04$
$3.80 \leq 4.06 < 4.40$	0.54	± 0.13	± 0.19	$+0.05/-0.04$
$4.40 \leq 4.70 < 5.10$	0.49	± 0.12	± 0.19	$+0.04/-0.04$
$5.10 \leq 5.48 < 6.00$	0.42	± 0.12	± 0.19	$+0.04/-0.03$

		10-20%		
	$d^2N/d\eta dp_\perp(STAR)/T_{AA}d^2\sigma/d\eta dp_\perp(NN)$		
$p_\perp$ (GeV/c)	(value)		(uncertainty)	
		(data)	(total)	($\langle N_{bin}\rangle$)
$1.70 \leq 1.75 < 1.80$	0.71	± 0.10	± 0.12	$+0.08/-0.06$
$1.80 \leq 1.85 < 1.90$	0.74	± 0.11	± 0.13	$+0.08/-0.06$
$1.90 \leq 1.95 < 2.00$	0.76	± 0.11	± 0.14	$+0.09/-0.06$
$2.00 \leq 2.05 < 2.10$	0.76	± 0.12	± 0.15	$+0.09/-0.06$
$2.10 \leq 2.15 < 2.20$	0.78	± 0.12	± 0.16	$+0.09/-0.06$
$2.20 \leq 2.25 < 2.30$	0.77	± 0.12	± 0.16	$+0.09/-0.06$
$2.30 \leq 2.35 < 2.40$	0.79	± 0.13	± 0.17	$+0.09/-0.06$
$2.40 \leq 2.49 < 2.60$	0.78	± 0.13	± 0.18	$+0.09/-0.06$
$2.60 \leq 2.69 < 2.80$	0.76	± 0.14	± 0.18	$+0.09/-0.06$
$2.80 \leq 2.90 < 3.00$	0.73	± 0.14	± 0.19	$+0.08/-0.06$
$3.00 \leq 3.16 < 3.35$	0.70	± 0.14	± 0.20	$+0.08/-0.06$
$3.35 \leq 3.55 < 3.80$	0.66	± 0.15	± 0.21	$+0.07/-0.05$
$3.80 \leq 4.06 < 4.40$	0.61	± 0.14	± 0.21	$+0.07/-0.05$
$4.40 \leq 4.70 < 5.10$	0.66	± 0.15	± 0.25	$+0.07/-0.05$
$5.10 \leq 5.48 < 6.00$	0.51	± 0.14	± 0.23	$+0.06/-0.04$

	20-30%			
	$\mathrm{d^2N/d\eta dp_\perp(STAR)/T_{AA}d^2\sigma/d\eta dp_\perp(NN)}$			
$p_\perp$ (GeV/c)	(value)		(uncertainty)	
		(data)	(total)	($\langle N_{bin}\rangle$)
$1.70 \leq 1.75 < 1.80$	0.76	± 0.10	± 0.12	$+0.11/-0.09$
$1.80 \leq 1.85 < 1.90$	0.78	± 0.11	± 0.13	$+0.12/-0.09$
$1.90 \leq 1.95 < 2.00$	0.81	± 0.11	± 0.14	$+0.12/-0.09$
$2.00 \leq 2.05 < 2.10$	0.80	± 0.11	± 0.15	$+0.12/-0.09$
$2.10 \leq 2.15 < 2.20$	0.85	± 0.12	± 0.16	$+0.13/-0.10$
$2.20 \leq 2.25 < 2.30$	0.81	± 0.12	± 0.16	$+0.12/-0.09$
$2.30 \leq 2.35 < 2.40$	0.83	± 0.12	± 0.17	$+0.12/-0.10$
$2.40 \leq 2.49 < 2.60$	0.85	± 0.13	± 0.18	$+0.13/-0.10$
$2.60 \leq 2.70 < 2.80$	0.86	± 0.13	± 0.19	$+0.13/-0.10$
$2.80 \leq 2.90 < 3.00$	0.82	± 0.14	± 0.20	$+0.12/-0.09$
$3.00 \leq 3.16 < 3.35$	0.80	± 0.14	± 0.21	$+0.12/-0.09$
$3.35 \leq 3.55 < 3.80$	0.77	± 0.16	± 0.23	$+0.11/-0.09$
$3.80 \leq 4.06 < 4.40$	0.70	± 0.14	± 0.23	$+0.10/-0.08$
$4.40 \leq 4.71 < 5.10$	0.78	± 0.17	± 0.29	$+0.12/-0.09$
$5.10 \leq 5.48 < 6.00$	0.71	± 0.19	± 0.31	$+0.11/-0.08$

	30-40%			
	$\mathrm{d^2N/d\eta dp_\perp(STAR)/T_{AA}d^2\sigma/d\eta dp_\perp(NN)}$			
$p_\perp$ (GeV/c)	(value)		(uncertainty)	
		(data)	(total)	($\langle N_{bin}\rangle$)
$1.70 \leq 1.75 < 1.80$	0.77	± 0.09	± 0.12	$+0.16/-0.11$
$1.80 \leq 1.85 < 1.90$	0.81	± 0.10	± 0.13	$+0.17/-0.12$
$1.90 \leq 1.95 < 2.00$	0.84	± 0.10	± 0.14	$+0.17/-0.12$
$2.00 \leq 2.05 < 2.10$	0.84	± 0.11	± 0.14	$+0.17/-0.12$
$2.10 \leq 2.15 < 2.20$	0.87	± 0.11	± 0.15	$+0.18/-0.13$
$2.20 \leq 2.25 < 2.30$	0.87	± 0.11	± 0.16	$+0.18/-0.13$
$2.30 \leq 2.35 < 2.40$	0.87	± 0.12	± 0.17	$+0.18/-0.13$
$2.40 \leq 2.49 < 2.60$	0.88	± 0.12	± 0.18	$+0.18/-0.13$
$2.60 \leq 2.70 < 2.80$	0.86	± 0.12	± 0.19	$+0.18/-0.13$
$2.80 \leq 2.90 < 3.00$	0.85	± 0.13	± 0.20	$+0.18/-0.12$
$3.00 \leq 3.16 < 3.35$	0.83	± 0.13	± 0.21	$+0.17/-0.12$
$3.35 \leq 3.55 < 3.80$	0.73	± 0.12	± 0.21	$+0.15/-0.11$
$3.80 \leq 4.06 < 4.40$	0.71	± 0.12	± 0.22	$+0.15/-0.10$
$4.40 \leq 4.70 < 5.10$	0.70	± 0.13	± 0.25	$+0.14/-0.10$
$5.10 \leq 5.48 < 6.00$	0.77	± 0.19	± 0.33	$+0.16/-0.11$

	40-60%			
	d^{2}N/dηdp$_\perp$(STAR)/T$_{AA}$d^{2}σ/dηdp$_\perp$(NN)			
p$_\perp$ (GeV/c)	(value)		(uncertainty)	
		(data)	(total)	(⟨N$_{bin}$⟩)
$1.70 \leq 1.75 < 1.80$	0.82	±0.10	±0.12	+0.27/ − 0.16
$1.80 \leq 1.85 < 1.90$	0.87	±0.10	±0.13	+0.28/ − 0.17
$1.90 \leq 1.95 < 2.00$	0.87	±0.10	±0.14	+0.28/ − 0.17
$2.00 \leq 2.05 < 2.10$	0.91	±0.11	±0.15	+0.30/ − 0.18
$2.10 \leq 2.15 < 2.20$	0.92	±0.11	±0.16	+0.30/ − 0.18
$2.20 \leq 2.25 < 2.30$	0.94	±0.11	±0.16	+0.30/ − 0.18
$2.30 \leq 2.35 < 2.40$	0.97	±0.11	±0.18	+0.32/ − 0.19
$2.40 \leq 2.50 < 2.60$	0.96	±0.11	±0.18	+0.31/ − 0.19
$2.60 \leq 2.70 < 2.80$	0.98	±0.12	±0.20	+0.32/ − 0.19
$2.80 \leq 2.90 < 3.00$	0.96	±0.11	±0.21	+0.31/ − 0.19
$3.00 \leq 3.16 < 3.35$	1.03	±0.13	±0.24	+0.33/ − 0.20
$3.35 \leq 3.55 < 3.80$	0.96	±0.13	±0.26	+0.31/ − 0.19
$3.80 \leq 4.07 < 4.40$	1.02	±0.16	±0.31	+0.33/ − 0.20
$4.40 \leq 4.71 < 5.10$	1.04	±0.19	±0.37	+0.34/ − 0.20
$5.10 \leq 5.49 < 6.00$	0.97	±0.23	±0.41	+0.32/ − 0.19

	60-80%			
	d^{2}N/dηdp$_\perp$(STAR)/T$_{AA}$d^{2}σ/dηdp$_\perp$(NN)			
p$_\perp$ (GeV/c)	(value)		(uncertainty)	
		(data)	(total)	(⟨N$_{bin}$⟩)
$1.70 \leq 1.75 < 1.80$	0.94	±0.13	±0.16	+0.80/ − 0.25
$1.80 \leq 1.85 < 1.90$	0.93	±0.13	±0.16	+0.79/ − 0.24
$1.90 \leq 1.95 < 2.00$	0.96	±0.14	±0.17	+0.81/ − 0.25
$2.00 \leq 2.05 < 2.10$	1.01	±0.14	±0.19	+0.86/ − 0.27
$2.10 \leq 2.15 < 2.20$	1.01	±0.15	±0.19	+0.86/ − 0.27
$2.20 \leq 2.25 < 2.30$	1.03	±0.15	±0.20	+0.88/ − 0.27
$2.30 \leq 2.35 < 2.40$	1.03	±0.15	±0.21	+0.87/ − 0.27
$2.40 \leq 2.49 < 2.60$	1.07	±0.15	±0.22	+0.91/ − 0.28
$2.60 \leq 2.70 < 2.80$	1.09	±0.16	±0.24	+0.92/ − 0.29
$2.80 \leq 2.90 < 3.00$	1.18	±0.18	±0.28	+1.00/ − 0.31
$3.00 \leq 3.16 < 3.35$	1.08	±0.17	±0.27	+0.92/ − 0.28
$3.35 \leq 3.55 < 3.80$	1.13	±0.20	±0.32	+0.96/ − 0.30
$3.80 \leq 4.07 < 4.40$	1.21	±0.23	±0.39	+1.03/ − 0.32
$4.40 \leq 4.71 < 5.10$	1.27	±0.31	±0.49	+1.08/ − 0.34
$5.10 \leq 5.49 < 6.00$	1.35	±0.43	±0.64	+1.15/ − 0.36

Appendix H

R_{AA} Vs $\langle N_{part} \rangle$

$\langle N_{part} \rangle$	(value)		(uncertainty)
		(data)	$(\langle N_{bin} \rangle)$
350.0	0.71	± 0.11	$+0.05/-0.05$
296.0	0.71	± 0.10	$+0.05/-0.06$
232.0	0.71	± 0.10	$+0.06/-0.07$
165.0	0.76	± 0.10	$+0.10/-0.10$
115.0	0.77	± 0.09	$+0.13/-0.13$
61.5	0.82	± 0.10	$+0.20/-0.20$
19.7	0.94	± 0.13	$+0.34/-0.43$
350.0	0.62	± 0.14	$+0.04/-0.04$
296.0	0.63	± 0.14	$+0.05/-0.05$
232.0	0.70	± 0.14	$+0.06/-0.07$
165.0	0.80	± 0.14	$+0.10/-0.10$
115.0	0.83	± 0.13	$+0.14/-0.14$
61.5	1.03	± 0.13	$+0.25/-0.25$
19.7	1.08	± 0.17	$+0.39/-0.50$
350.0	0.37	± 0.11	$+0.03/-0.03$
296.0	0.42	± 0.12	$+0.03/-0.03$
232.0	0.51	± 0.14	$+0.04/-0.05$
165.0	0.71	± 0.19	$+0.09/-0.09$
115.0	0.77	± 0.19	$+0.13/-0.13$
61.5	0.97	± 0.23	$+0.24/-0.24$
19.7	1.35	± 0.43	$+0.48/-0.62$

The table is divided into three sections with headers:
- $1.7 \leq p_\perp < 1.8$ GeV/c, $dN/d\eta dp_\perp(STAR)/\langle N_{bin}\rangle dN/d\eta dp_\perp(NN)$ (for rows 350.0 through 19.7, first block)
- $3 \leq p_\perp < 3.35$ GeV/c (second block)
- $5.1 \leq p_\perp < 6$ GeV/c (third block)

Table H.1:

Appendix I

$\langle N_{part} \rangle$ Scaling Vs $\langle N_{part} \rangle$

$\langle \text{N}_{\text{part}} \rangle$	(value)		(uncertainty)
	(data)		$(\langle \text{N}_{\text{bin}} \rangle)$
$1.7 \leq p_\perp < 1.8$ GeV/c $(\text{dN/dp}_\perp \langle \text{N}_{\text{part}} \rangle /2)_{\text{cent}}/(\text{dN/dp}_\perp / \langle \text{mN}_{\text{part}} \rangle)_{\text{periph}}$			
350.0	4.14	± 0.65	$+0.05/-0.05$
296.0	3.88	± 0.57	$+0.09/-0.09$
232.0	3.61	± 0.52	$+0.14/-0.14$
165.0	3.42	± 0.46	$+0.21/-0.21$
115.0	2.99	± 0.36	$+0.26/-0.31$
61.5	2.56	± 0.30	$+0.37/-0.46$
19.7	2.00	± 0.28	$+0.51/-0.61$
$3 \leq p_\perp < 3.35$ GeV/c			
350.0	3.17	± 0.71	$+0.04/-0.04$
296.0	3.05	± 0.67	$+0.07/-0.07$
232.0	3.09	± 0.63	$+0.12/-0.12$
165.0	3.16	± 0.56	$+0.19/-0.19$
115.0	2.81	± 0.43	$+0.24/-0.29$
61.5	2.80	± 0.35	$+0.41/-0.50$
19.7	2.00	± 0.31	$+0.51/-0.61$
$5.1 \leq p_\perp < 6$ GeV/c			
350.0	1.57	± 0.45	$+0.02/-0.02$
296.0	1.66	± 0.46	$+0.04/-0.04$
232.0	1.85	± 0.52	$+0.07/-0.07$
165.0	2.25	± 0.60	$+0.14/-0.14$
115.0	2.13	± 0.52	$+0.18/-0.22$
61.5	2.12	± 0.50	$+0.31/-0.38$
19.7	2.00	± 0.64	$+0.51/-0.61$

Table I.1:

Bibliography

[1] Geant, Detector Description and Simulation Tool. Technical report, 1993. CERN Program Library Long Writeup W5013.

[2] K. Golec-Biernat A. Stasto and J. Kwiecinski. *Phys.Rev.Lett*, 86:596, 2001.

[3] A.H.Mueller and J.W.Qiu. *Nucl.Phys.*, B268:427, 1986.

[4] B.B.Back. *Phys.Rev.*, C65:031901, 2002.

[5] J.D. Bjorken. *FERMILAB-PUB-82-59-THY*.

[6] W. Blum and L. Rolandi. *Particle Detection With Drift Chambers*. Springer Verlag, Berlin, Second edition, 1994.

[7] D. Boyanovsky. *hep-ph/0102120*.

[8] A.Schafer B.Z.Kopeliovich, J.Nemchik and A.V.Tarasov. *Phys.Rev.Lett*, 88:0232303, 2002.

[9] A. Cardenas. Charged Kaon Production at Mid-Rapidity in Gold-Gold Collisions at $\sqrt{s_{\mathrm{NN}}}$=130GeV, PhD thesis, Purdue University. 2001.

[10] N.I. Chernov and G.A. Oskov. *Comp.Phys.Comm.*, 33:329, 84.

[11] The STAR Collaboration. URL: http://www.star.bnl.gov/STAR/html/tpc_l/tpc.html.

[12] The STAR Collaboration. Conceptual Design Report for the Solenoidal Tracker At RHIC. Technical report, 1992. LBL PUB-5347.

[13] J.C. Collins and M.J. Perry. *Phys. Rev. Lett.*, 36:1353, 1975.

[14] J.W. Cronin. *Phys.Rev.*, D11:3105, 1975.

[15] M. Calderón de la Barca Sánchez. Charged Hadron Spectra in Au+Au Collisions at $\sqrt{s_{\mathrm{NN}}}$=130GeV, PhD thesis, Yale University. 2001.

[16] D.J.Gross and F.Wilczek. *Phys.Rev.*, D8:3633, 1973.

[17] R.D.Pisarski D.J.Gross and L.G.Yaffe. *Rev.Mod.Phys.*, 53:43, 1981.

[18] D.Kharzeev. *Phys.Lett.*, B378:238, 1996.

[19] C.Lourenco D.Kharzeev and M.Nardi. *Z.Phys.*, C74:307, 1997.

[20] E.Levin D.Zharzeev and McLerran L. hep-ph/0210332.

[21] K.J. Eskola. *Tampere 1999*, page 231.

[22] A. Breakstone *et al.* *Z.Phys.*, C23:1.

[23] A.J.Blatz *et al.* *Nucl.Instr.Meth*, A417:1, 1998.

[24] C.Albajar *et al.* *Nucl.Phys.*, B335:261, 1990.

[25] D. Antreasyan *et al.* *Phys.Rev.*, D19:764, 1979.

[26] F. Bergsma *et al.* The STAR Magnet System. Technical report. URL: http://www.star.bnl.gov/j̃hthomas/NimWeb/magnet/magnet_nim.ps.

[27] F.S. Bieser *et al.* The STAR Trigger. Technical report. URL: http://www.star.bnl.gov/j̃hthomas/NimWeb/trigger/trigger_nim.ps.

[28] G. Arnison *et al.* *Phys.Lett.*, B118:173, 1982.

[29] K.Adcox *et al.* *Phys.Rev.Lett*, 88:022301, 2001.

[30] K.Adcox *et al.* *Phys.Rev.Lett*, 88:0242301, 2002.

[31] M. Anderson *et al.* A Readout System for the STAR Projection Chamber. *nucl-ex/0205014.*

[32] M. Anderson *et al.* The STAR Projection Chamber: A Unique Tool for Studying High Multiplicity Events at RHIC. *nucl-ex/0301015.*

[33] P.Abreu *et al. Eur.Phys.J.*, C17:207, 2000.

[34] P.B. Straub *et al. Phys.Rev.Lett*, 68:452, 1992.

[35] D. Buskulic *et al.* ALEPH Collaboration. *Phys.Lett.*, B384:353, 1996.

[36] R. Barate *et al.* ALEPH Collaboration. *Phys.Rept.*, 294:1, 1998.

[37] W.Bartel *et al.* JADE Collaboration. *Z.Phys.*, C33, 1986.

[38] J.Velkovska *et al.* PHENIX Collaboration. *Nucl.Phys.*, A698:507, 2002.

[39] C. Adler *et al.* STAR Collaboration. *Phys.Rev.Lett.*, 87:262302, 2001.

[40] C. Adler *et al.* STAR Collaboration. *Phys.Rev.Lett.*, 89:092301, 2002.

[41] C. Adler *et al.* STAR Collaboration. *Phys.Rev.Lett.*, 89:202301, 2002.

[42] C. Adler *et al.* STAR Collaboration. *Phys.Rev.Lett.*, 90:032301, 2003.

[43] C. Adler *et al.* STAR Collaboration. *Phys.Rev.Lett.*, 90:082302, 2003.

[44] E. Laermann F. Karsch and A. Peikert. *Phys.Lett.*, B478:447, 2000.

[45] R. Fruühwirth. *Comp.Phys.Comm.*, 100:1, 1997.

[46] F.Yuan. *Private Communication.*

[47] G.C.Rossi and G.Veneziano. *Nucl.Phys.*, B123:507, 1977.

[48] G.D.Lafferty and T.R.Wyatt. *Nucl.Instrum.Meth.*, A355:541, 1995.

[49] N.K. Glendenning and F. Weber. *astro-ph/0003426.*

[50] Particle Data Group. *Eur. Phys. J.*, C15:1, 2000.

[51] K. Schilling G.S. Bali and A. Wachter. *Phys.Rev.*, D56:2566, 1997.

[52] M. Gyulassy. *Lect.Notes.Phys.*, 583:37, 2002.

[53] M. HIrai and S. Kumano. *Phys.Rev.*, D64:34003, 2001.

[54] M. Gyulassy I. Vitev and P. Levai. *nucl-th/0204019.*

[55] I.Vitev. *Private Communication.*

[56] I.Vitev and M.Gyulassy. *Phys.Rev.*, C65:41902, 2002.

[57] P. Jacobs. *Private Communication*, 2002.

[58] B.A.Kniehl J.Binnewies and G.Kramer. *Z.Phys*, C65:433, 1995.

[59] J.Ollitrault. *Nucl.Phys.*, A638:195, 1998.

[60] J.P.Blaizot and E.Iancu. *Phys.Rept.*, 359:355, 2002.

[61] J.I. Kapusta. *Nucl. Phys.*, B148:461, 1979.

[62] F. Karsch. *Lect.Notes Phys.*, 583:209, 2002.

[63] K. Kayana. *hep-ph/0209116.*

[64] K.Golec-Biernat and M. Wusthoff. *Phys.Rev.*, D60:114203, 1999.

[65] K.G.Wilson. *Phys.Rev.*, D10:2445, 1974.

[66] D.E. Kharzeev. *nucl-th/0206073.*

[67] V.J. Kolhinen K.J.Eskola and C.A.Salgado. *Eur.Phys.J.*, C9:61, 1999.

[68] E. Levin. hep-ph/0105205.

[69] D. Liko. Track Fitting in the STAR Detector using the Kalman Filter Method. Technical report, 1992. STAR Note 87.

[70] M.A. Lisa. The STAR-TPC Clusterfinder/Hitfinder. Technical report, 1996. STAR Note 238.

[71] L.McLerran. hep-ph/0202270.

[72] L.McLerran and R.Venugopalan. *Phys.Rev.*, D49:2233, 1994.

[73] E.M.Levin L.V.Gribov and M.G.Ryskin. *Phys.Rept.*, 100:1, 1983.

[74] K.Rajagopal M.Alford and F.Wilczek. *Phys.Lett.*, B422:247, 1998.

[75] S. Margetis and D. Cebra. Main Vertex reconstruction in STAR. Technical report, 1992. STAR Note 90.

[76] M.E.Peskin. *An Introduction to Quantum Field Theory.* Westview Press, 1995.

[77] M.Gyulassy. *Nucl.Phys.Proc.Suppl.*, 53:95, 1997.

[78] M.Gyulassy and M.Plumer. *Phys.Lett.*, B243:432, 1990.

[79] M.Gyulassy and X.N.Wang. *Nucl.Phys.*, B420:583, 1994.

[80] I.Vitev M.Gyulassy and X.N.Wang. *Phys.Rev.Lett.*, 86:2537, 2001.

[81] X.N.Wang M.Gyulassy, I.Vitev and B.Zhang. *nucl-th/0302077*.

[82] X.N.Wang M.Gyulassy, I.Vitev and P.Houvinen. *Phys.Lett.*, B526:301, 2002.

[83] Jeffery T. Mitchell and Iwona M. Sakrejda. Tracking for the STAR TPC: Documentation and User's Guide. Technical report, Lawrence Berkeley National Laboratory, 1994. STAR Note: SN0190.

[84] M.Miller. *Private Communication*, 2001.

[85] P.M. Dinh N.Borghini and J.Ollitrault. *Phys.Rev.*, C64:054901, 2001.

[86] N.Brown and W.J.Stirling. *Phys.Lett.*, B252:657, 1990.

[87] P.M.Jacobs. Remarks on the Geometry of High Energy Nuclear Collisions. Technical report, 1999. STAR note 402.

[88] RHIC Project. RHIC Design Manual. Technical report, Brookhaven National Laboratory, 1994. URL: http://www.agsrhichome.bnl.gov/NT-share/rhicdm/.

[89] P.Steinberg. URL: http://hep.phy.uct.ac.za/šteinber.

[90] D. Schiff R. Baier and B.G. Zakharov. *Ann.Rev.Nucl.Part.Sci.*, 50:37, 2000.

[91] L. Ray. URL: http://www.star.bnl.gov/r̃ay/EVR_REVIEW_TALK_LBNL_2000.ps.

[92] R.J.Glauber. High energy collision theory. 1959.

[93] W.J. Stirling R.K. Ellis and B.R. Webber. *QCD and Collider Physics*. Cambridge University Press, 1996.

[94] E.V. Shuryak. *Phys. Lett.*, D53:150, 1978.

[95] E.V. Shuryak. *Phys.Rev.*, C66:027902, 2002.

[96] S.Kumano and M.Miyama. *Phys.Rev.*, D64:034003, 2001.

[97] BRAHMS(www4.rcf.bnl.gov/brahms/WWW/brahms.html); PHOBOS(phobos srv.chm.bnl.gov); PHENIX (www.phenix.bnl.gov); STAR (www.star.bnl.gov).

[98] T.Roser. *AIP Conf.Proc.*, 572:191, 2000.

[99] T.Sjóstrand. *Private Communication*.

[100] T.Ullrich. http://star.physics.yale.edu/wrk/support-doc/ua1scaling.ps.

[101] I. Vitev and M. Gyulassy. *Phys.Rev.Lett*, 89:0252301.

[102] V.Muccifora. *Proceedings of 9th International Workshop on Deep Inelastic Scattering*, page 191, 2001.

[103] V.N.Gribov. *Sov.Phys.JETP*, 29:483, 1969.

[104] X.N. Wang. *Phys.Rev.*, D47:2754, 1993.

[105] X.N. Wang. *Nucl.Phys.*, B702:238, 2002.

[106] X.N.Wang. *Phys.Rev.*, C61:064910, 2000.

[107] Y.V.Kovchegov and K.Tuchin. *Nucl.Phys.*, A708:413, 2002.

Vita

Bum Choi was born in South Korea. Bum Choi passed his formative years in the United States of America, the greatest nation-state in history, or the latest incarnation of the evil empire, depending on your point of view. Bum Choi personally believes in the former.

Permanent address: 821 Barlow St
                                  Philadelphia, PA 19116

This dissertation was typeset with LaTeX† by the author.

---

†LaTeX is a document preparation system developed by Leslie Lamport as a special version of Donald Knuth's TeX Program.